CRANFIELD UNIVERSITY

LI FANG

SUPPRESSION OF STALL ON HIGH-CAMBER FLAP USING UPPER-SURFACE BLOWING

SCHOOL OF ENGINEERING
MSc THESIS

MSc BY RESEARCH
Academic Year: 2010 - 2011

Supervisor: Dr. Vladimir Titarev, Dr. Shijun Guo
January 2011

CRANFIELD UNIVERSITY

SCHOOL OF ENGINEERING

MSc BY RESEARCH

Academic Year 2010 - 2011

LI FANG

SUPPRESSION OF STALL ON HIGH-CAMBER FLAP USING UPPER-SURFACE BLOWING

Supervisor: Dr. Vladimir Titarev, Dr. Shijun Guo

January 2011

This thesis is submitted in partial fulfilment of the requirements for the degree of Master of Science

ABSTRACT

For many years, high-lift devices of an aeroplane have been employed to enhancing the aerodynamic performance of the wing during take-off and landing. But their complex geometries not only increase the design and manufacture cost, but also result in lower maintainability and reliability. Further more, they have been thought to be a major noise source of civil airliners. As one of the possible solutions, single-slot variable-camber flap design can greatly decrease the system complexity and the design cost of the high-lift system. However, the deteriorated stall behaviour of the flap prevents this concept to obtain its full benefits at high flap deflection angle.

In this thesis, separation control and lift-enhancing capabilities of upper-surface blowing have been studied and tested numerically on a two-dimensional two-element airfoil. The baseline airfoil consists of a drooped leading edge and a fowler flap with variable-camber feature and deflected at 35°. A compressible structured-grid RANS code with SA turbulence model has been validated and employed to perform the simulations. All CFD simulations were performed at typical landing condition with M_∞=0.2 and Re=15.3×10^6.

This study started with two baseline cases, including normal flap and high-camber flap configurations. Simulation results showed that larger separation region was observed on the flap if the camber of the flap was further increased. The lift of the airfoil had barely changed, but the drag was affected.

Then, upper-surface blowing was applied on the high-camber flap configuration. Two blowing methods have been studied: tangential blowing and non-tangential blowing. Computed results showed that both methods were quite effective against separation once sufficient blowing momentum had applied. For the tested blowing slot designs, the non-tangential blowing showed its advantage in avoiding the drag penalty when the blowing system was off.

ACKNOWLEDGEMENTS

I would like to express my gratitude to my supervisors Dr. Vladimir Titarev and Dr. Shijun Guo for their instructive advices, useful suggestions and the inspiring discussions. I shall extend my thanks to Dr. Bowen Zhong for his impressive kindness, patience and help in the completion of this thesis.

My sincere thanks are also given to Dr. R. L. Oswald for helping me with performing the CFD simulations.

A special acknowledgement should show to Mrs Elizabeth Anderson for helping me with my thesis writing and my life in England. I would like to thank all my friends for their help, too.

Last but not least, I would not be able to finish this thesis without the constant support from my whole family. My deepest gratitude goes to my love Hui Sheng for her understanding and caring.

TABLE OF CONTENTS

LIST OF FIGURES

LIST OF TABLES

LIST OF EQUATIONS

Nomenclature

Latin Symbols

AOA	Angle of attack
c	Reference chord length
c_{flap}	Flap chord length
C_L	Lift coefficient
C_{Lmax}	Maximum lift coefficient
C_D	Drag coefficient
C_M	Momentum coefficient
C_p	Pressure coefficient
C_μ	Blowing momentum coefficient
D	Drag
h	Blowing slot height
HBR	High blowing rate
L	Lift
LBR	Low blowing rate
M	Mach number
M_∞	Free flow Mach number
MBR	Medium blowing rate
Re	Reynolds number
V_s	Jet Velocity at the Blowing Slot exit
V_∞	Free flow velocity
x	X-Coordinate
y	Y-Coordinate
ZB	Zero blowing

Greek Symbols

α	Angle of attack

1 Introduction

The author has been involved in two different projects, which are the Group Design Project (GDP) and the Individual Design Project (IRP), for the one-year MSc study in Cranfield from 22nd Feb. 2010 to 21st Feb. 2011. Introductions of these projects are given in the following sections.

1.1 The Group Design Project (GDP)

The Group Design Project (GDP) which started in 2008 is a three-year aircraft design MSc training program for AVIC. The major objective of this program is to deliver a brand new design of 130-seat civil aeroplane (see Fig. 1-1). In 2008, the first cohort of AVIC students finished the conceptual design and named this 130-seat civil aeroplane the Flying Crane. This was followed by the preliminary design which was accomplished by the second cohort in 2009. This year is the third year of the GDP, and the target of this phase is to complete the detailed design of the Flying Crane.

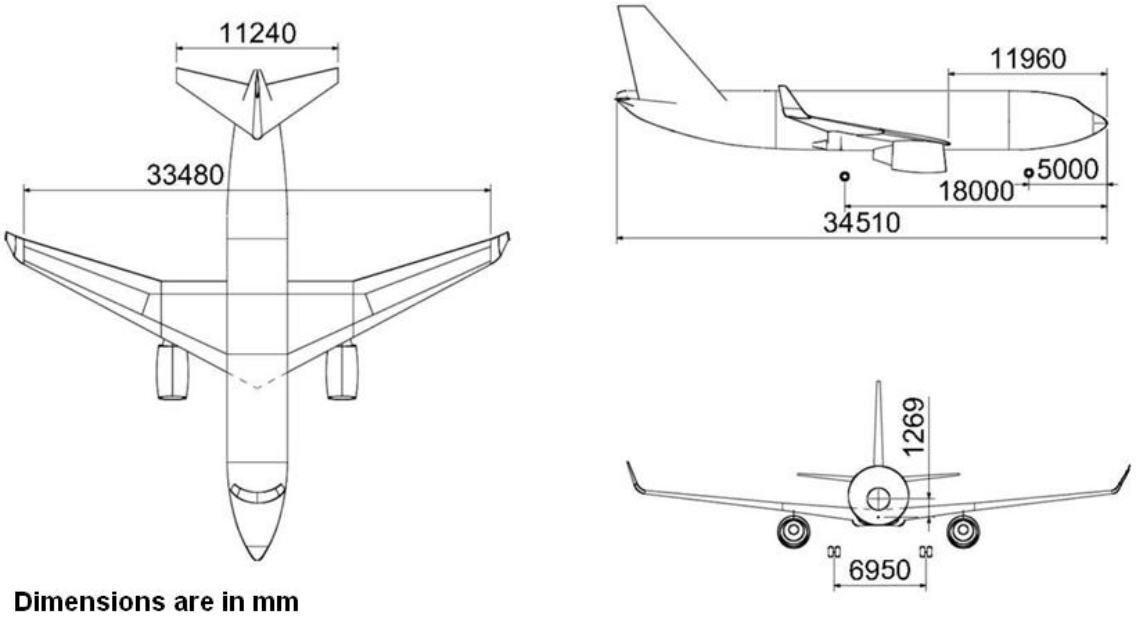

Figure 1-1 Three-view drawing of the Flying Crane

The author is in charge of the scarf intake design, intake aerodynamic performance study and mass & CG control of the Flying Crane. The schedule and responsibility of the author's work are listed in table 1-1.

Table 1-1 Personal schedule and responsibility of the GDP

Phase	Time	Responsibility
Phase I	18th Mar. ~ 15th Apr.	*Preliminary design study and check* Including: 1. Nacelle design and installation check. 2. Mass and CG check.
Phase II	16th Apr. ~ 10th May.	*Nacelle Design and Mass & CG control* Including: 1. Nacelle design and sizing. 4 different designs have been delivered. 2. Nacelle 3D CATIA model generation. 3. Mass and CG updating.
Phase III	11th May ~ 10th Jun.	*Nacelle aerodynamic performance study and Mass &CG control* Including: 1. CFD analysis of the nacelle. All 4 nacelle designs have been compared and 1 has been chosen. 2. Mass and CG updating.
Phase IV	11th Jun. ~ 10th Jul.	*Nacelle, wing interference study and Mass & CG control* Including: 1. Nacelle, wing interference study using CFD approach. 2. Mass and CG updating.
Phase V	11th Jul. ~ 3rd Sep.	*Mass & CG control and final presentation* Including: 1. Mass and CG updating. 2. Thesis writing. 3. GDP final presentation

1.2 The Individual Research Project (IRP)

During take-off and landing, the leading and trailing edge devices can greatly increase the maximum lift coefficient of the wing by increasing the camber and the area of the wing. Variable camber flap can further increase the aerodynamic performance of the wing compared to the contemporary design. Single-slot variable-camber flap design will decrease the system complexity simultaneously. But the stall character of the flap will deteriorate if the camber is further increased at high deflection angle. In the hope of making the flap more efficient and obtaining the full benefits, active flow control technology, e.g. the upper-surface blowing, could be applied.

The author's work is mainly focused on employing upper-surface blowing for separation control of an existing high-camber flap at typical landing conditions. Following aspects have been covered:

a. Influence of flap camber change without separation control.

b. Effects of the steady upper-surface blowing and how the jet affects the lift, drag, moment characters and stall behaviour of the multi-element airfoil.

c. Differences between tangential and non-tangential blowing.

d. The influence of momentum coefficient C_μ that defines the strength of blowing is simulated and analyzed in different conditions.

The study of relevant topics started at the beginning of the GDP. Learning of basic theories and necessary software has been accomplished in this stage. Then, two baseline cases and two blowing cases were chosen. All tested cases are airfoils which included drooped leading edge slats and a Fowler flaps deployed at 35° (typical landing configuration). These airfoils are designed for using on an A320-like short- to medium-range commercial airliner. The first baseline case has a conventional flap and the other one has a high-camber flap. Tangential and non-tangential blowing slots are applied on the high-camber flap and make the two blowing cases.

In order to fulfil the major objectives, CFD approaches have been studied. In the scope of this thesis, the aerodynamic performances including lift, drag, and moment were predicted by solving 2D compressible RANS Equations with the Spalart–Allmaras (SA) one-equation turbulence model on a structured grid. The Fluent 12 has been used as the solver. The numerical method was validated by comparing the computed results of MDA 30P-30N multi-element airfoil and existing experimental data. The influences of far field extent and Reynolds number were studied during the two major stages of the validation. Multi-block structured grids were generated for both validation cases and study cases.

The IRP schedule can be divided into 7 different phases. Each phase is defined as follow:

Table 1-2 Schedule of the IRP

Phase	Time	Executing Schedule
Phase I	4th Mar. ～ 14th May.	*Literature Review Stage I* Including: 1. Review of contemporary high-lift designs, and future trends. 2. Study of problems and possible solutions regarding high-lift system design. 3. The MDA 30P-30N multi-element airfoil has been chosen to be the validation case
Phase II	15th May. ～ 24th Sep.	*Literature Review Stage II* Including: 1. Review of numerical methods. 2. Comparison and capability analysis of different numerical methods. 3. Studies of MDA 30P-30N multi-element airfoil have been highlighted. 4. Methodology was design in this stage.

Phase III	15th Aug. ~ 4th Sep.	*Preparation of validation work* Including: 1. Preparation of case data including geometrical and experimental test data. 2. Geometry generation using CATIA. 3. Grid generation using Gambit, two grids with different far field extents have been built.
Phase IV	5th Sep. ~ 14th Oct.	*Validation of numerical methods* Including: 1. Simulation of validation cases. 2. Postprocessing, results analysis and compare.
Phase V	4th Oct. ~ 24th Oct.	*Preparation of study cases* Including: 1. Geometrical data preparation. 2. Geometry generation using CATIA, four multi-element airfoils have been built. 3. Grid generation using Gambit, four grids have been built regarding different case geometries.
Phase VI	25th Oct. ~ 24th Dec.	*Simulation execution and results analysis* Including: 1. Execution of simulations which are 36 cases in total, including 4 cases, each with 3 different AOA and 3 different blowing strength. 2. Postprocessing and results analysis.
Phase VII	25th Nov. ~ 24th Jan.	*Summarization and thesis writing* Including: 1. Summarizing of IRP works and proposing future works. 2. Thesis writing.

2 Literature review

The literature review includes following aspects. Firstly, the contemporary high-lift system designs and the future trends are studied. This is followed by a review of both experimental and computational studies concerning the MDA 30P-30N airfoil, so as to obtain a clear view of the capability of contemporary experimental test and computational prediction. Then, the variable camber flap concept and the recent achievements are covered. Last but not the least, review of the active flow control methods is given and special attention is paid to separation control methods.

2.1 Review of modern high-lift system

High-lift devices, which are the typical camber-changing component, have been employed for better low speed performance of aircraft though providing extra lift during take-off and landing.

Nowadays, the use of high-lift systems has already become one of the major factors that greatly affect the whole aircraft design, especially the cost. Firstly, the high-lift device is sophisticated and expensive. According to Rudolph (1996), 6% to 11% of the production cost of a jet transport is taken by high-lift system. Secondly, its performance has a huge impact on aircraft efficiency. For a typical twin-engine jet transport, following relations are obtained by Butter (1984):

- Increase in the take-off C_{Lmax} by 5% may increase the payload of the aircraft by 12-15%.
- Increase in the take-off L/D by 5% may increase the payload of the aircraft by 20%.
- Increase in the landing C_{Lmax} by 5% may increase the payload of the aircraft by 25%.

Garner and Meredith (1991) also gave similar examples:

- "A 0.10 increase in lift coefficient at constant angle of attack is equivalent

to reducing the approach attitude by 1°. For a given aft body-to-ground clearance angle, the landing gear may be shortened for a savings of airplane empty weight of 1400 lb."

- "A 1.5% increase in maximum lift coefficient is equivalent to a 6600 lb increase in payload at a fixed approach speed."

- "A 1% increase in take-off L/D is equivalent to a 2800 lb increase in payload or a 150 nm increase in range."

All these examples explain why high-lift system design is an issue of such great importance. In the hope of achieving higher capability, high-lift design and lift-enhancing concepts have continuously been brought up and the design disciplines have been changed. According to van Dam's review (2002), early attempts were focused on maximising the C_{Lmax} to meet "the high cruise wing loading needs of jet transport aircraft while retaining acceptable takeoff and landing distances." But the high-lift system itself involves not only the aerodynamic requirement, but also other interactive constraints such as structure, system, etc. Complex configurations, e.g. the tripe-slotted Fowler flap systems applied on Boeing B727, not only increase the design and manufacture cost, but also result in lower maintainability and reliability. Hence, recent researches have turned to "reducing the complexity and weight of the high-lift systems for given maximum lift levels."

For most commercial airliners, e.g. the Airbus A320 and Boeing 737, the high-lift system consists of two components: a leading edge device (slat) and a trailing edge device (flap) (Fig. 2-1). Deflection of these devices can increase the camber of the wing, while their extension (if appropriate) can increase the chord length. How these devices affect the lift character of the wing is shown in Fig. 2-2. Normally, the deflection of flap results in increased C_L, and the larger α_{max} is caused by the deployment of slat. For details of existing high-lift systems that have been applied on civil airliner, the reader is referred to van Dam's review [48].

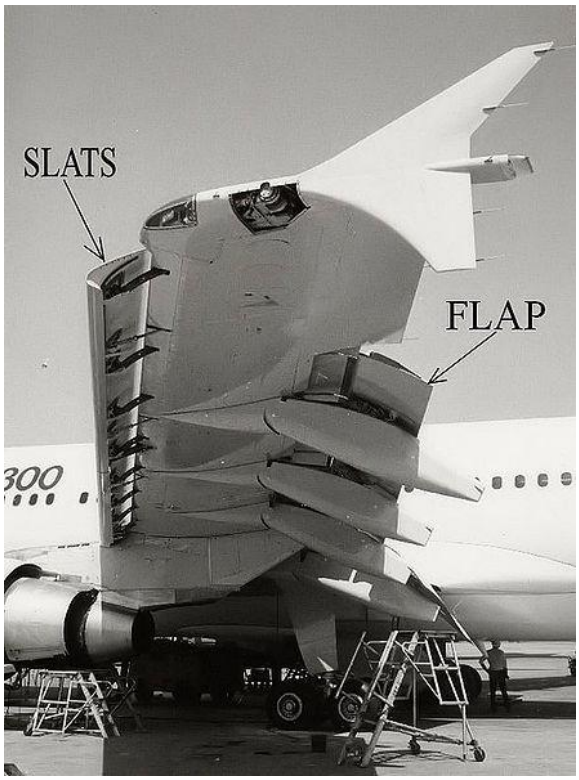

Figure 2-1 Slats and flaps on an Airbus A310-300

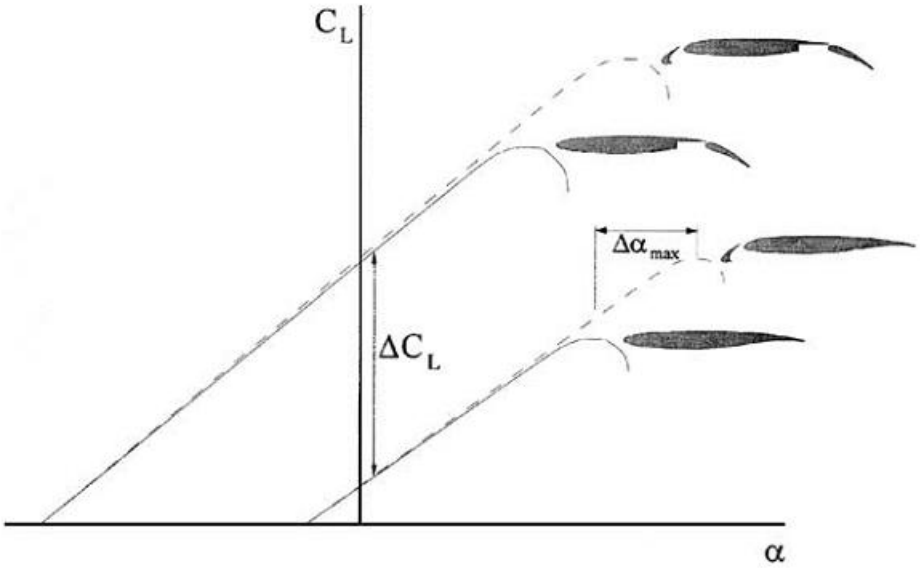

Figure 2-2 Typical high-lift system and its effect on airplane lift [van Dam (2002)]

The flow phenomena around the high-lift system are complex (see Fig. 2-3) and difficult to predict. Though several studies have been conducted, there's still a long way to develop a full understanding of the inherent uncertainties and

inconsistencies within the flow physics, the experimental test and computational prediction.

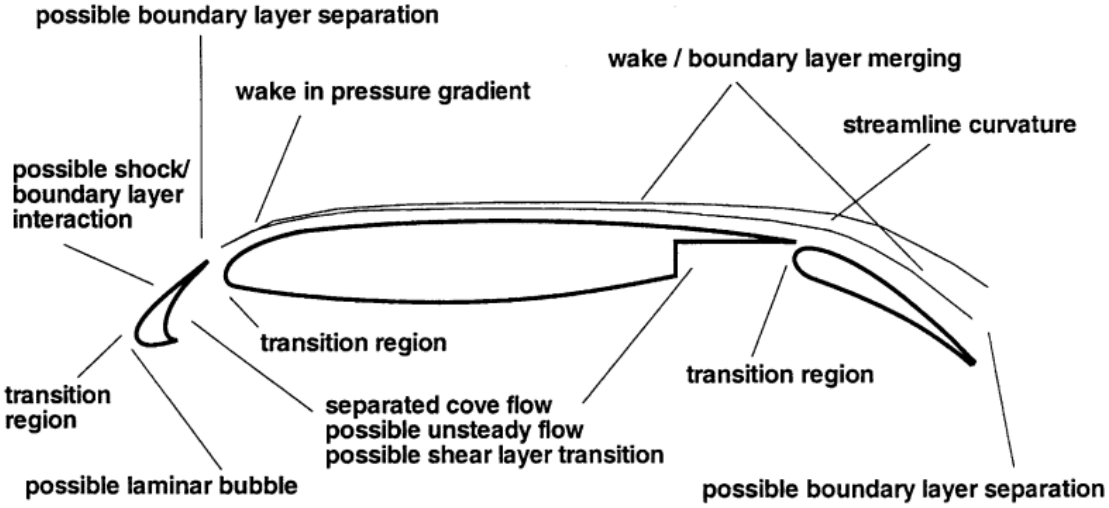

Figure 2-3 Complex flow phenomena over high-lift system [Rumsey and Ying (2002)]

2.2 Review of previous study on multi-element airfoils

There are several multi-element airfoils, such as the GA (W) -1 2-element airfoil and MDA 3-element airfoil. Detailed review was given by Rumsey and Ying (2002). As a representative configuration, the MDA 30P-30N multi-element airfoil, as shown in Fig. 2-4, has been studied both computationally and experimentally. Through all these studies, the capabilities of both experimental test and computational prediction have been obtained. In the following section, a review of investigations on this multi-element airfoil is given.

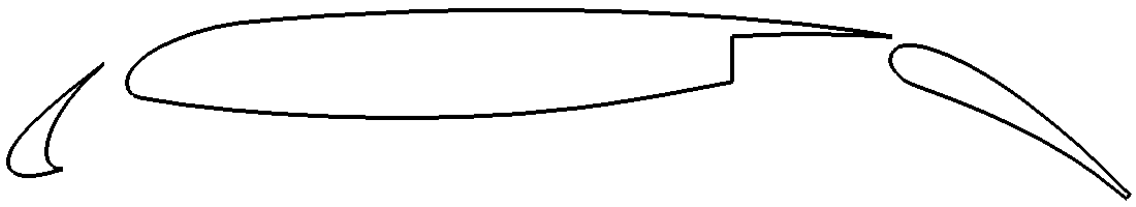

Figure 2-4 Profile of MDA 30P-30N multi-element airfoil

2.2.1 Experimental investigation on MDA 30P-30N airfoil

Many experiments have been done on three-element McDonnell Douglas 30P-30N airfoil to develop further understanding of high-lift flow physics and provide validation data for different CFD codes.

Chin et al. (1993) tested three-element MDA 30P-30N airfoil at the NASA Langley's Low Turbulence Pressure Tunnel (LTPT). Two Reynolds numbers have been tested, which are 5×10^6 and 9×10^6, with Ma=0.2. Comparing the test data at different Reynolds number, lift is greater when the Reynolds number is higher. This tendency increases along with the increase of the angle of attack, but the stall angle is almost the same. The pressure distribution at $\alpha=8°$ shows that separation on the flap is more likely to happen when the Reynolds number is lower. For the velocity profile, lower Reynolds number tends to shift the wakes further away from the flap upper surface and increase their widths.

Klausmeyer and Lin (1994) measured the skin friction of 30P-30N for Reynolds numbers of 5×10^6, 9×10^6 and 16×10^6. Test results have been obtained showing the stall is caused by "off-surface flow reversal in the main element wake," rather than the surface separation on the flap. The flow on the flap interestingly separated at a low angle of attack, but remained attached when α increased. The flap separation, similar to what has found in Chin's work, is "strongly Reynolds number dependent."

Through MDA 30P-30N airfoil is well-known as a typical 2-D design and is tested as 2-D case, one key issue has been brought up by CFD studies is the disagreement between computational simulation and experiment. On the one hand, contemporary CFD codes are problematic when simulate the turbulent flow. On the other hand, wind tunnel tests also involve following uncertainties:

- 3-D effects.
- Wake of wind tunnel wall.
- Effects of extra supporting structures, e.g. the brackets.

Three-dimensional effects have been analyzed by both Bertelrud (1998) and Rumsey et al (2002). According to Bertelrud, “A truly two-dimensional high-lift experiment does not exist.” The existence of side-wall lowers the wing circulation in wall-juncture region and three-dimensionality will spoil the flow, especially on the flap, as the angle of attack further increases. Employing side-wall venting can reduce this effect, but can never eliminate it. Actually, the three-dimensionality was quite significant on the flap above 16° angle-of-attack even with the existence of side-wall venting (see Fig. 2-5). Though experiments always come along with this inconvenient fact, Bertelrud’s study showed the experimental data could be “sufficiently” used for 2-D CFD code validation if the angle of attack is less than 16°, where the experiment could be treated as two dimensional.

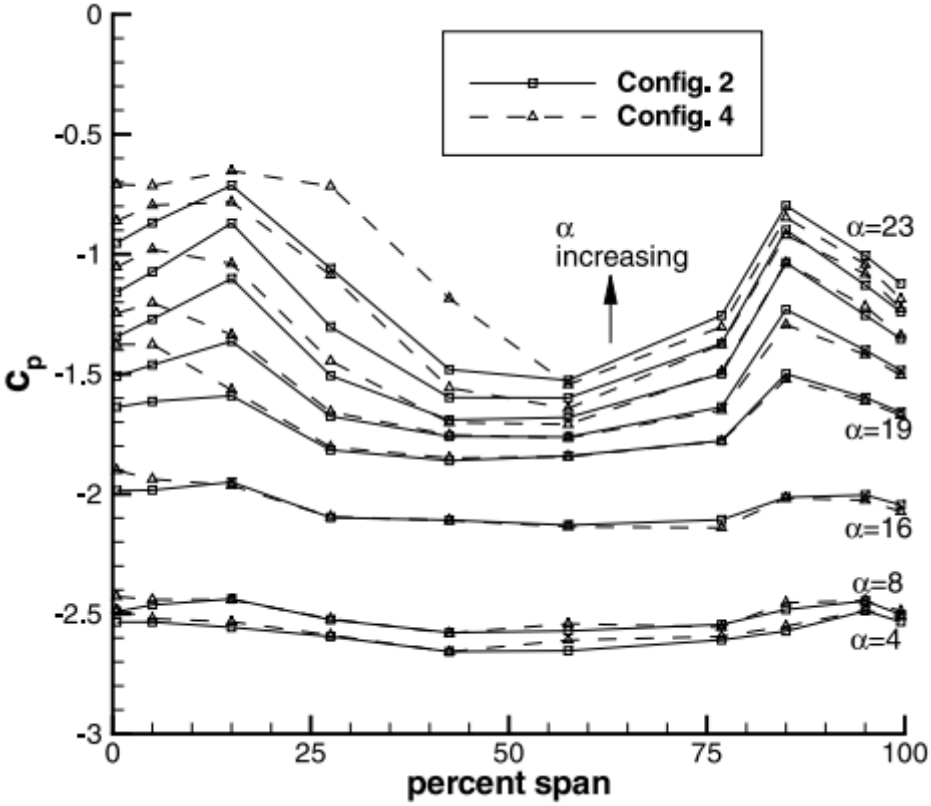

Figure 2-5 Spanwise surface C_p distribution on the flap upper surface [Rumsey et al (2002)]

Rumsey et al (2002) studied the effect of employing side-wall venting. As concluded in their report, if the side-wall venting is off, lift level dropped by 0.1-

0.2 “nearly uniformly”, but the angle of attack at C_{Lmax} remained. The suction levels of side-wall venting didn’t affect the lift levels much (less than 1%) near maximum lift. And by employing special side-wall venting treatment, the angle of attack at C_{Lmax} can be increased by at least 2°.

The effect of brackets has also been analyzed by Rumsey et al. (2002). Because this support system is “inevitable” in experimental test, the only way to judge its effects is through CFD approach. Results showed the existence of brackets reduced the lift by 2-3% near C_{Lmax}.

Another problem highlighted by Bertelrud is the film sheet effect. Attaching the hot film to measure the separation may lead to change of surface roughness and shape, thus increases the 3-D effects. Furthermore, the number of hot films used has huge impact on “captured” location of transition.

2.2.2 Computational investigation on MDA 30P-30N airfoil

Lots of computational works have been conducted on MDA 30P-30N since this CFD challenge was set by NASA Langley in 1993. Most of these works were based on structured- or unstructured-grid RANS code and performed at $Re=9\times10^6$. Despite configuration changes, two facts have been highlighted: turbulence model behavior and disagreement between experimental and computational works.

Different turbulence models have been employed and compared in many studies and the Spalart-Allmaras (SA) turbulence model is the most commonly used one. Though Lynch et al (1996) argued that SA turbulence model was not adequate to predict the flow field of 30P-30N configuration, Klausmeyer and Lin (1994) successfully simulated the flow using 2-D RANS code with SA turbulence model and predetermined boundary layer transition locations. The results matched the test data. Rogers et al. (1994) compared MDA 30P-30N configuration using different turbulence models including BB, SA, and SST etc. Based on their work and summarized by Rumsey and Ying (2002), “differences between predictions of different turbulence models were smaller than

differences between CFD and experimental data." Valarezo et al. (1993) predicted the flow around the flap using three different turbulence models, including BB, SA and k-ε turbulence models. Their results showed "all models were in closer agreement to each other than to experiment," and the location of the attachment point was underpredicted by all these turbulence models.

Several simulations have also been done in order to find whether contemporary CFD approaches can predict the changes caused by Reynolds number changes. For RANS codes, there has been much debate about turbulence model capacity. Dominik (1994) tested an incompressible structured-grid RANS code with three turbulence models: BB, SA, and SST. Performance changes due to the change of Reynolds number were predicted by BB model, but not by SA and SST models. Different result has been obtained by Jones et al. (1995). Their work showed the structured-grid RANS code with SA turbulence model can predict variations with Reynolds number. All of their works are based on fully-turbulent simulation. One possible explanation for this is both the maximum lift and the transitional behaviors are largely dependent on Reynolds number. As given by Rumsey and Spalart (2008), "the SA and SST turbulence models – along with many other models in wide use today – were not designed to predict transition," and "very large regions of laminar flow may signify that the turbulence models are being utilized outside of their intended range of applicability," especially when Reynolds number is low. This could also be the reason why Klausmeyer and Lin's simulation matched the test data well, as boundary layer transition locations have been predetermined.

Another important issue, as mentioned in the previous section, is that the disagreement between computational simulation and experiment is significant. Some trends can be found in previous works:

- For attached flow (at a low angle of attack), most CFD methods were adequate to predict the surface pressure.

- Lift was often overpredicted, especially the C_{Lmax} and the angle of attack at which it occurs. Jones et al. (1995) believed that better grid

distribution near the main element leading edge region may benefit the lift prediction.

- The slat wake was often overpredicted, too. Comparing with the test data, the slat wake was usually predicted to be “too wide” and “too deep.” And Cao et al. (1994) believed coarser grids would enhance this trend.

- Large variability in velocity profiles can be found in many reports. The velocity profiles, especially at high angle of attack, was deemed to be highly sensitive to grid resolution and distribution, while the surface pressures could be resolved with grid of much less amount, e.g. 50,000 points [Anderson et al. (1993)].

Though the disagreement between computational and experimental work still requires further study, some facts that thought to be beneficial for CFD prediction have been concluded. Thomas and Salas (1986) stated that the far field grid extent and boundary condition greatly affect the drag prediction. If the extents are less than 40 times of reference chord, a far field circulation correction was necessary to improve the accuracy of RANS code. For 3D simulation, inclusion of wind tunnel walls and mounting brackets has shown its importance for agreement between computational and experimental data.

2.3 Review of variable-camber flap concept

One way to minimize the complexity of the high-lift device is to decrease the number of slots. Replacing the multi-slot flap with simple Fowler flap and applying hinged leading edge or variable-camber leading edge rather than slat can make the high-lift design much simpler. But on the other hand, these simpler substitutes also come along with decreased performance:

- C_{LMAX} and α_{CLMAX} cannot be obtained due to the separation about the flap and main wing.

- The full benefit of large camber and chord length change can hardly be achieved, thus the ΔC_L will also be affected.

According to recent studies, the variable-camber flap concept has shown its potentials and made it one of the possible solutions of these problems.

No matter how complex the high-lift system is, the contemporary designs are all limited to a certain number of fixed design points. If the high-lift system can be designed targeting on “design envelops” rather than “design points,” the efficiency of the wing and high-lift system can immediately be improved by meeting the full-envelop requirements, while the complexity of high-lift system is kept low. This is the motivation of variable-camber flap. In addition to this, the variable flap geometries also make them capable to act as control surfaces like the ailerons. Two major functions of the variable camber flap are:

a. To provide improved aerodynamic performance.

b. To provide control capability during flight.

The benefit of employing variable-camber flap can be significant and recent studies showed its great potential. Mentioned in Rechzeh’s report (2003), Airbus Germany tested new high-lift concepts as a part of the German national research and technology programme which is also known as HAK. In these tests, variable-camber flaps have been used to create the complete wingspan trailing edge devices (Fig. 2-6).

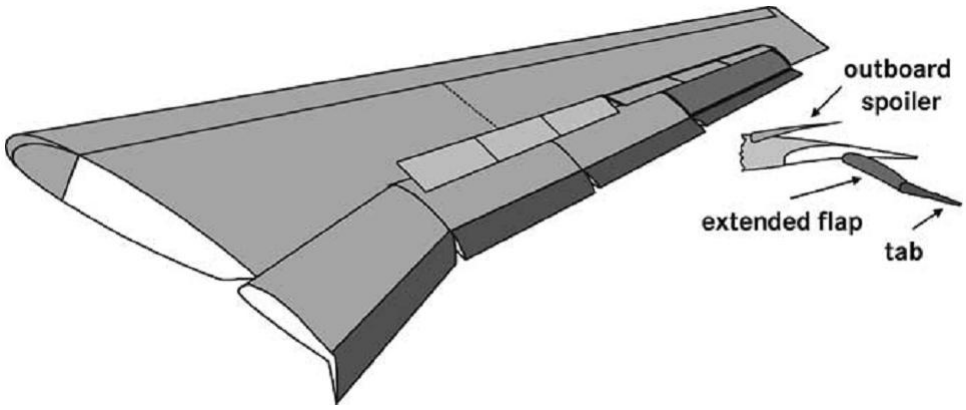

Figure 2-6 HAK high-lift wing design with extended flap and trailing edge tabs [Rechzeh (2003)]

Test results showed this design is promising and “for a take-off configuration in 2nd segment climb a drag improvement of app. 6% was possible while maximum lift was increased by 4%.” Besides, using the differentially controlled trailing edge tabs and spoilers for roll control means there is no need to apply the aileron on the wing. Furthermore, wing loading adaptation, gust alleviation and quick configuration change are also potential benefit of applying this design.

Despite all these potential benefits, several problems, such as the structure, control system, etc, must be solved before these concepts can be employed on a large commercial airliner. Besides, though camber of the flap can be increased, separated flow on the upper surface of the main wing and the flap is still an “inevitable” phenomenon and could be even worse when the aircraft is flying at a high angle of attack or the camber of the flap is high. As a result, the performance of variable-camber flap is not necessarily better than an original design, if the separation flow has not been properly controlled. And furthermore, the control of the aeroplane may not be maintained by changing of flap camber when flow separation occurs. To summarise, the variable-camber flap concept is promising and proper separation control devices should be employed to achieve its full potential.

2.4 Review of separation control

Although the main objective of this thesis is the study of the separation control for high-lift devices, brief review and discussions of different active flow control methods are also covered in this section.

Collis et al. (2004) listed that the objectives of applying active flow control include “drag reduction, separation control, enhanced mixing, noise suppression, change of a surface property, etc.” Contemporary methods include applying leading-edge suction to delay transition, upper-surface blowing to eliminate boundary-layer separation, and using vortex generator or synthetic jet to enhance the exchange of momentum between the boundary layer and the outer flow, etc. Concluded by Donovan et al. (1998), it is possible to achieve both

improved lift/drag characteristic of the wing/airfoil and manoeuvre capability without control surface deflection by employing active flow control approaches,

Contemporary methods of separation control can be divided into two categories: passive actuation devices (e.g. vortex generators) and active control devices (e.g. synthetic jet). They all work on the same principle, which is “to bring momentum into the boundary layer (BL) in order to allow it to sustain the strong adverse pressure gradient (APG),” as discussed by Godard and Stanislas (2006). The major difference that distinguishes one from the other is the passive actuation devices introduce steady input to the flow field while unsteady input is provided by active control devices. Each method has its own advantages and disadvantages. The passive actuation devices can be simpler and cheaper for both design and manufacture. But the continuous suction or blowing approaches are energy consuming, while, stated by Collis et al. (2004), the steady control “may only be effective over a limited range of operating conditions,” due to the inherent unsteadiness of the flow fields. For active control devices, more flexible control can be introduced, and possible global effects triggered by small input also lead to less energy requirements. On the other hand, understandings of incoming flow and its response to the control input, e.g. the oscillatory momentum injection, are necessary and must be developed prior to a successful design, where more complex control system should be employed.

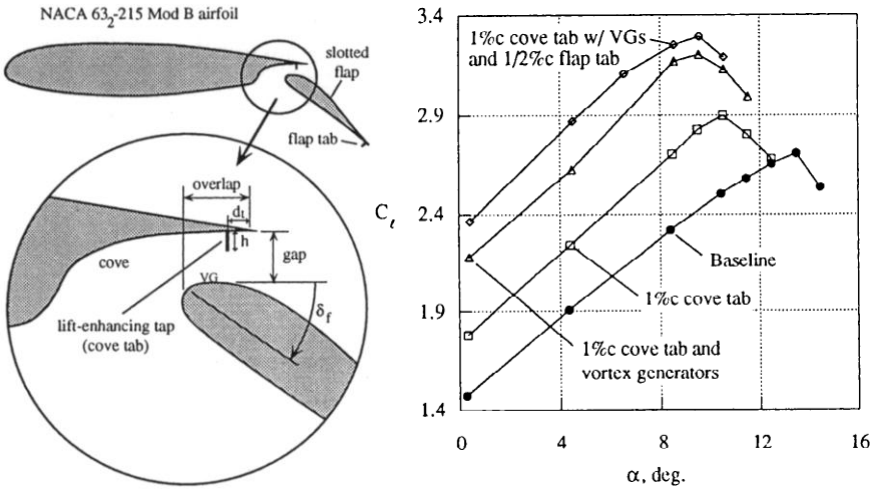

Figure 2-7 Lift-enhancing tabs and its effect on lift, M_∞=0.2, Re=3.7×10^6 [46]

As one of the oldest separation control concepts, the vortex generator has been studied through several different aspects and has been applied in many practical situations. The idea of using vortex generators is to create co-rotating or counter-rotating vortices and thus to enhance the exchange of momentum between the near-wall region and the outer flowfield. Storm et al. (1995) tested the airfoil with vortex generators attached to the leading edge of the flap at 10% flap chord and Gurney-flap-type tabs (see Fig. 2-7) placed in the cove region. Flow remained fully attached about the upper surface of the flap at 8° angle of attack with the free flow Mach number of 0.2, yielding a lift increase of about 30%. But on the other hand, their results also indicated that the cove tab had negative effects at low flap deflections. The recent contribution to this subject, conducted by Godard et al (2006), is the optimization of three different vortex generators. They are passive vortex generators which are usually an array of thin plates that have triangular or trapezoidal shape, and slotted/round jets vortex generators which introduce continuous blowing through rectangular/round holes. For the passive vortex generators, a significant improvement of the wall skin friction was obtained and the test results also showed the counter-rotating actuators were more effective in contrast to the co-rotating one. For the slotted jets vortex generators, both steady and pulsing blow were tested and did not yield any encouraging results. In addition, the pulsing blowing device seemed less effective than the steady jet, no matter what the pulsed frequency was. And for the round jets vortex generators, much significant increase of the skin friction was observed compared to passive devices of the same arrangement, thereby showing a brighter future than the other two configurations.

For the upper-surface blowing concepts, early studies can be traced back to 1950s. Williams and Alexander (1956) tested an 8% thick aerofoil with trailing-edge flap blowing. Results showed that significant lift improvement could be obtained and the blowing “was quite effective for flap angles up to 45°.” Turner (1972) investigated the longitudinal aerodynamic characteristics of an airfoil with aspect ratio of 4.735 and a 9.8% chord blowing flap which was a plain flap with blowing gap located to its front. Both the C_L curve slope and C_{Lmax} increased

with the momentum coefficient C_μ. Ground effect was also studied. Because this configuration does not have cove region between the main wing and the flap, acoustic benefits could be achieved simultaneously. Weaver et al. (1995) tested the upper-surface blowing on a VR-7 airfoil (see Fig. 2-8) in U.S. Army Aeroflightdynamics Directorate (AFDD) closed-circuit water tunnel at the NASA Ames Research Center. The test Reynolds number Re=1×10^5 based on the incoming flow condition and the chord length. Both steady and pulsed blowing methods were measured in the test while the blowing slot located at the quarter chord. As results showed, even though the steady blowing could not prevent the separation from happening if the separation occurred before the blowing slot, the blowing could still trap the separation bubble at the leading edge, hence significant lift enhancement was obtained. Best results were observed at the highest jet momentum. Pulsed blowing yielded similar results as the steady blowing and "a slight advantage in terms of hysteresis reduction and lift augmentation" was captured at a specific pulsing frequency.

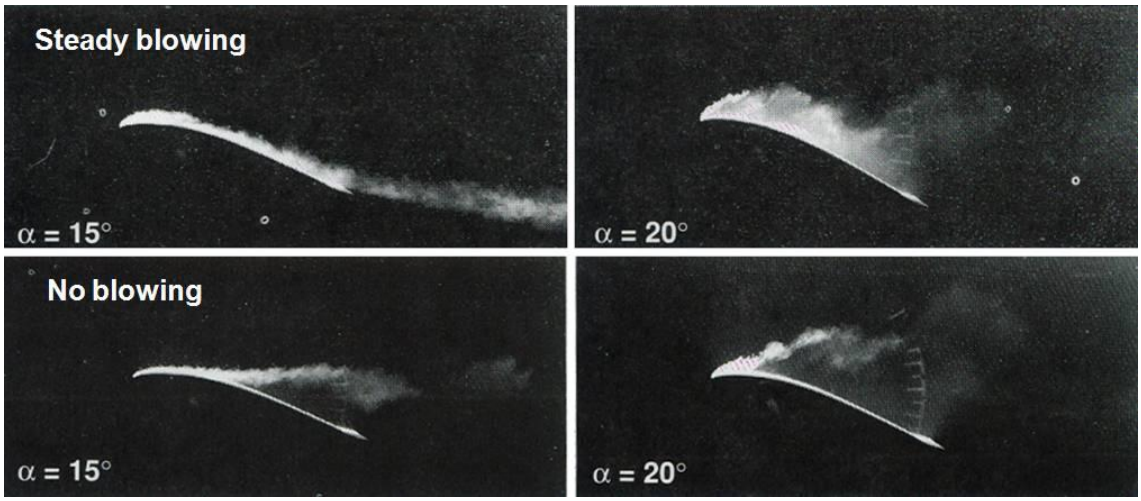

Figure 2-8 Flow visualisation of airfoil with/without steady blowing

[Weaver, et al. (1996)]

Recent interests of separation control using computational approaches are mainly focused on oscillatory blowing, e.g. the synthetic and pulsating jets. Using incompressible URANS code and Spalart-Allmaras one-equation turbulence model, Ekaterinaris (2004) simulated the flow over the TAU-0015 airfoil with pulsating jet flow control slat applied at the leading edge.

Computational prediction had a good agreement with the experiment, and “high grid resolution in the vicinity of the jet port is needed for accurate simulation of flow control.” Results also showed that the pulsating jet was capable to effectively control mildly separation, but cannot be able to prevent separation from happening at high angle of attack.

2.5 Summary

Several conclusions can be drawn from previous works:

1. Contemporary high-lift designs can greatly increase the maximum lift coefficient of the wing when those devices are deployed. But on the other hand, these designs also leave a large room for improvement.

2. Employing variable-camber flap concept can further increase the flap efficiency by fulfilling full-envelop requirements. But avoiding flow separations about the main wing and the high-lift system are the key issue in achieving better lift performance and other potential benefits at low speed, while maintaining less system complexity.

3. When the aircraft fly at a low angle of attack, flow separation may only occur about the upper surface of the flap. For higher angle of attack, especially near the maximum lift, the separation is caused by both “the flap boundary layer separation” and “the breakdown of the wake of the main wing above the flap,” according to van der Burg et al (2004).

4. For high-lift prediction, both the experimental and computational approaches have their inherent uncertainties, and no agreement has been reached on how to narrow this gap when separation occurs. RANS code with SA turbulence model can properly simulate the flow at a low angle of attack, but the C_{Lmax} and α_{CLmax} predictions are usually overpredicted.

5. Flow control devices have been proved to be effective of preventing flow from separating under certain conditions. Several concepts have been studied and each has its own advantages and disadvantages. They can be

divided into two major categories including passive actuation devices and active control devices.

6. For steady blowing, the momentum coefficient C_μ has been realised to be the key parameter of this control method. Besides, the blowing slot which maintains the profile shape of the airfoil can prevent the drag penalty at low incidence, as discussed by Weaver et al (1996).

3 Review of CFD

3.1 Governing Equations

The fundamental governing equations of fluid dynamics, which are also known as Navier-Stokes equations, include mass, momentum and energy conservation laws. They can be derived from applying these physical principles to a finite control volume of fluid or an infinitesimal fluid element. Two different basic forms of the governing equations can be derived, which are the conservation form and the non-conservation form. Besides, the governing equations can be written as either integral equations or differential equations.

For an unsteady, three-dimensional, compressible, viscous flow, the Navier-Stokes equations of the conservation form can be described by the same generic equation:

$$\frac{\partial \boldsymbol{U}}{\partial t}+\frac{\partial \boldsymbol{F}}{\partial x}+\frac{\partial \boldsymbol{G}}{\partial y}+\frac{\partial \boldsymbol{H}}{\partial z}=\boldsymbol{J} \tag{3-1}$$

where

$$\boldsymbol{U}=\begin{Bmatrix}\rho\\ \rho u\\ \rho v\\ \rho w\\ \rho\left(e+\frac{V^2}{2}\right)\end{Bmatrix},\quad \boldsymbol{F}=\begin{Bmatrix}\rho u\\ \rho u^2+p-\tau_{xx}\\ \rho vu-\tau_{xy}\\ \rho wu-\tau_{xz}\\ \rho\left(e+\frac{V^2}{2}\right)u+pu-k\frac{\partial T}{\partial x}-u\tau_{xx}-v\tau_{xy}-w\tau_{xz}\end{Bmatrix}$$

$$\boldsymbol{G}=\begin{Bmatrix}\rho v\\ \rho uv-\tau_{yx}\\ \rho v^2+p-\tau_{yy}\\ \rho wv-\tau_{yz}\\ \rho\left(e+\frac{V^2}{2}\right)w+pv-k\frac{\partial T}{\partial y}-u\tau_{yx}-v\tau_{yy}-w\tau_{yz}\end{Bmatrix}$$

$$\boldsymbol{H}=\begin{Bmatrix}\rho w\\ \rho uw-\tau_{zx}\\ \rho vw-\tau_{zy}\\ \rho w^2+p-\tau_{zz}\\ \rho\left(e+\frac{V^2}{2}\right)w+pw-k\frac{\partial T}{\partial z}-u\tau_{zx}-v\tau_{zy}-w\tau_{zz}\end{Bmatrix}$$

$$\boldsymbol{J} = \begin{Bmatrix} 0 \\ \rho f_x \\ \rho f_y \\ \rho f_z \\ \rho\left(u f_x + v f_y + w f_z\right) + \rho \dot{q} \end{Bmatrix}$$

For Newtonian fluids, the shear stresses can be written as:

$$\tau_{xx} = \lambda(\nabla \cdot \boldsymbol{V}) + 2\mu \frac{\partial u}{\partial x}$$

$$\tau_{yy} = \lambda(\nabla \cdot \boldsymbol{V}) + 2\mu \frac{\partial v}{\partial y}$$

$$\tau_{zz} = \lambda(\nabla \cdot \boldsymbol{V}) + 2\mu \frac{\partial w}{\partial z}$$

$$\tau_{xy} = \tau_{yx} = \mu\left(\frac{\partial \mathrm{v}}{\partial \mathrm{x}} + \frac{\partial \mathrm{u}}{\partial \mathrm{y}}\right)$$

$$\tau_{xz} = \tau_{zx} = \mu\left(\frac{\partial \mathrm{u}}{\partial \mathrm{z}} + \frac{\partial \mathrm{w}}{\partial \mathrm{x}}\right)$$

$$\tau_{yz} = \tau_{zy} = \mu\left(\frac{\partial \mathrm{w}}{\partial \mathrm{y}} + \frac{\partial \mathrm{v}}{\partial \mathrm{z}}\right)$$

There are six variables in Navier-Stokes equations which contain only five different equations. The system is closed by the so-called equation of state, which in the present study is given by:

Thermal equation of state: $p = \rho RT$

For incompressible flows, the continuity equation and momentum equation can be simplified and displayed in tensorial form as:

$$\frac{\partial u_j}{\partial x_j} = 0 \qquad \textbf{(3-2)}$$

$$\frac{\partial u_i}{\partial t}+\frac{\partial u_i u_j}{\partial x_j}=-\frac{1}{\rho}\frac{\partial p}{\partial x_i}+\nu\frac{\partial^2 u_i}{\partial x_j^2} \quad \textbf{(3-3)}$$

where i, j ≡1,2,3 indicating the x, y, z directions respectively.

3.2 Levels of Approximation

Generally, the Navier-Stokes equations are capable of describing any scale of turbulent flow. The Direct Numerical Simulation (DNS) resolves all scales of turbulent thus detailed flow field simulation can be obtained. But in reality, this involves enormous number of points and unbelievably long CPU time due to the current computer capacity. Hoffmann (2000) estimated in his book: "For the three-dimensional DNS of turbulent boundary layer with Re_δ=5000, the number of grid points would be around 4.5×10^{10}." Therefore, this method is strictly limited to certain research areas and is thought to be impractical for engineering problems.

Then, a question arises: what variables and information should be included for the affordable and "accurate" solution? In his book, Sagaut (2006) gave a very good description for this issue: "what is wanted now is evidence that certain phenomena exist, rather than all the physical mechanisms at play." As long as certain scale of phenomena are taken into account, the physical model of flow which governed by the Navier-Stokes equations can fall into different levels of approximation.

Given by Ferziger (1997), these are five major categories of approximation:

1. Direct Numerical Simulation of Navier-Stokes Equations (DNS)
2. Large Eddy Simulations (LES)
3. Reynolds-Averaged Navier-Stokes Equations (RANS)
4. Integral Methods
5. Correlation Methods

Hirsch (2007) categorized the levels of approximation in further details, as shown in Fig. 3-1.

No matter how we rank and name those methods, the key issue is always the trade-off of CPU time and accuracy, and the difficulty of grid generation should be taken into consideration, too. All the researches in this thesis are based on RANS approach. Brief review of different numerical and turbulence modelling methods are presented in the following chapters.

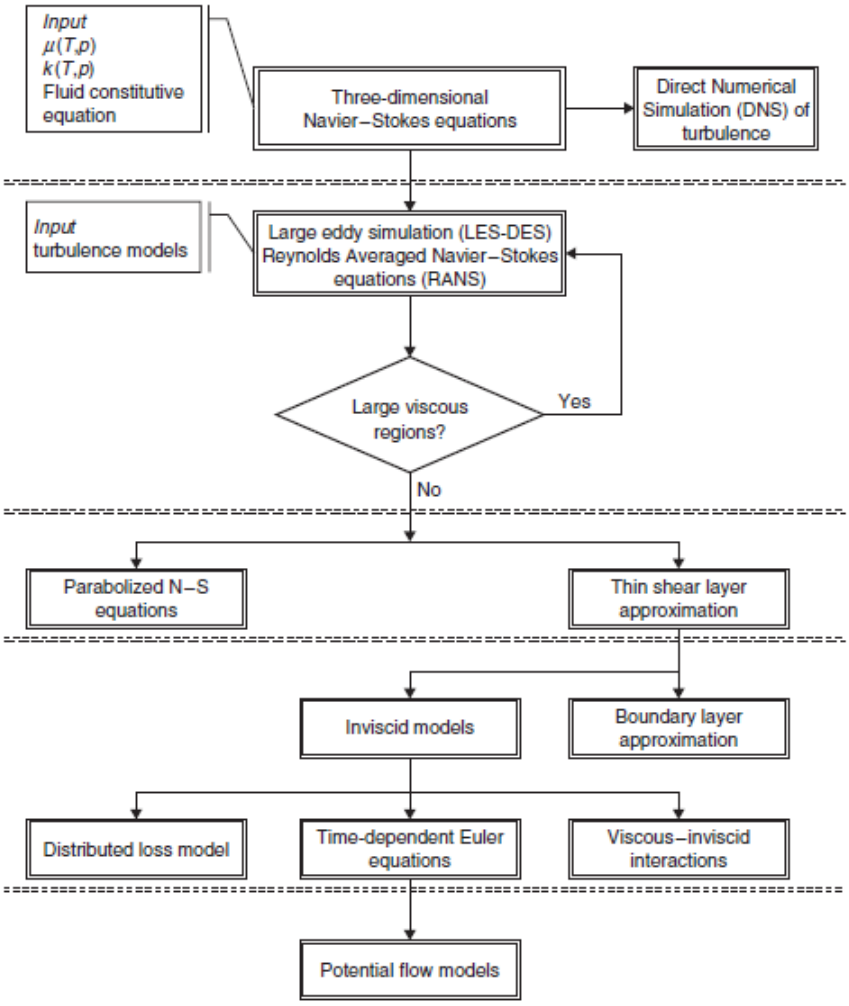

Figure 3-1 Different levels of approximation

3.2.1 Direct Numerical Simulation (DNS)

As mentioned, the Direct Numerical Simulation (DNS) resolves all scales of turbulent without using any simplification or assumption of turbulence, and is the most time-consuming methods. Though it is still not suitable for engineering

purpose, some successful examples of using DNS methods are presented in recent years showing its great potential.

Shan, Jiang and Liu (2005) used two- and three-dimensional DNS for studying the flow separation and transition around a NACA 0012 airfoil with the Reynolds number of 105. They successfully captured “the details of the flow separation, detached shear layer, vortex shedding, breakdown to turbulence, and re-attachment of the boundary layer.”

Lamballais, Silvestrini and Laizet (2008) predicted the separation bubble on a generic half-body with a rounded edge through DNS approach. The Reynolds number of their research is Re=1250. The results are “found to be consistent with experiments,” and are the “complement to the experiments.”

3.2.2 Large Eddy Simulation (LES)

Like the Direct Numerical Simulation, Large Eddy Simulation (LES) directly resolves the turbulence, but to a limited range of turbulent scale. This makes it less “expensive” than DNS while maintaining higher level of accuracy and reliability compared to contemporary methods, i.e. Reynolds-Averaged Navier-Stokes Equations (RANS). Because LES approach only simulates “large” scales of turbulent, this makes it much “affordable.” But still, the LES approach is too demanding when predicting the high-Reynolds flow. On the other hand, LES methods rely on the definition of large and small scales. Sagaut (2006) described this definition as a “fuzzy and empirical concept” which still needs “further discussion”. Besides, averaged forms of the equations are employed so as to simulate the “small” scales of turbulent. So, similar to the RANS, the LES also includes turbulence models.

3.2.3 Reynolds-Averaged Navier-Stokes Equations (RANS)

Due to the high cost of resolving the turbulent directly, RANS approach has been widely used in industry for a long time and the confidence of yielding adequate prediction of the flow field through this method has been gradually built. The basis of RANS approach is the Reynolds averaging (or decomposition)

of the flow variables (i.e. $u_i(x,t)$), which breaks them into the time-averaged components ($\overline{u}_i(x)$) and the fluctuating components ($u_i'(x,t)$). Thus, the flow variables can be described as:

$$p(\boldsymbol{x},t) = \overline{p}(\boldsymbol{x}) + p'(\boldsymbol{x},t) \tag{3-4}$$

$$u_i(\boldsymbol{x},t) = \overline{u}_i(\boldsymbol{x}) + u_i'(\boldsymbol{x},t) \tag{3-5}$$

where the time-averaged components are:

$$\overline{u}_i(\boldsymbol{x}) = \lim_{T\to\infty}\frac{1}{T}\int_t^{t+T} u_i(\boldsymbol{x},t)dt \tag{3-6}$$

$$\overline{p}_i(\boldsymbol{x}) = \lim_{T\to\infty}\frac{1}{T}\int_t^{t+T} p_i(\boldsymbol{x},t)dt \tag{3-7}$$

For incompressible flow, RANS equations can be obtained by time averaging (3-2) and (3-3):

$$\frac{\partial \overline{u}_j}{\partial x} = 0 \tag{3-8}$$

$$\frac{\partial \overline{u}_i}{\partial t} + \frac{\partial \overline{u}_i \overline{u}_j}{\partial x_j} = -\frac{1}{\rho}\frac{\partial \overline{p}}{\partial x_i} + \nu\frac{\partial^2 u_i}{\partial x_i^2} - \frac{\partial \overline{u_i' u_j'}}{\partial x_j} \tag{3-9}$$

where $-\overline{u_i' u_j'}$ is known as the specific Reynolds-stress tensor (τ_{ij}).

Though the RANS approach which does not solve the turbulent motion of small scales successfully makes the CFD applications much affordable, it does has its own weak point. Additional variables (the specific Reynolds-stress tensor: $-\overline{u_i' u_j'}$) ,which need to be defined, are generated while averaging the Navier-Stokes equations. The common way of solving this closure problem is employed a turbulence model which establishes certain relationship of presenting the specific Reynolds-stress tensor (τ_{ij}).

3.3 RANS-based turbulence simulation

3.3.1 Boussinesq hypothesis

The Boussinesq hypothesis, which is the basis of most turbulence models, assumes that the specific Reynolds-stress tensor (τ_{ij}) can be represented as the product of the eddy viscosity and the mean strain-rate tensor:

$$\tau_{ij} = \frac{2}{\rho}\mu_t S_{ij} - \frac{2}{3}k\delta_{ij} \quad \textbf{(3-10)}$$

Where S_{ij} is the mean strain-rate tensor and the μ_t is known as the eddy viscosity. For a compressible flow, S_{ij} is defined as:

$$S_{ij} = \frac{\partial \overline{u}_i}{\partial x_j} + \frac{\partial \overline{u}_j}{\partial x_i} - \frac{2}{3}\frac{\partial \overline{u}_k}{\partial x_k}\delta_{ij} \quad \textbf{(3-11)}$$

And for an incompressible flow, $\frac{\partial \overline{u}_k}{\partial x_k}$ will be zero, and thus S_{ij} can be written as:

$$S_{ij} = \frac{\partial \overline{u}_i}{\partial x_j} + \frac{\partial \overline{u}_j}{\partial x_i} \quad \textbf{(3-12)}$$

3.3.2 Spalart-Allmaras turbulence model

The Spalart–Allmaras (SA) one-equation model was first presented by Spalart and Allmaras (1992). In SA model, the eddy viscosity (μ_t) is written as:

$$\mu_t = \rho\tilde{\nu}f_{v1} \quad \textbf{(3-13)}$$

The modified turbulent kinematic viscosity, $\tilde{\nu}$, in equation (3-13) can be obtained through solving its transport equation:

$$\frac{\partial}{\partial t}(\rho\tilde{\nu}) + \frac{\partial}{\partial x_i}(\rho\tilde{\nu}u_i) = G_v + \frac{1}{\sigma_{\tilde{\nu}}}\left[\frac{\partial}{\partial x_j}\left\{(\mu + \rho\tilde{\nu})\frac{\partial \tilde{\nu}}{\partial x_j}\right\} + C_{b2\rho}\left(\frac{\partial \tilde{\nu}}{\partial x_j}\right)^2\right] - Y_v \quad \textbf{(3-14)}$$

where G_ν and Y_ν represent the production and the destruction of turbulent viscosity, respectively. They are modelled as:

$$G_\nu = C_{b1}\rho\tilde{S}\tilde{\nu}, \qquad Y_\nu = C_{w1}\rho f_w\left(\frac{\tilde{\nu}}{d}\right)^2 \tag{3-15}$$

Closure coefficients and auxiliary relations are:

$$C_{b1} = 0.1355, \qquad C_{b2} = 0.622, \qquad \delta_{\tilde{\nu}} = \frac{2}{3}, \qquad C_{v1} = 7.1 \tag{3-16}$$

$$C_{w1} = \frac{C_{b1}}{\kappa^2} + \frac{(1+C_{b2})}{\sigma}, \qquad C_{w2} = 0.3, \qquad C_{w3} = 2.0, \qquad \kappa = 0.4187 \tag{3-17}$$

$$f_{v1} = \frac{\chi^3}{\chi^3 + C_{v1}^3}, \qquad f_{v2} = 1 - \frac{\chi}{1+\chi f_{v1}}, \qquad f_w = g\left[\frac{1+C_{w3}^6}{g^6 + C_{w3}^6}\right]^{1/6} \tag{3-18}$$

$$\chi = \frac{\tilde{\nu}}{\nu}, \qquad g = r + C_{w2}(r^6 - r), \qquad r = \frac{\tilde{\nu}}{\tilde{S}\kappa^2 d^2} \tag{3-19}$$

With all these equations and coefficients set, the RANS equations can now be solved.

3.3.3 The k-ϵ turbulence model

As the most popular two-equation model, k-ϵ turbulence model has been used in engineering field for decades. Unlike the SA model which only introduces one variable ($\tilde{\nu}$) to describe the eddy viscosity, the standard k-ϵ model computed the turbulence viscosity by introducing two variables: the turbulence kinetic energy (k) and the turbulence dissipation rate (ϵ), as proposed by Launder and Spalding (1974). The relationship is written as:

$$\mu_t = \rho C_\mu \frac{k^2}{\epsilon} \tag{3-20}$$

These two variables are obtained from the following equations:

$$\frac{\partial k}{\partial t}+\bar{u}_j\frac{\partial k}{\partial x_j}=\frac{\partial}{\partial x_j}\left[\frac{1}{\rho}\left(\mu+\frac{\mu_t}{\sigma_k}\right)\frac{\partial k}{\partial x_j}\right]-\epsilon+\tau_{ij}\frac{\partial \bar{u}_i}{\partial x_j} \quad \textbf{(3-21)}$$

and

$$\frac{\partial \epsilon}{\partial t}+\bar{u}_j\frac{\partial \epsilon}{\partial x_j}=\frac{\partial}{\partial x_j}\left[\frac{1}{\rho}\left(\mu+\frac{\mu_t}{\sigma_k}\right)\frac{\partial \epsilon}{\partial x_j}\right]-C_{2\epsilon}\frac{\epsilon^2}{k}+C_{1\epsilon}\frac{\epsilon}{k}\tau_{ij}\frac{\partial \bar{u}_i}{\partial x_j} \quad \textbf{(3-22)}$$

Closure coefficients and auxiliary relations of the standard k-ϵ model includes:

$$C_{\epsilon 1}=1.44,\quad C_{\epsilon 2}=1.92,\quad C_\mu=0.09,\quad \sigma_k=1.0,\quad \sigma_\epsilon=1.3 \quad \textbf{(3-23)}$$

Another version of the k-ϵ turbulence model is the RNG k-ϵ model. Like the standard model, the RNG k-ϵ model also represents the turbulence viscosity by the turbulence kinetic energy (k) and the turbulence dissipation rate (ϵ), but a modified coefficient ($C_{\epsilon 2}$) is employed and defined as:

$$C_{\epsilon 2}=\tilde{C}_{\epsilon 2}+\frac{C_\mu\lambda^3(1-{}^{\lambda}/_{\lambda_0})}{1+\beta\lambda^3},\qquad \lambda=\frac{k}{\epsilon}\sqrt{2S_{ij}S_{ji}} \quad \textbf{(3-24)}$$

And the closure coefficients for the RNG k-ϵ model has become:

$$C_{\epsilon 1}=1.42,\quad \tilde{C}_{\epsilon 2}=1.68,\quad C_\mu=0.085,\quad \sigma_k=0.72,\quad \sigma_\epsilon=0.72 \quad \textbf{(3-25)}$$

$$\beta=0.012,\quad \lambda_0=4.38 \quad \textbf{(3-26)}$$

3.3.4 The k-ω turbulence model

Like the k-ϵ model, k-ω model also uses two variables to represent the eddy viscosity: the turbulence kinetic energy (k) and the specific dissipation rate (ω). Then the eddy viscosity (μ_t) is defined as:

$$\mu_t = \frac{\rho k}{\tilde{\omega}}, \qquad \tilde{\omega} = max\left\{\omega, C_{lim}\sqrt{\frac{2S_{ij}S_{ij}}{\beta^*}}\right\}, \qquad C_{lim} = \frac{7}{8} \tag{3-27}$$

Two transport equations for each variable are:

$$\frac{\partial k}{\partial t} + \bar{u}_j\frac{\partial k}{\partial x_j} = \frac{\partial}{\partial x_j}\left[\left(\nu + \sigma^*\frac{k}{\omega}\right)\frac{\partial k}{\partial x_j}\right] - \beta^* k\omega + \tau_{ij}\frac{\partial \bar{u}_i}{\partial x_j} \tag{3-28}$$

$$\frac{\partial \omega}{\partial t} + \bar{u}_j\frac{\partial \omega}{\partial x_j} = \frac{\partial}{\partial x_j}\left[\left(\nu + \sigma\frac{k}{\omega}\right)\frac{\partial \omega}{\partial x_j}\right] - \beta\omega^2 + \frac{\sigma_d}{\omega}\frac{\partial k}{\partial x_j}\frac{\partial \omega}{\partial x_j} + \alpha\frac{\omega}{k}\tau_{ij}\frac{\partial \bar{u}_i}{\partial x_j} \tag{3-29}$$

Closure coefficients and auxiliary relations are:

$$\alpha = \frac{13}{25}, \qquad \beta = \beta_o f_\beta, \qquad \beta^* = \frac{9}{100}, \qquad \sigma = \frac{1}{2}, \qquad \sigma^* = \frac{3}{5}, \qquad \sigma_{do} = \frac{1}{8} \tag{3-30}$$

$$\sigma_d = \begin{cases} 0, & \dfrac{\partial k}{\partial x_j}\dfrac{\partial \omega}{\partial x_j} \le 0 \\ \sigma_{do}, & \dfrac{\partial k}{\partial x_j}\dfrac{\partial \omega}{\partial x_j} > 0 \end{cases} \tag{3-31}$$

$$\beta_o = 0.0708, \qquad f_\beta = \frac{1 + 85\chi_\omega}{1 + 100\chi_\omega}, \qquad \chi_\omega = \left|\frac{\Omega_{ij}\Omega_{jk}S_{ki}}{(\beta^*\omega)^3}\right| \tag{3-32}$$

The Ω_{ij} and S_{ij} represent the mean-rotation tensor and the mean-strain-rate tensor, respectively.

4 Representation Models and Simulation Description

In this chapter, four different representation models are described. Each model has been analyzed using CFD approaches. The simulation condition and methodology of prediction are also presented, including typical calculation procedures. This is followed by a description of the grid strategy. The methods of Postprocessing are given in the last section.

4.1 Representation models and case setting

As previously discussed, separation on the flap usually happens at a low angle of attack rather than at high incidence. The deflection angle of the flap also plays an important role. Besides this, the separation is highly Reynolds number dependent and is more likely to happen when the Reynolds number is low. Taking all these factors into consideration, this study should be carried out for typical landing conditions as then the flaps are usually fully extended and the aeroplane flies at low air speed.

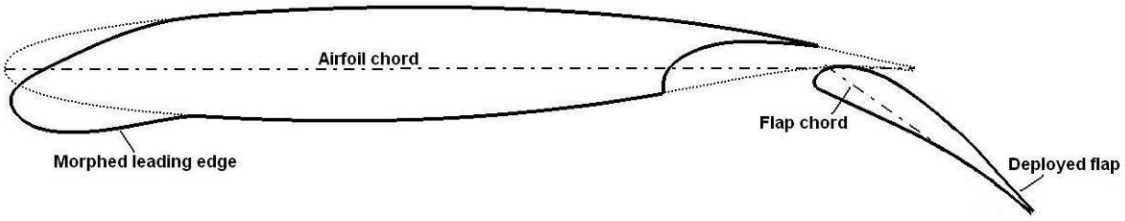

(a) Normal flap model (Case I)

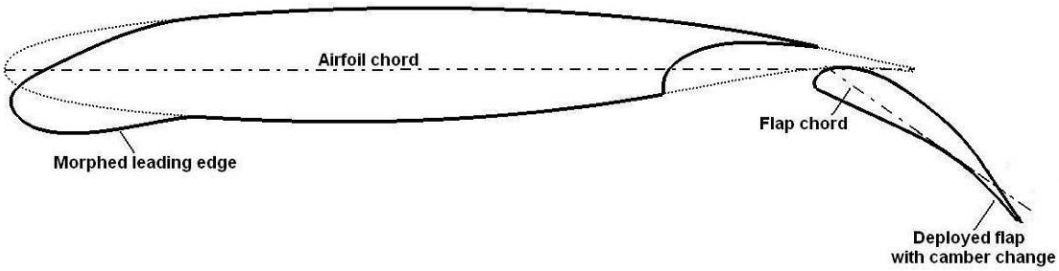

(b) High-camber flap model (Case II)

Figure 4-1 Baseline airfoils

Two baseline models have been chosen for this study as shown in Fig. 4-1. These airfoils are designed to be used on short- to medium-range commercial airliner, e.g. the Airbus A320. The key features of these models include:

a. Each model has a deployed flap which has a deflection angle of 35°. The first model named as normal flap model (see Fig. 4-1.a) has a conventional flap while the second model (see Fig. 4-1.b) has a high-camber flap and is named after this feature. A better understanding of camber related stall of the flap can be developed through comparing the results of these two cases.

b. Each baseline case has a drooped leading edge slat. As reduction of the complexity and noise level is gradually becoming the trend of high-lift design, including a morphed leading edge will also benefit further studies.

As the baseline cases have been settled, the next job is to develop the blowing study cases. In the scope of this thesis, blowing slot has been fixed on the upper-surface of the flap at 25%c_{flap} (see Fig. 4-2.a). The slot is also defined by the slot height, h. Two different types of blowing have been studied: tangential blowing and non-tangential blowing. The tangential blowing has been introduced by aligning the blowing slot to the local airfoil shape. The non-tangential blowing is fulfilled by placing the blowing slot at an angle of 20° against the local tangent. Both slots have the same height. For the tangential blowing, part of the airfoil has been modified (see Fig. 4-2.b) as the slot is placed beneath the original profile. But for the non-tangential blowing, only a small gap is added to the flap surface (see Fig. 4-2.c). Dimensions of the representation models are given in table 4-1.

Table 4-1 Airfoil and blowing slot dimensions

Airfoil chord, c	3.956m
Flap chord, c_{flap}	1.170m
Blowing slot height, h	0.003m

As 2 different blowing slot designs has been applied on case II, two more cases have been introduced. Thus four cases have been studied in this thesis. Features of all cases have been summarised in Table 4-2.

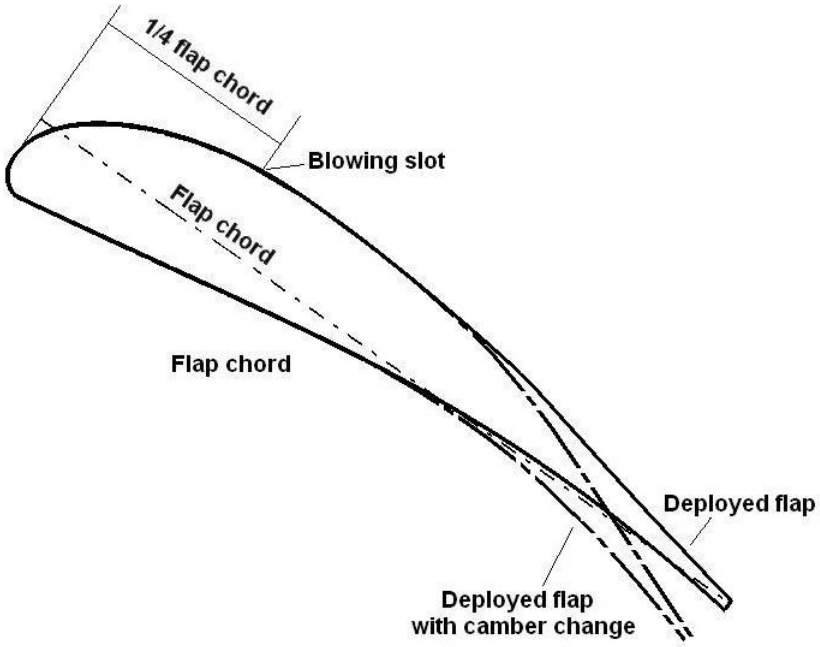

(a) Location of the blowing slot

(b) Close up view of the blowing slot (Tangential blowing)

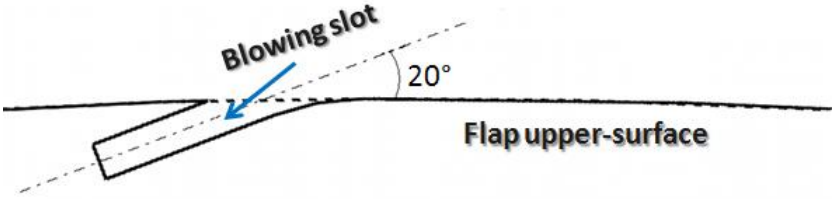

(c) Close up view of the blowing slot (Non-tangential blowing)

Figure 4-2 Location and shape of the blowing slot

Table 4-2 Case definition

Geometry	Leading edge	Flap		Blowing Slot
		Deflecting angle	Camber change	
Case I	Drooped	35°	No	No
Case II			Yes	No
Case III			Yes	Tangential blow
Case IV			Yes	Non-tangential blow

4.2 Simulation Conditions

The aerodynamic performance of each case was predicted using a freestream Mach number of 0.2 and a Reynolds number of 15.3×10^6 according to the freeflow velocity and the reference chord length. Series of angles of attack have been studied, too. For those blowing cases, effects of different blowing momentum coefficients have also been analyzed, as shown in Table 4-3. The blowing momentum coefficient, C_μ, is defined as:

$$C_\mu = 2\frac{h}{c}\cdot\left(\frac{V_s}{V_\infty}\right)^2 \quad \textbf{(4-1)}$$

where V_s is the jet velocity at the slot exit.

Table 4-3 Calculated conditions of each case

Geometry	M_∞	α	C_μ
Case I	0.2	4°, 8°, 12°	
Case II			
Case III	0.2	4°, 8°, 12°	*4 different C_μ*
Case IV			

4.3 Numerical method and turbulence model

All simulations were performed by solving the two-dimensional compressible RANS equations on multi-block structured grids. The commercial CFD software Fluent 12 was employed to obtain the solutions. For spatial discretization, the first-order upwind scheme was employed to perform the initial calculation and boost the convergence. Then, a higher-order third-order MUSCL scheme was used to achieve a better accuracy. Different simulation procedures are shown in Fig. 4-3.

The third-order MUSCL scheme combines the central-differencing scheme and the second-order upwind scheme and can be written as:

$$\phi_f = \theta\phi_{f,CD} + (1-\theta)\phi_{f,SOU} \tag{4-2}$$

where $\phi_{f,CD}$ is computed using the central-differencing scheme and is determined by following equation:

$$\phi_{f,CD} = \frac{1}{2}(\phi_0 + \phi_1) + \frac{1}{2}(\nabla\phi_0 \cdot \overrightarrow{r_0} + \nabla\phi_1 \cdot \overrightarrow{r_1}) \tag{4-3}$$

while $\phi_{f,SOU}$ is defined by the second-order upwind scheme and written as:

$$\phi_{f,SOU} = \phi + \nabla\phi \cdot \vec{r} \tag{4-4}$$

For turbulence modelling, the Spallart-Allmaras one-equation turbulence model has been used. The SA model can be written in terms of the modified turbulent kinematic viscosity, $\tilde{\nu}$, which is identical to the eddy viscosity in the none near-wall region. The $\tilde{\nu}$ can be obtained by solving its transport equation, as written in equation (3-14) and (3-15). The close coefficients and auxiliary relations are given by equation (3-16) to (3-19).

For the near-wall region, the modified turbulent kinematic viscosity, $\tilde{\nu}$, is set to zero and the wall shear stress is described by the laminar stress-strain relationship:

$$\frac{u}{u_\tau} = \frac{\rho u_\tau y}{\mu} \quad \textbf{(4-5)}$$

The numerical method and turbulence model were validated by performing simulations on the MDA 30P-30N multi-element airfoil. Prediction results were compared with experimental data. Two major factors which have been thought to have influences on prediction accuracy were highlighted in the validation phase, including far-field extent of the grid and the Reynolds number of simulation.

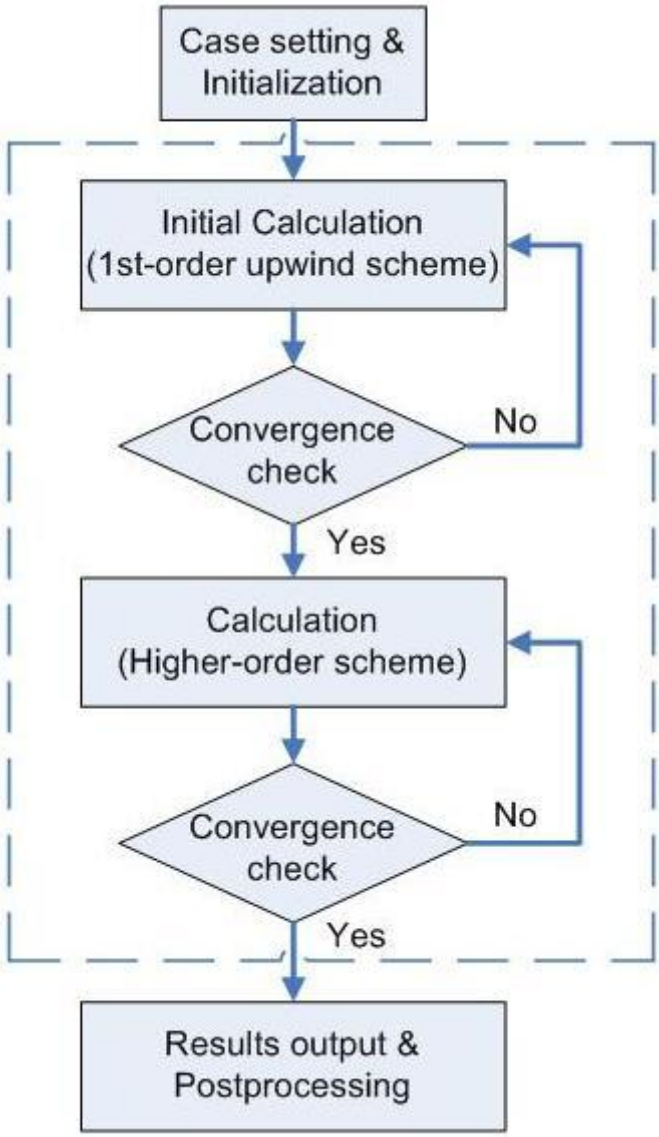

Figure 4-3 Flow chart of simulation

4.4 Grid Strategy

Multi-block structured grids were employed in this study. Though the grid was intended to be orthogonal to the airfoil surface, the complex geometry of high-lift airfoil made this hard to achieve. Grid node distribution was carefully adjusted so as to maintain acceptable grid skewness. As the main region of interest, the grids around the flap were also refined for both validation cases and study cases.

The numerical results for turbulence flows are susceptible to the near-wall grid resolution; hence sufficiently fine meshes should be used in these regions. On the other hand, fine meshes in the near-wall region are also a key factor in obtaining the full benefit of the Spalart-Allmaras model. Using y^+ ($y^+ \equiv \rho u_\tau y/\mu$) as a measurement, $y^+=1$ at the wall adjacent cell will be desirable. A higher y^+ is also acceptable as long as it is less than 4. In order to achieve this, the wall adjacent cell has been placed within the range of $\Delta y_1/c = 6 \times 10^{-6}$ for validation cases and $\Delta y_1/c = 2.5 \times 10^{-6}$ for study cases. The stretching ratio ($\Delta y_{j+1}/\Delta y_j$) equals 1.2 for all cases.

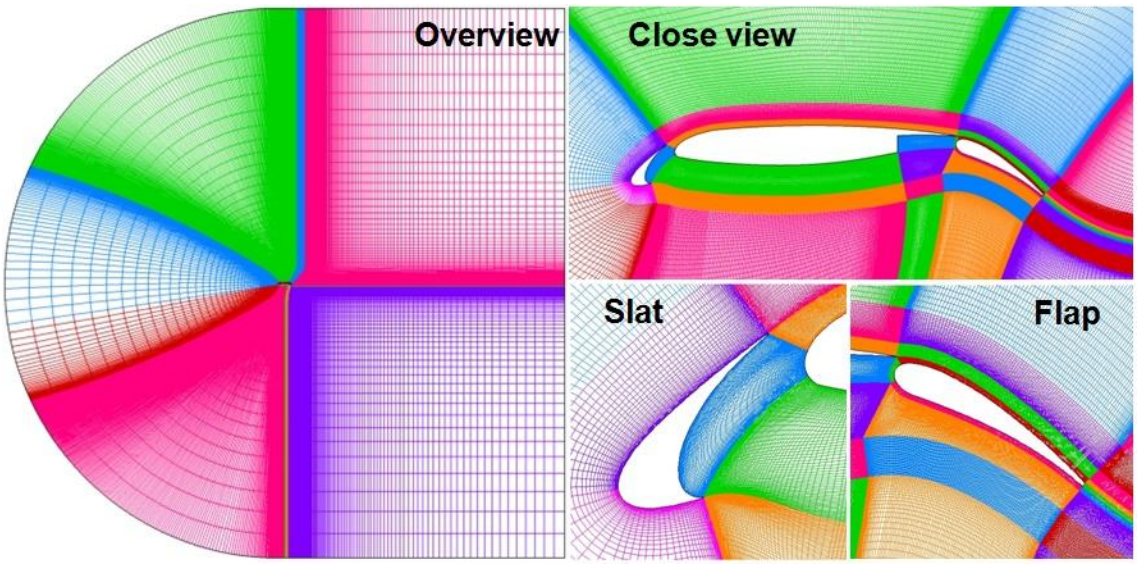

Figure 4-4 Grid for validation

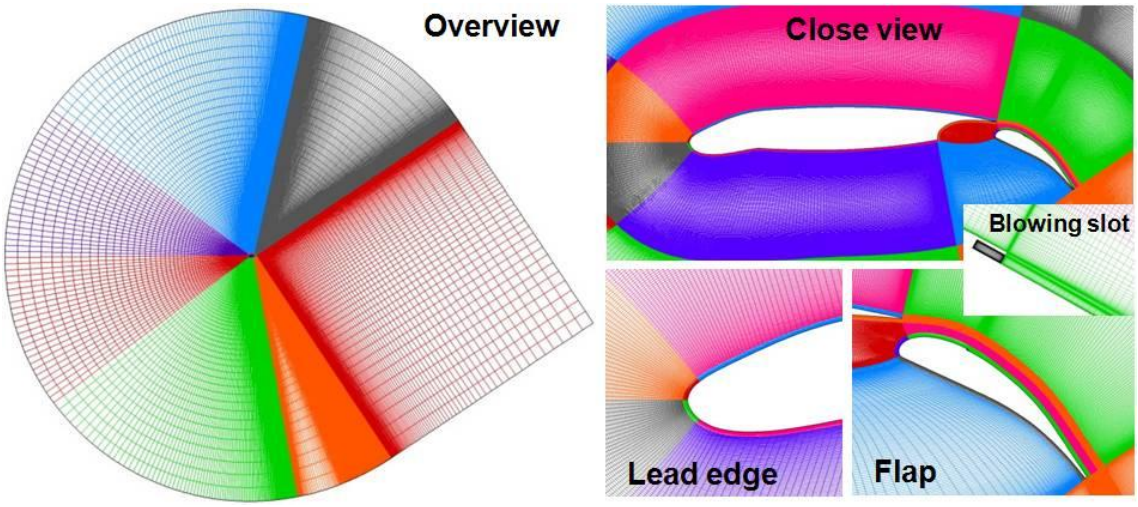

Figure 4-5 Grid for the case studies

In all six grids have been generated, two of which are used for numerical method validation, and the other four grids represent four different study cases. Details of each grid are described as follows:

a. Grid A and B (Fig. 4-4) were generated for the numerical method validation. Grid strategy and near-wall distribution are the same as discussed above. The only difference between these two is that Grid B has a far-field extent of 50 times of reference chord, whilst this is 25 for Grid A. As a result, the Grid A and B have 430,000 nodes and 464,000 nodes respectively.

b. Grids for the case studies comprise Grid I, II, III and IV, each named after the study case represented (Fig. 4-5). Both Grid I and II consist of 493,000 grid nodes, while for the Grids III and IV, to which extra 70,000 grid nodes have been added for blowing simulation, the quantity of grid nodes increases to 563,000.

4.5 Postprocessing

Both the validation work and the case studies involved Postprocessing. For the validation case, the calculated force coefficients, C_p distribution and velocity profiles were compared with experimental data and computed results from other research. Several rakes have been placed normal to the upper-surface of the

main wing and the flap, as shown in Fig. 4-6, for comparison of the velocity profile. These rakes are named according to the experimental data.

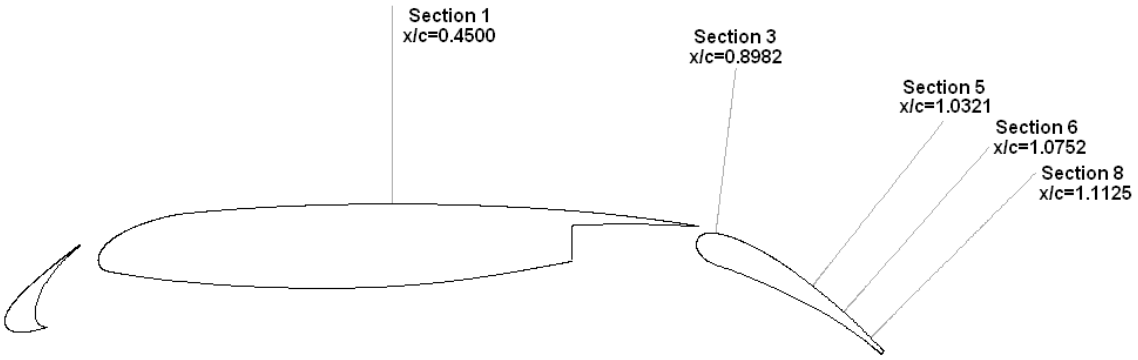

Figure 4-6 Location of rakes for validation

As with the validation work, the calculated force coefficients, C_p distribution were also compared during case study phase. But due to the lack of experimental data, only the prediction results of different configurations and conditions have been compared. Flow phenomena were illustrated by streamlines and contour plot. 8 rakes at different stations were placed for the velocity profile output (see Fig. 4-7). Tecplot was used for the graphical output.

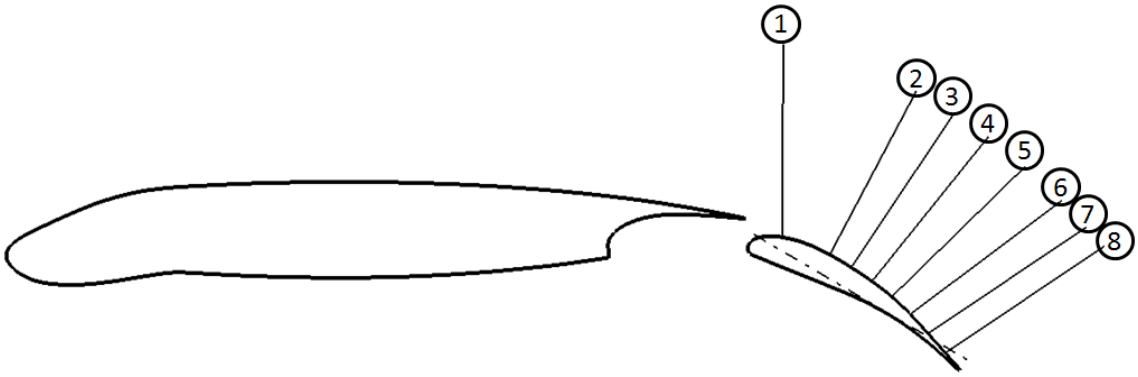

Rake	Position
1	x/c_{flap}=10%
2	x/c_{flap}=30%
3	x/c_{flap}=40%
4	x/c_{flap}=50%
5	x/c_{flap}=60%
6	x/c_{flap}=70%
7	x/c_{flap}=80%
8	x/c_{flap}=90%

Figure 4-7 Location of rakes for case study

5 Validation

The MDA 30P-30N airfoil was chosen to be the validation case, and the configuration definition of MDA 30P-30N airfoil can be found in table 5-1. Prediction results were compared both numerically and graphically. Experimental data used was obtained in the NASA Langley LTPT in 1992 and described in detail by Chin et al. Experimental data was documented and compared with computed results in ref.18. According to their report, good agreement was found between experimental data and prediction results from different codes. For the RANS methods, lift was often predicted more accurately than drag. Changes of lift and drag due to changes in Reynolds number could also be predicted well. The slat wake was predicted to be larger than it was measured in the experiment.

Table 5-1 Configuration definition of MDA 30P-30N multi-element airfoil

Slat Deflection	30°
Slat Gap	2.95%
Slat overhang	-2.5%
Flap Deflection	30°
Flap Gap	1.27%
Flap overhang	0.25%

5.1 Case setting

Simulations were carried out with a free-stream Mach number M_∞=0.2. Two Reynolds numbers have been tested, which were Re=5×10^6 and Re=9×10^6 based on the free flow condition and the reference chord length. For cases with Re=5×10^6, the simulated angle of attack was 8.12°. And for the case with Re=9×10^6, the angle of attack was set as 8.10°.

Validation work was performed in two stages, each analysing a highlighted parameter:

a. As mentioned, the far field grid extent has a huge impact on accuracy, especially for drag prediction. Two cases with different far field extent (*ffe*) have been generated and tested first. Case A has a *ffe* that equal 25 times the reference chord and the other (Case B) is 50 times the reference chord. Both simulations were performed with a Reynolds number of 5 million.

b. Based on the results of the first stage, a third validation case was introduced, which had the same *ffe* as which had proved better in stage one, but was simulated with a larger Reynolds number of 9 million.

Definitions of each case can be found in table 5-2.

Table 5-2 Definitions of validation cases

	M_∞	*ffe*	*Re*	α
Case A	0.2	25c	5 million	8.12°
Case B		50c	5 million	8.12°
Case C		50c	9 million	8.10°

5.2 Results and discussion

5.2.1 Influence of far field extent

Firstly, the residual of each computed variable was checked. They were all found to be around 1×10^{-6} or less. Lift and drag coefficients were monitored throughout the whole process to determine the convergence (see Fig. 5-1). Then the values of y^+ were checked (see Fig. 5-2). As all values were less than 2, both grids had been shown to be fine enough in the near wall region.

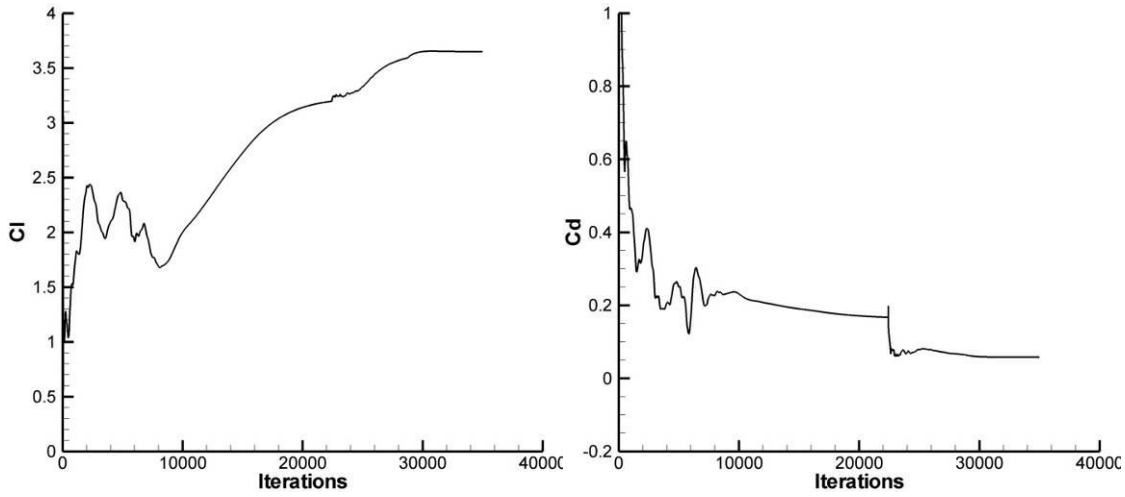

(a) Lift coefficient (b) Drag coefficient

Figure 5-1 Typical convergence histories (Case A)

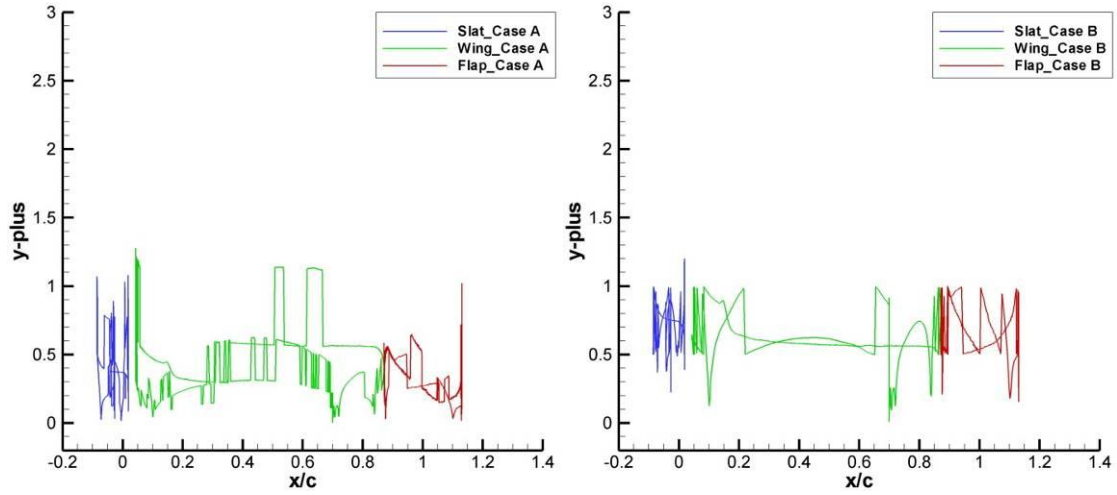

(a) Case A (b) Case B

Figure 5-2 Comparison of y^+ distributions

Calculated lift, drag and momentum coefficients were compared with experiment as shown in table 5-3. For every case, the lift coefficients were overpredicted by 6%. Similar results were obtained by comparing the momentum coefficients. For the drag coefficient prediction, the result of case B showed a better agreement with the experiment, although a large difference (31%) was found. As shown in Fig. 5-3, the experimental data was compared with the simulation results obtained by many other researchers using different RANS codes. For further information, please refer to Klausmeyer and Lin's report [24].

Table 5-3 Comparison between calculated coefficients and experimental data

	Re=5×10^6		
	Exp.	Case A	Case B
C_L	3.0841	3.2666	3.2754
$(C_L - C_{LExp})/ C_{LExp}$		+6%	+6%
C_D	0.0361	0.0519	0.0472
$(C_D - C_{DExp})/ C_{DExp}$		+44%	+31%
C_M	-0.5701	-0.6141	-0.6133
$\lvert(C_M - C_{MExp})/ C_{MExp}\rvert$		+8%	+8%

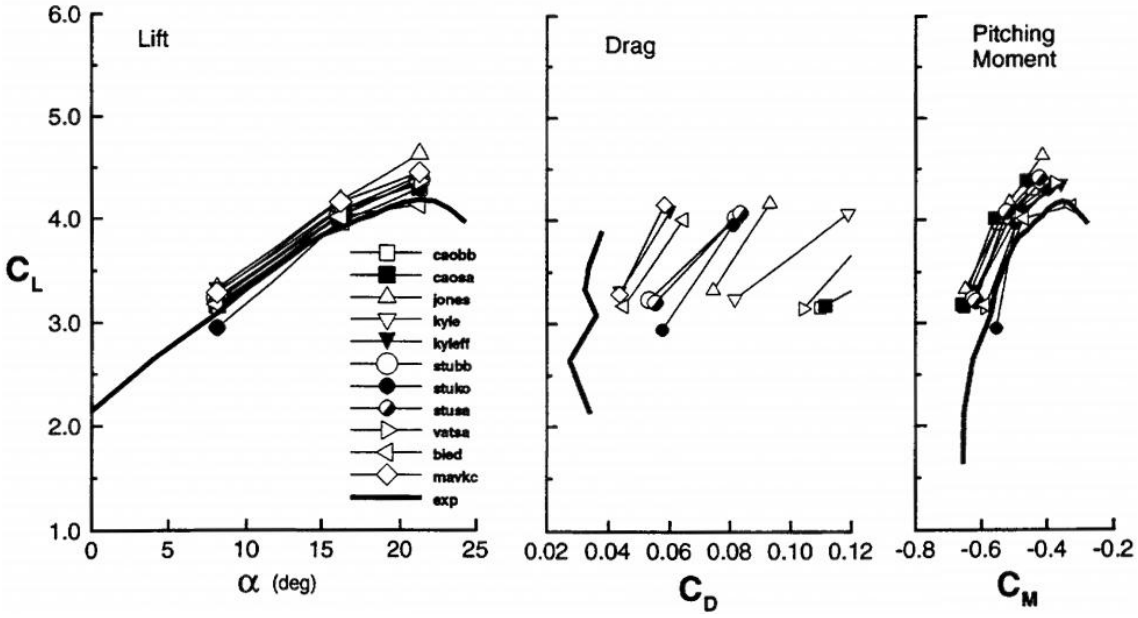

Figure 5-3 Calculated results and comparison to experiment (Re=5×10^6) [24]

The surface C_p distributions on different components were compared in Figure 5-4. Predicted results from other researches were also illustrated. As can clearly be seen, different cases produced similar results. In comparison to experimental data, the higher suction peak at the leading edge of the slat showed overpredicted acceleration of flow on the slat upper-surface (Fig. 5-4.a1) and

results from other cases showed a similar pattern. Predictions of the wing and flap had a better agreement with the experimental data.

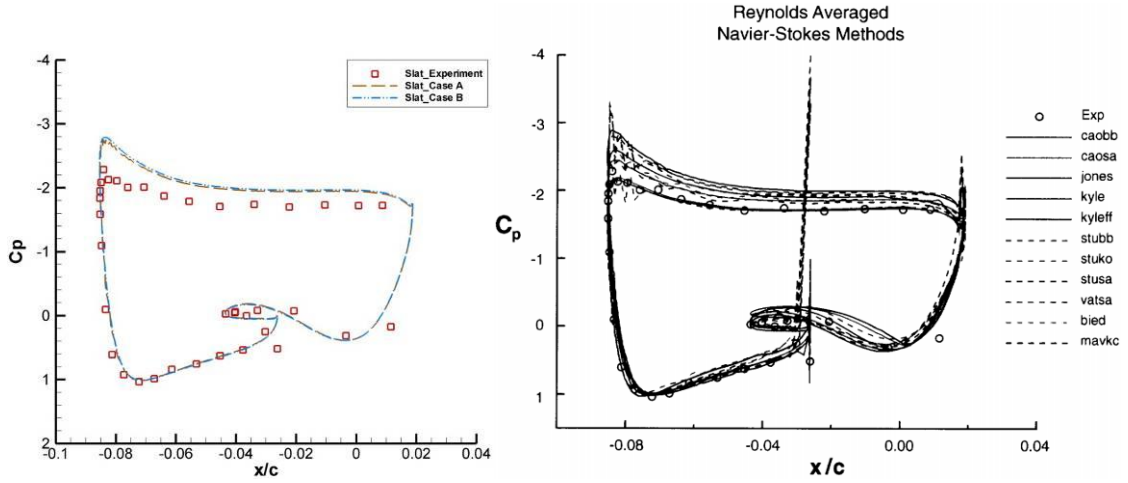

(a1) Validation (Slat) (a2) Results from other research

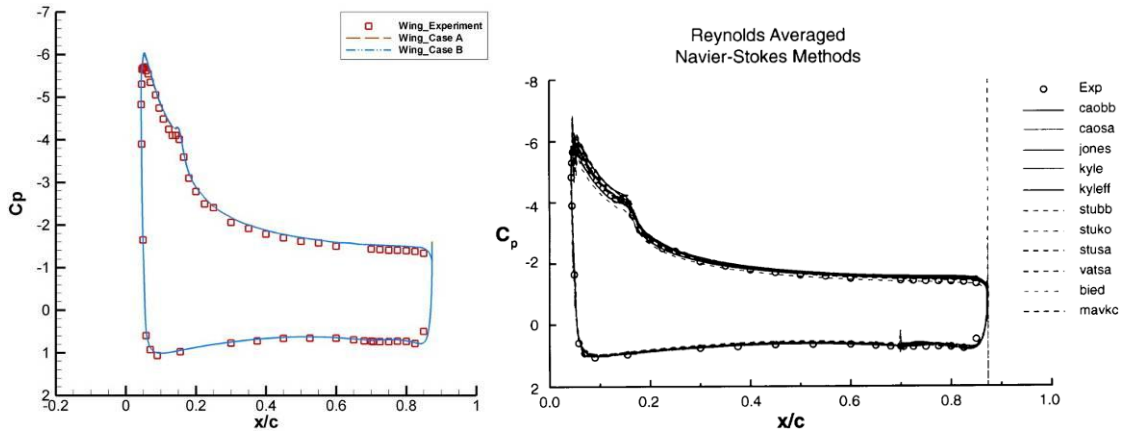

(b1) Validation (Wing) (b2) Results from other research

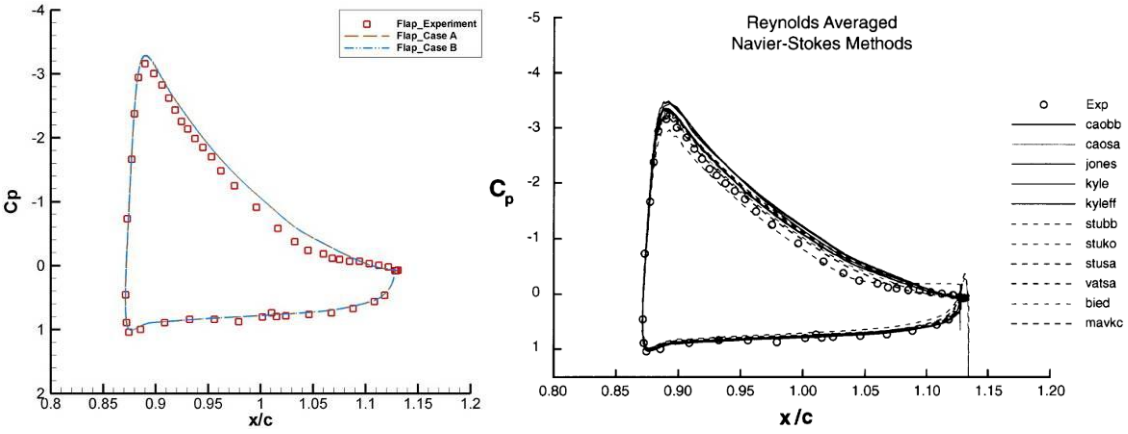

(c1) Validation (Flap) (c2) Results from other research

Figure 5-4 Comparison of surface C_p distribution

To further analyze the simulations, velocity profiles at different stations were compared and presented (see Fig. 5-5). Results from two grids matched each other well and also had good agreement with experiment, especially at station 3. This meant the flow through the cove region between the flap and the wing was predicted well.

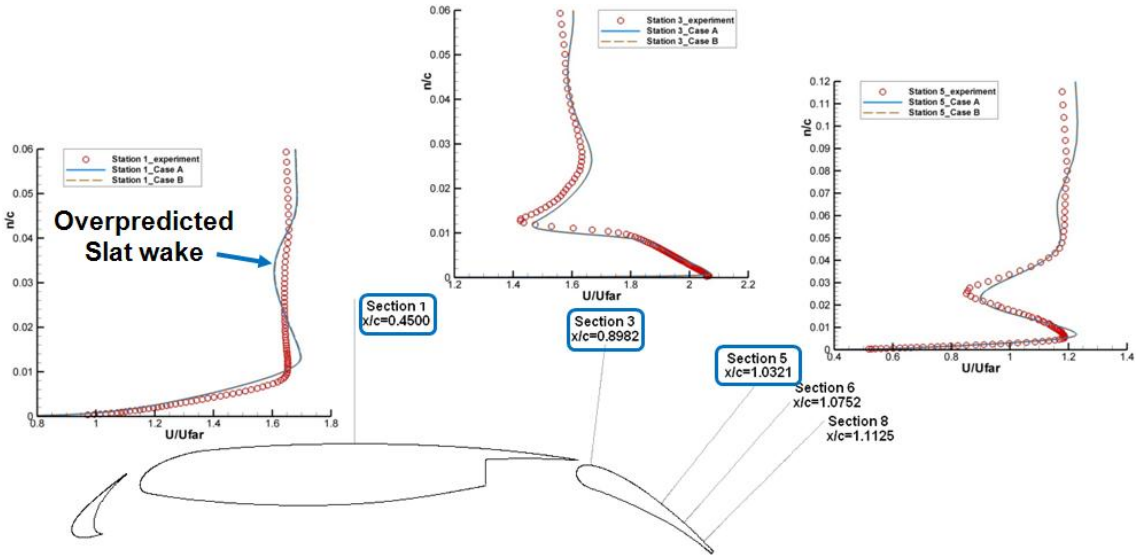

(a) Validation

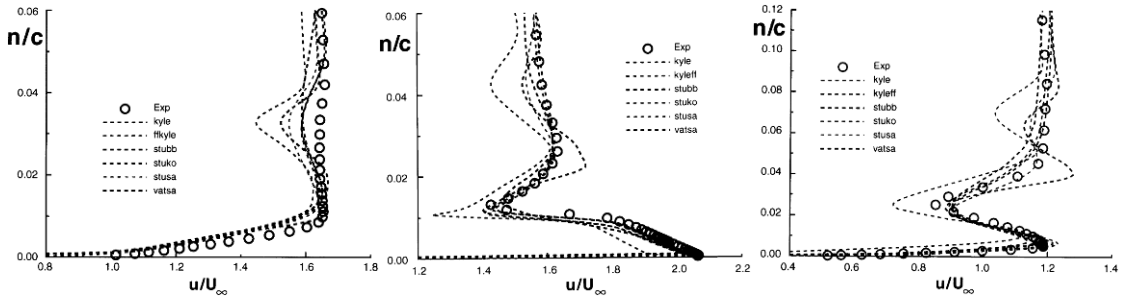

x/c=0.450 x/c=0.898 x/c=1.032

(b) Results from other research [24]

Figure 5-5 Comparison of velocity profile at different station

As discussed by other researchers, the slat wake was usually predicted too wide and deep. The overpredicted slat wake was also been found in both cases. Experimental data showed that the slat wake and boundary layer on the wing merged at station 1, but these phenomena were not captured by the simulations.

5.2.2 Influence of Reynolds number

As the larger far field extent did show advantages in drag prediction, simulations using a different Reynolds number were performed with *eff*=50c. Similar to the previous simulations, the residual of each computed variable was checked first. The convergence of the calculation was also determined by monitoring the lift and drag coefficients (see Fig. 5-6). The y^+ of each case was also checked and found to be acceptable (see Fig. 5-7).

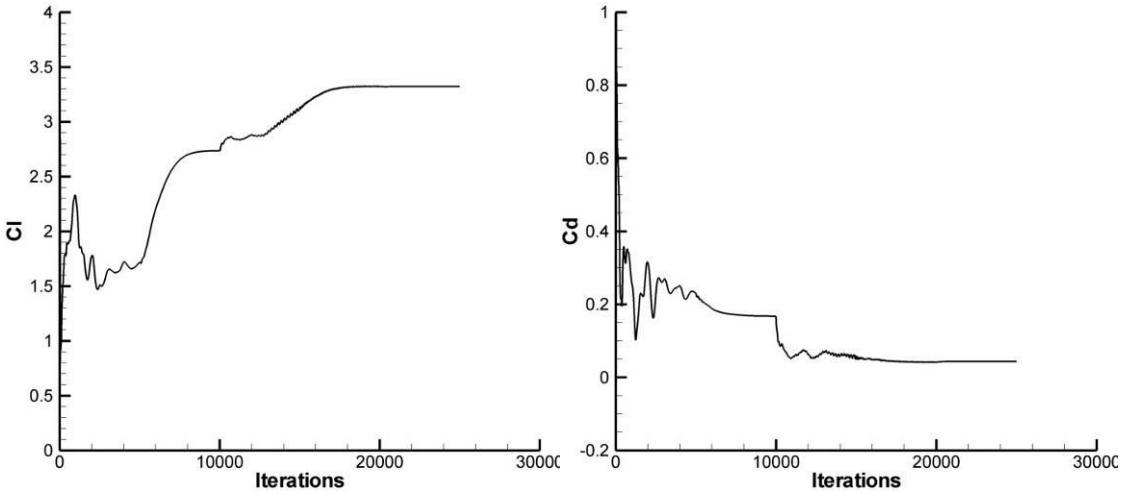

(a) Lift coefficient (b) Drag coefficient

Figure 5-6 Typical convergence histories (Case C)

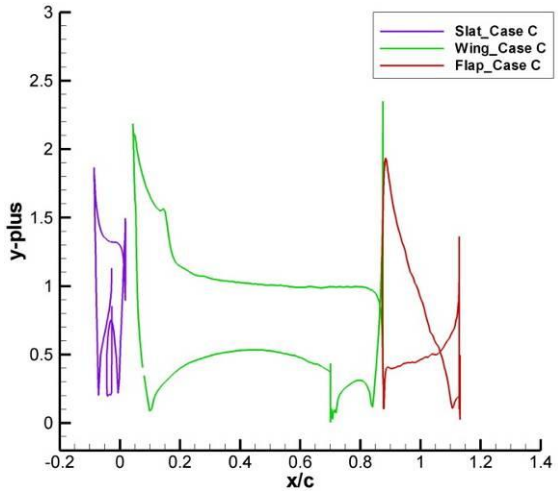

Figure 5-7 y^+ distribution of Case C

Table 5-4 Comparison between calculated coefficients and experiment

	Re=5×10^6		Re=9×10^6	
	Exp.	Case B	Exp.	Case C
C_L	3.0841	3.2754	3.1354	3.3205
$(C_L- C_{LExp})/ C_{LExp}$		+6%		+6%
C_D	0.0361	0.0472	0.0278	0.0431
$(C_D- C_{DExp})/ C_{DExp}$		+31%		+55%
C_M	-0.5701	-0.6133	-0.5872	-0.6220
$\|(C_M- C_{MExp})/ C_{MExp}\|$		+8%		+6%

Table 5-4 shows calculated force coefficients and relevant experimental results. Slightly better C_M results were obtained with higher Reynolds number simulation, whilst no major differences were found in lift prediction. The drag, however, was overpredicted by 55% in comparison with experiment.

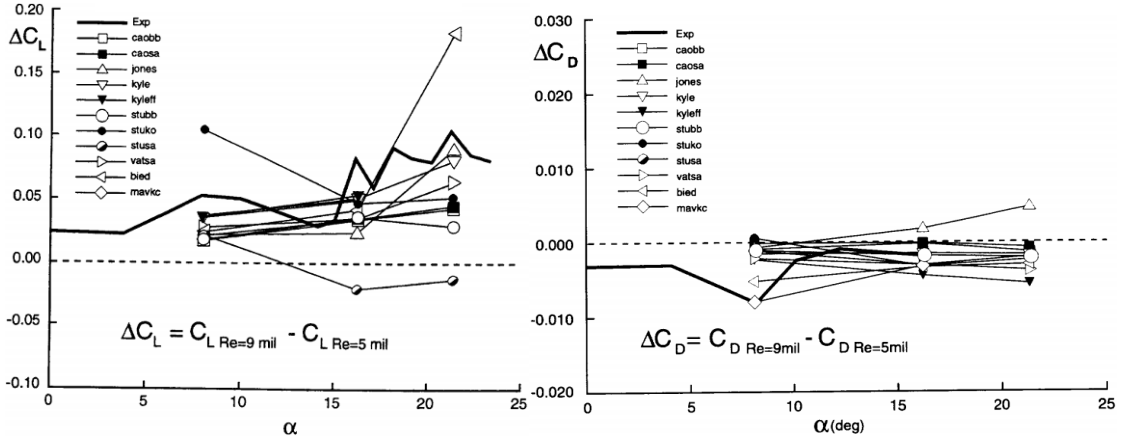

Figure 5-8 Lift and drag change due to increase in Reynolds number [18]

In Klausmeyer and Lin's report [28], the lift and drag changes caused by increase in Reynolds number were also studied. Generally speaking, computed lift change was lower than the experimental value and most of the predicted values of ΔC_L were between 0.04 and 0.06. The validation result, which was 0.045, also fell into the same region. For drag prediction, most of the computed results were smaller than the experimental value, too. As shown in Fig. 5-8, the

predicted drag decrease was found to be between 0 and 0.005. Despite the overpredicted drag value, the RANS code plus SA model had a similar result which was 0.004.

Using C_p distribution analysis, the overpredicted flow accelerations over the slat were also found and Case C produced a better result predicting the flow around the flap.

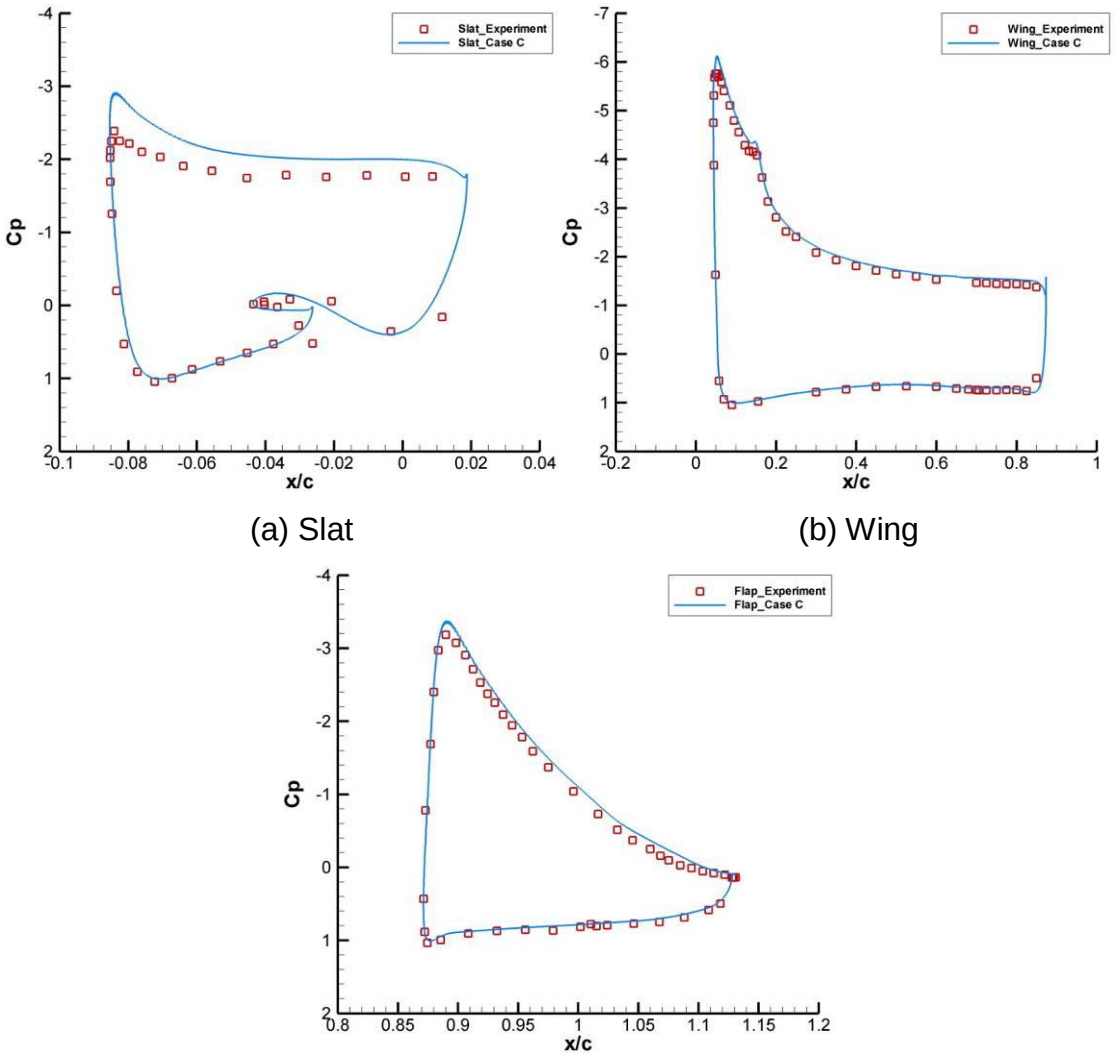

(a) Slat

(b) Wing

(c) Flap

Figure 5-9 Comparison of surface C_p distribution

The velocity profile also showed that case C had a good agreement with experiment (see Fig. 5-10), though the slat wake was still not captured precisely.

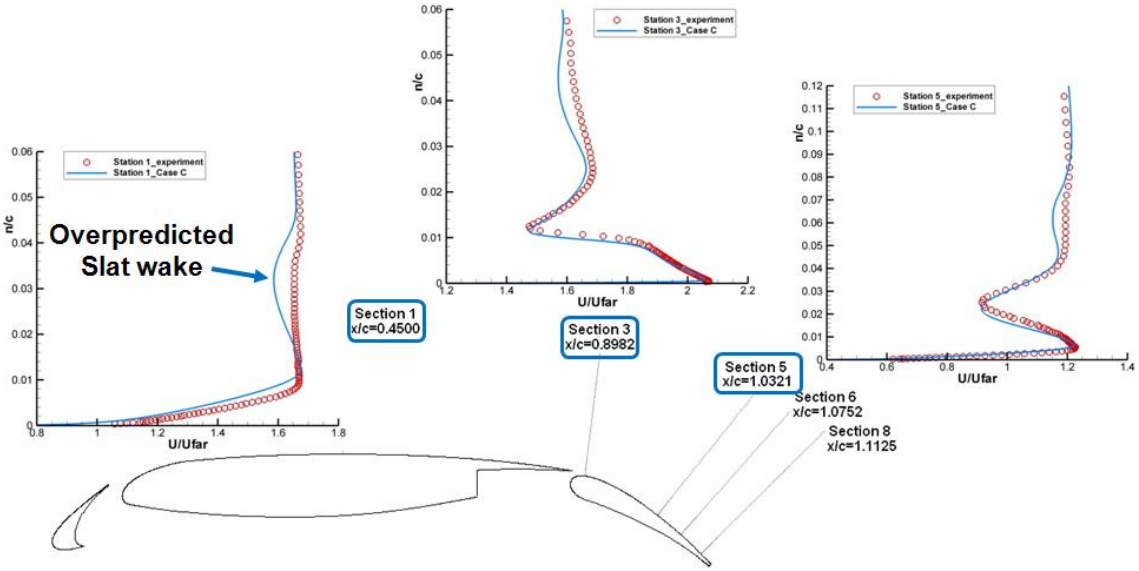

Figure 5-10 Velocity profile at different station

5.2.3 Summary

Three cases have been studied and results have been compared with experimental values and others computed data. Generally speaking, the RANS code with SA turbulence model is able to predict flow around the multi-element airfoil. But the flow field around the slat cannot be precisely resolved and the force coefficients are often overpredicted. A grid with larger far field extent will benefit the drag prediction. Lift and momentum predictions were quite similar at different Reynolds numbers. However, the difference between predicted drag and that observed experimentally seemed to increase at higher Reynolds number.

6 Results and Discussion

Both lift and drag coefficients were monitored during the simulation in order to determine the convergence. The residuals of each calculated variables were also checked.

As mentioned above, the simulation consists of two phases and each could be clearly seen in Fig. 6-1.

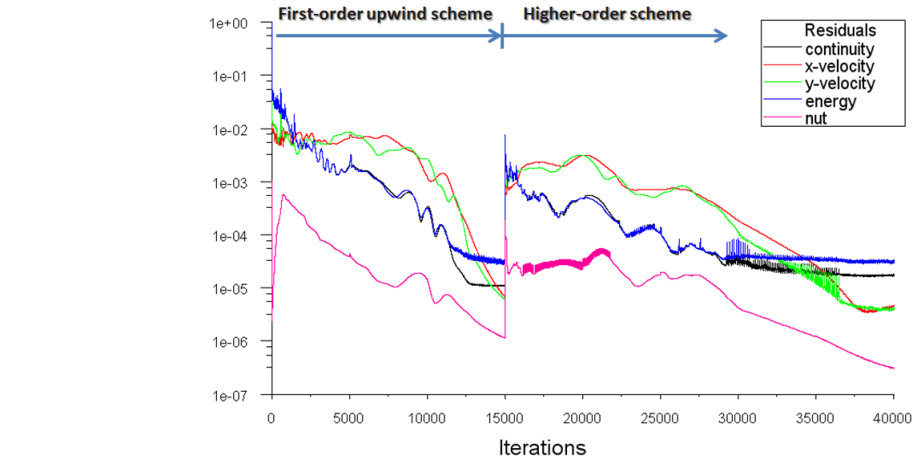

(a) Residuals

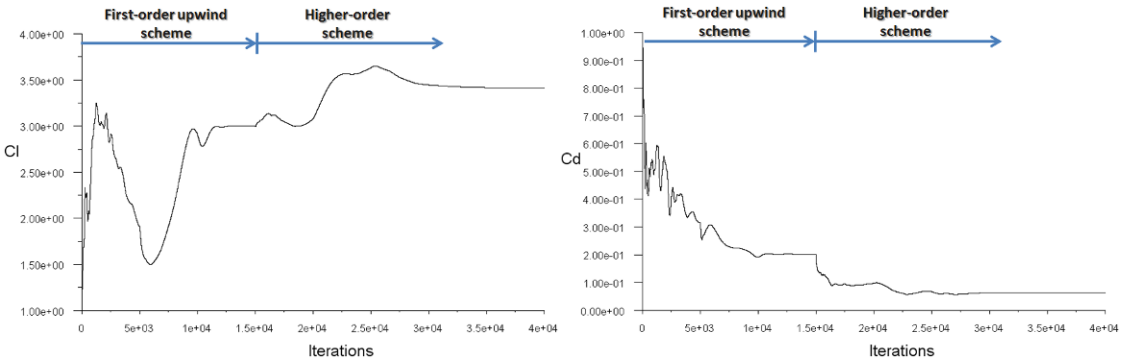

(b) C_L (c) C_D

Figure 6-1 Typical convergence histories (Case IV, ZB, α=12°)

As the Spalart-Allmaras one-equation turbulence model and the chosen near-wall treatment are dependent on a fine grid in the near-wall region, it is necessary to check the y^+ distribution when the calculation is finished. The y^+ values should be less than 4 while a value of y^+=1 would be the most desirable.

Fig. 6-1 shows that the y^+ values in most regions are around 1. In some regions, such as the leading edge of the airfoil, the y^+ values have exceeded 2, but none of them are larger than 3. These distributions illustrate that the near-wall grids are sufficient and that the viscous-affected regions have been properly resolved

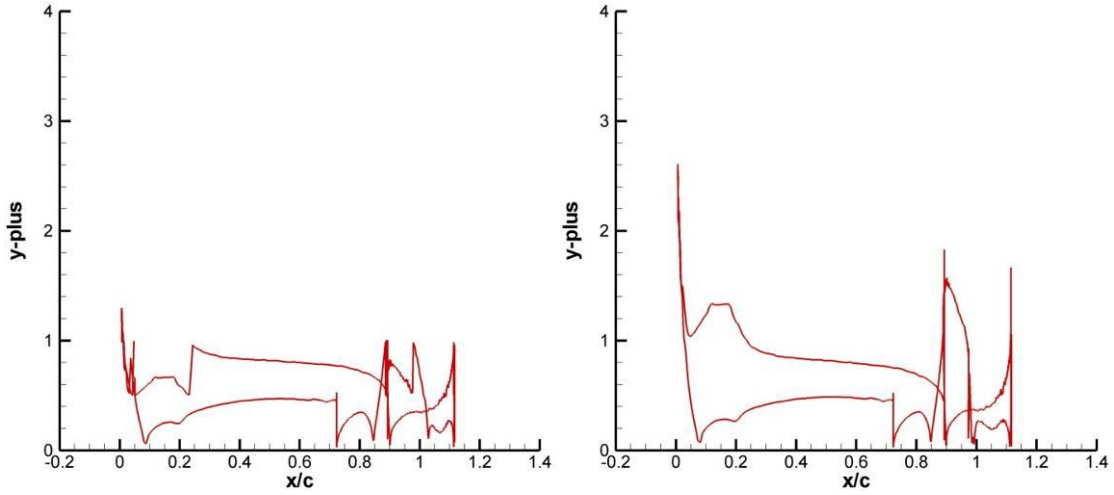

(a) Case II (b) Case III (ZB)

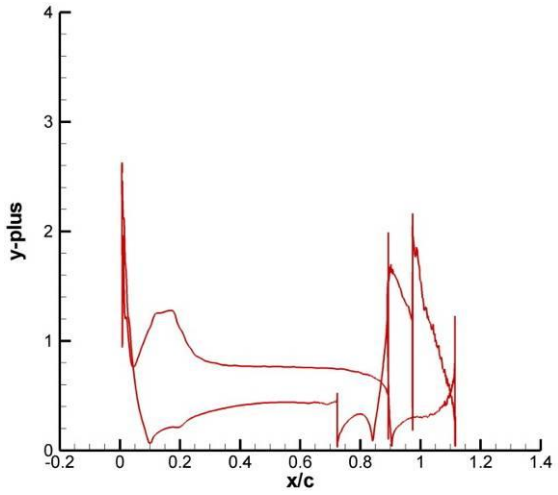

(c) Case III (HBR)

Figure 6-2 Typical y^+ distribution of study cases

6.1 Effects of camber change

To develop an understanding of camber related stall over the flap, two baseline cases, Case I and Case II, were compared first. Predicted force coefficients are shown in table 6-1. It can be clearly seen that the lift coefficients are almost the same for both cases; even the Case II has a higher camber. On the other hand,

the drag of Case II is almost 30% higher than Case I when the angle of attack is 4°. Difference of the drag narrowed along with the increase of airfoil's incidence. However, the drag of Case II is still 18% higher than Case I at α=12°. Hence, the lift-to-drag ratio for Case II is greatly affected.

Table 6-1 Predicted force coefficients of Case I and Case II

Case I				
α	C_L	C_D	L/D	C_M
4°	2.6146	0.0375	69.72	-0.6259
8°	3.0218	0.0453	66.71	-0.6071
12°	3.5045	0.0551	63.60	-0.6065
Case II				
α	C_L	C_D	L/D	C_M
4°	2.6195	0.0487	53.79	-0.6248
8°	3.0249	0.0557	54.31	-0.6061
12°	3.4539	0.0649	53.22	-0.5918

At α=4° (see Fig. 6-3.a1 and b1), the separation was found at around 60%c_{flap} for Case I. For Case II, the separation occurred at 50%c_{flap}. Increasing the airfoil's incidence to 8° did not change the position where the separation occurred for both cases. But as the angle of attack reached 12° (see Fig. 6-3.a3 and b3), the flow velocity through the flap slot increased. For Case I, these increased momentums were quite effective and delayed the separation to near 70%c_{flap}. But for Case II, the increased flow velocity did little to the flap separation and the separation was found at around 55%c_{flap}. So, it is obvious that the high-camber flap will not enhance the airfoil's performance at high deflection angle as the separation happens earlier on the flap upper-surface. The larger area of separation will induce larger drag which prevents the high-camber flap achieving its lift-enhancing benefits.

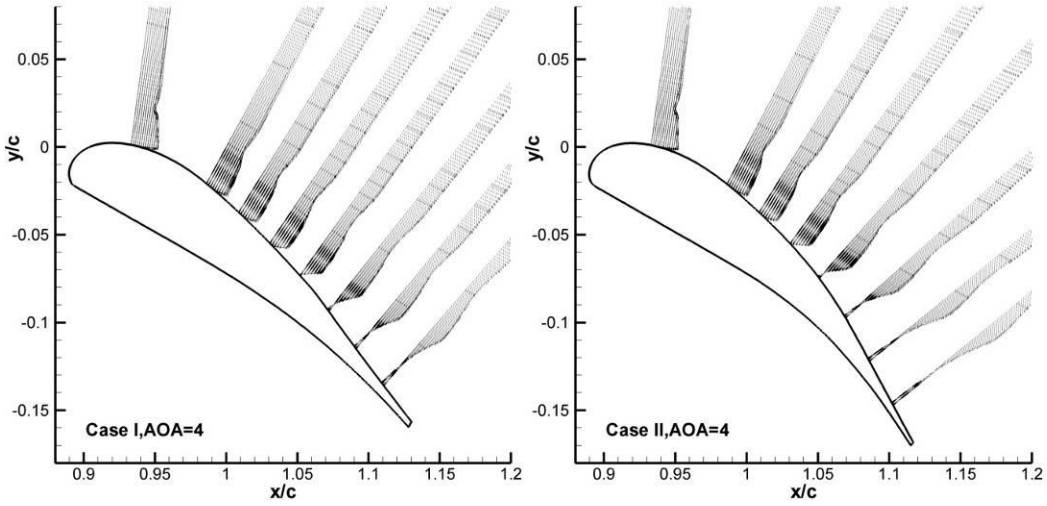

(a1) Case I (α=4°) (b1) Case II (α=4°)

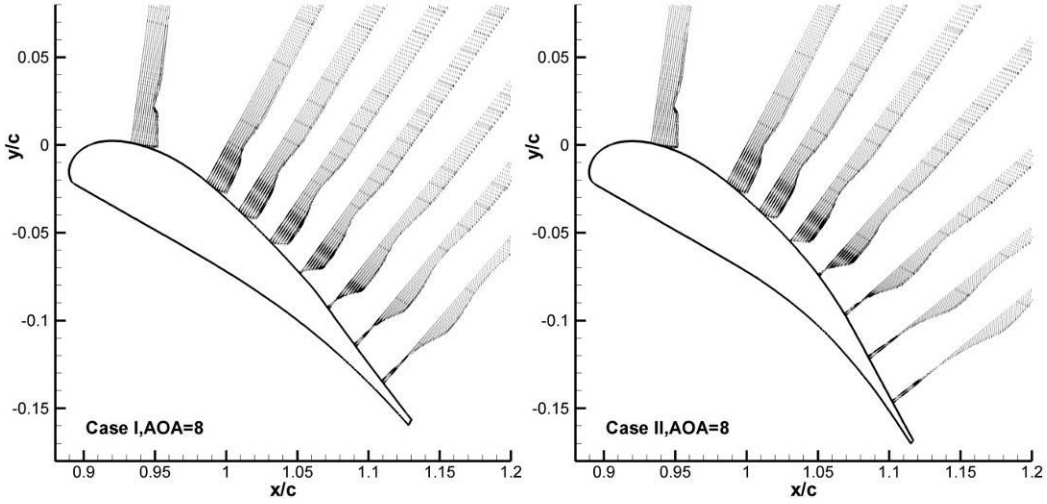

(a2) Case I (α=8°) (b2) Case II (α=8°)

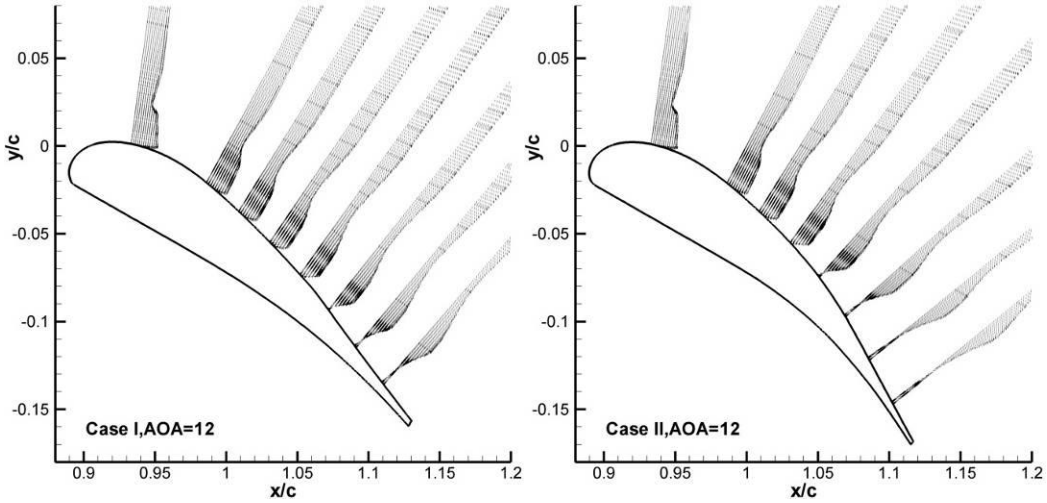

(a3) Case I (α=12°) (b3) Case II (α=12°)

Figure 6-3 Comparison of velocity profile at different positions

As no slat or slot had been applied at the leading edge, the flow over the leading edge of the airfoil had large curvature, especially at higher angle of attack. As shown in Fig. 6-4.c, flow velocity exceeded Mach 1 at the airfoil's leading edge. This caused large pressure recovery loss in the main element wake flow and increased the likelihood of breakdown. The wake flow of the main element became wider as the incidence increased (see Fig. 6-3). At α=12°, the wake flow broke up over the flap for both cases (see Fig. 6-5). These phenomena were not observed at α=4° and α=8°, as the flow near the leading edge of the airfoil remained subsonic.

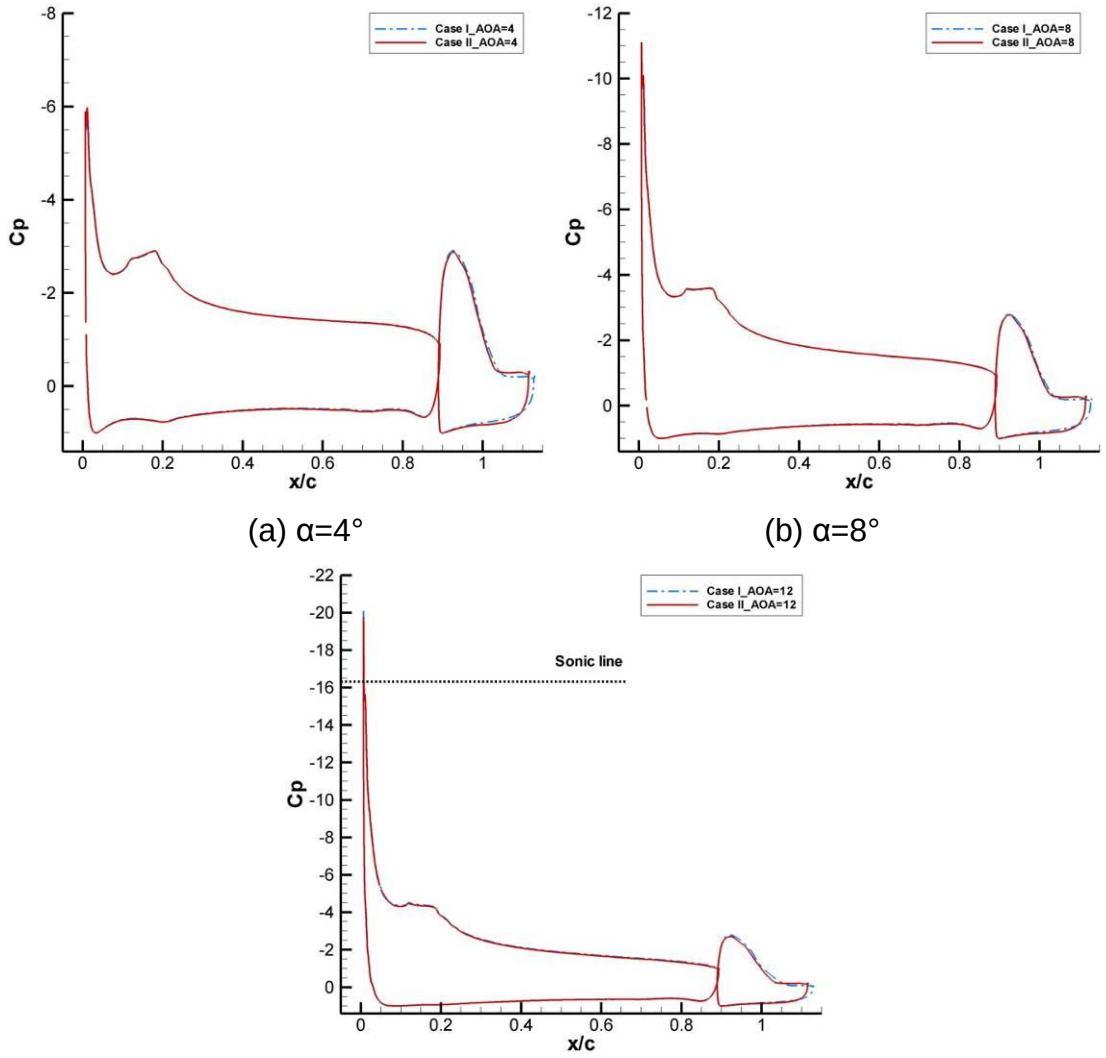

(a) α=4°

(b) α=8°

(c) α=12°

Figure 6-4 Comparison of C_p distribution

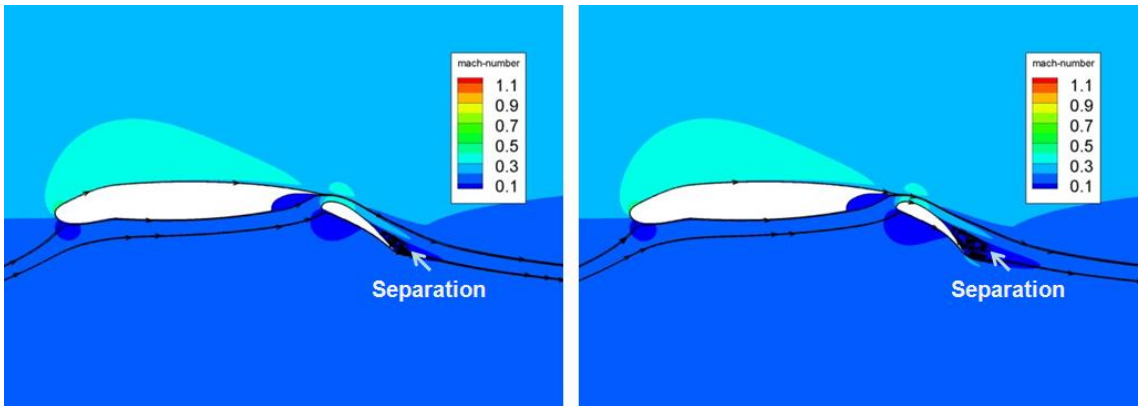

(a1) Case I (α=4°) (b1) Case II (α=4°)

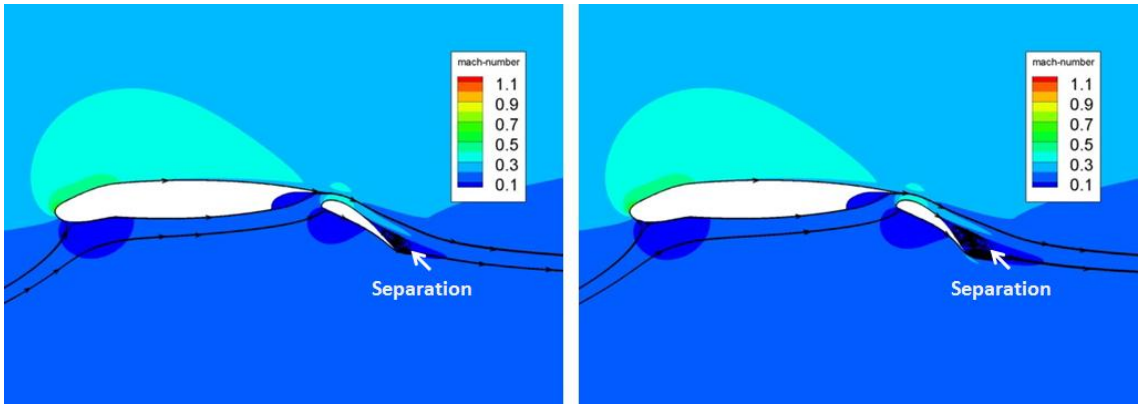

(a2) Case I (α=8°) (b2) Case II (α=8°)

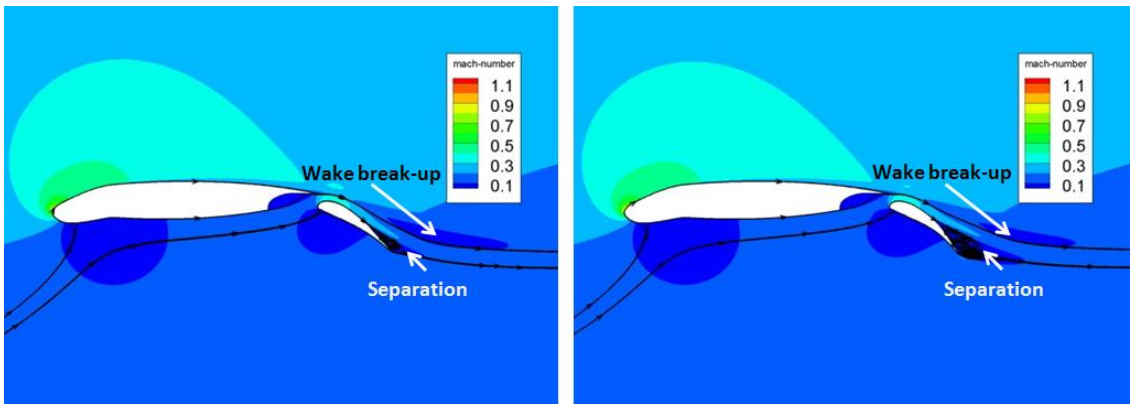

(a3) Case I (α=12°) (b3) Case II (α=12°)

Figure 6-5 Compare of streamlines and contour of Mach number

As discussed, Case I had a smaller separation region on the flap, but a larger area of wake flow of the main wing was found over the flap at α=12°. This explained why the C_D difference between Case I and Case II decreased as the incidence increased, and also indicated that the blowing might not further benefit the baseline airfoil as the main wing wake flow gradually became the

dominant factor of drag and it was beyond the control capability of blowing on the upper-surface of flap. In order to minimize the effect of the breakdown of main element wake, all simulations in this study have been performed with α ≤12°. To further improve the performance of the baseline airfoil, flow control devices, e.g. the lift-enhancing tabs placed in the cove region at the trailing edge of the main element [4, 24, and 35], could be used. But these are beyond the scope of this thesis and will not be discussed.

6.2 Effects of blowing

Like the baseline cases, two blowing cases have been simulated at three different incidences. Different blowing momentums have been analyzed, too.

6.2.1 Tangential blowing (Case III)

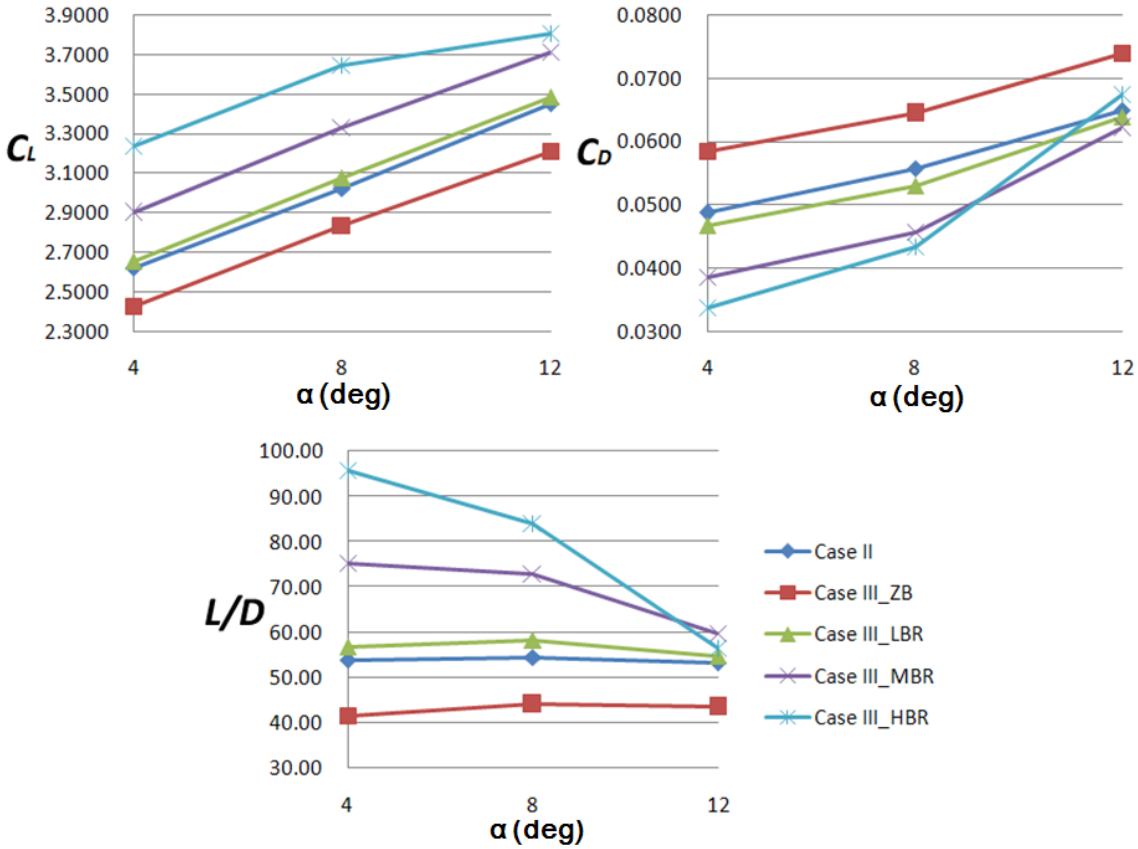

Figure 6-6 Effects of steady blowing (Case III)

As clearly shown in Fig. 6-6, larger C_μ led to better lift performance, especially at low angles-of-attack. This was also true when considering the drag and life-to-drag ratio at lower incidence.

High-blowing rate (HBR) – Quantitative results are listed in table 6-2. At α=4°, flow visualization results showed that the blowing delayed the separation from 50%c_{flap} to 90%c_{flap} (see Fig. 6-8.a) while a minor breakdown of the main element wake flow was found over the trailing edge of the flap (see Fig. 6-7.a). The comparison of pressure coefficient indicated that the blowing did not only minimize the separation on the flap, but also increased the flow velocity on the upper-surface of the main element (see Fig. 6-9). This was a result of the Coandă effect. As the upper-surface blowing eliminated the separation, the flow was bent downwards and accelerated. As a result, a 24% growth in C_L and a dramatic reduction of 30% in drag coefficient was achieved compared to Case II. The most encouraging result is the lift-to-drag ratio which was increased by 78%.

Similar results were observed when the simulation was performed at α=8°. The flap separation was not found even at 90%c_{flap}. Increased flow velocity was also observed on the main element upper-surface. But the flow velocity at the leading edge was quite close to Mach 1, and thus induced larger pressure recovery loss. The flow visualization results also illustrated that the bending of flow made the breakdown of the main element wake flow happened earlier. At this incidence, 20% of lift enhancement and 22% of drag reduction were achieved and led to a rise of nearly 55% in *L/D*.

When the airfoil's incidence reached 12°, the high C_μ increased the C_D rather than brought it down. The C_D increased by 55.5% at α=12° compared to that observed at α=8°. Consequently, only 6% lift-to-drag enhancement was found, even though the C_L was still 10% larger. As the flow became supersonic at the leading edge, a significant breakdown of the main wing wake flow was found over the flap (see also Fig. 6-7), which caused the drag to soar despite the elimination of separation on the flap. As the main wing began to stall, the upper-surface blowing on the flap could not further benefit the performance of the

airfoil. In addition, prediction results also showed a higher blowing momentum was necessary in order to eliminate the separation at low incidence.

Once the jet was introduced to the flow field, the mixing between the injected and incident flow could begin. Simulation results showed these flows were fully mixed at around 70%c_{flap} at α=4°and α=8°. The injected flow maintained its momentum until reaching 80% flap chord.

Table 6-2 Results of simulation (Case III, HBR)

α	C_μ	C_L	C_D	L/D	C_M
4°	0.0112	3.2382	0.0338	95.80	-0.8006
8°	0.0109	3.6442	0.0434	83.97	-0.7760
12°	0.0099	3.8082	0.0675	56.42	-0.6880

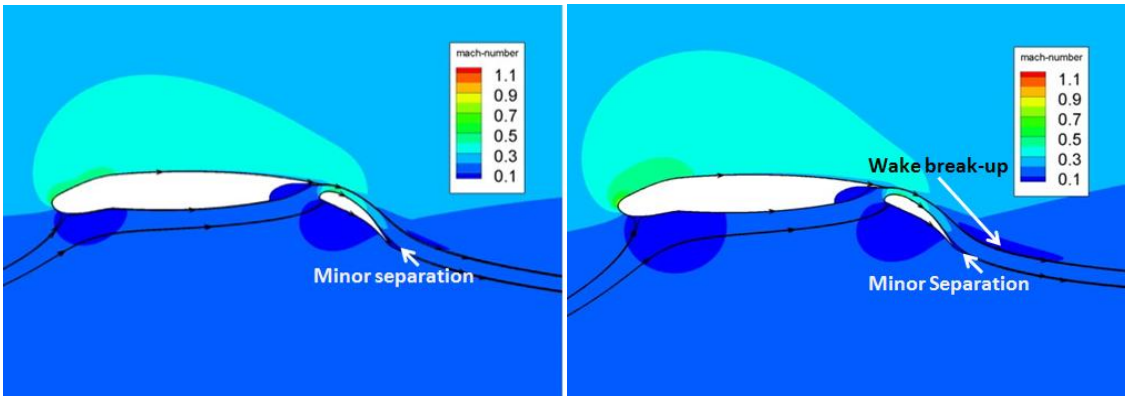

(a) α=4° (b) α=8°

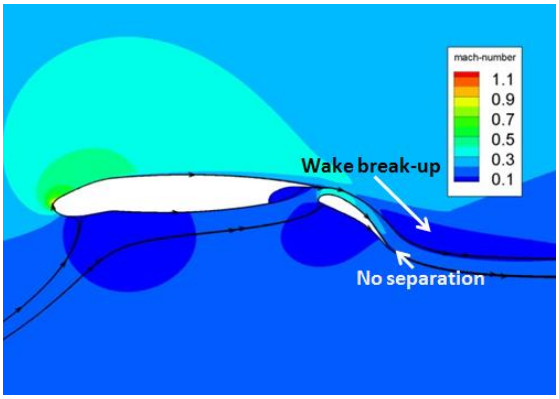

(c) α=12°

Figure 6-7 Streamline and contour of Mach number (Case III, HBR)

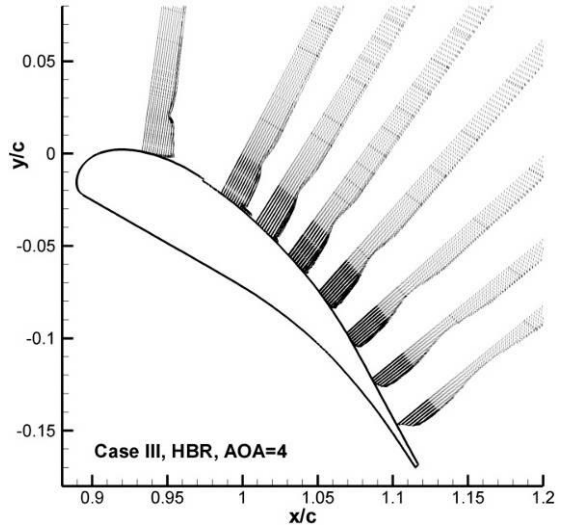

(a) α=4°

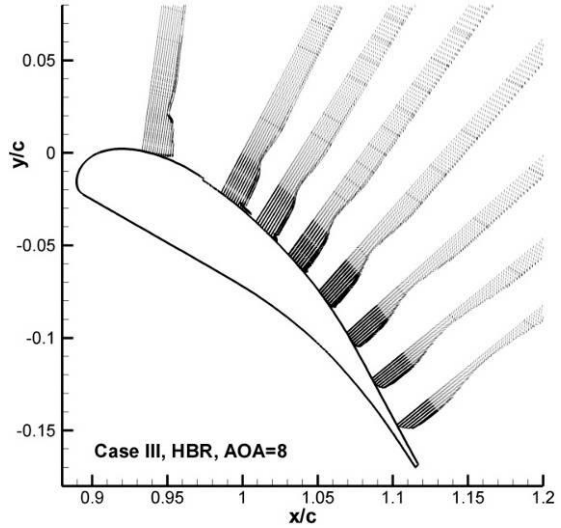

(b) α=8°

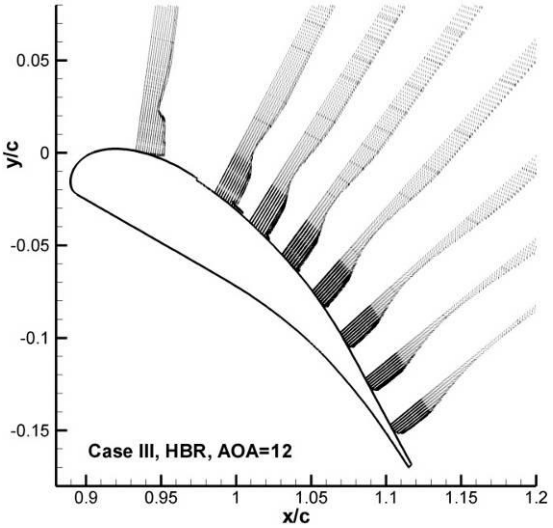

(c) α=12°

Figure 6-8 Velocity profile on the flap upper-surface (Case III, HBR)

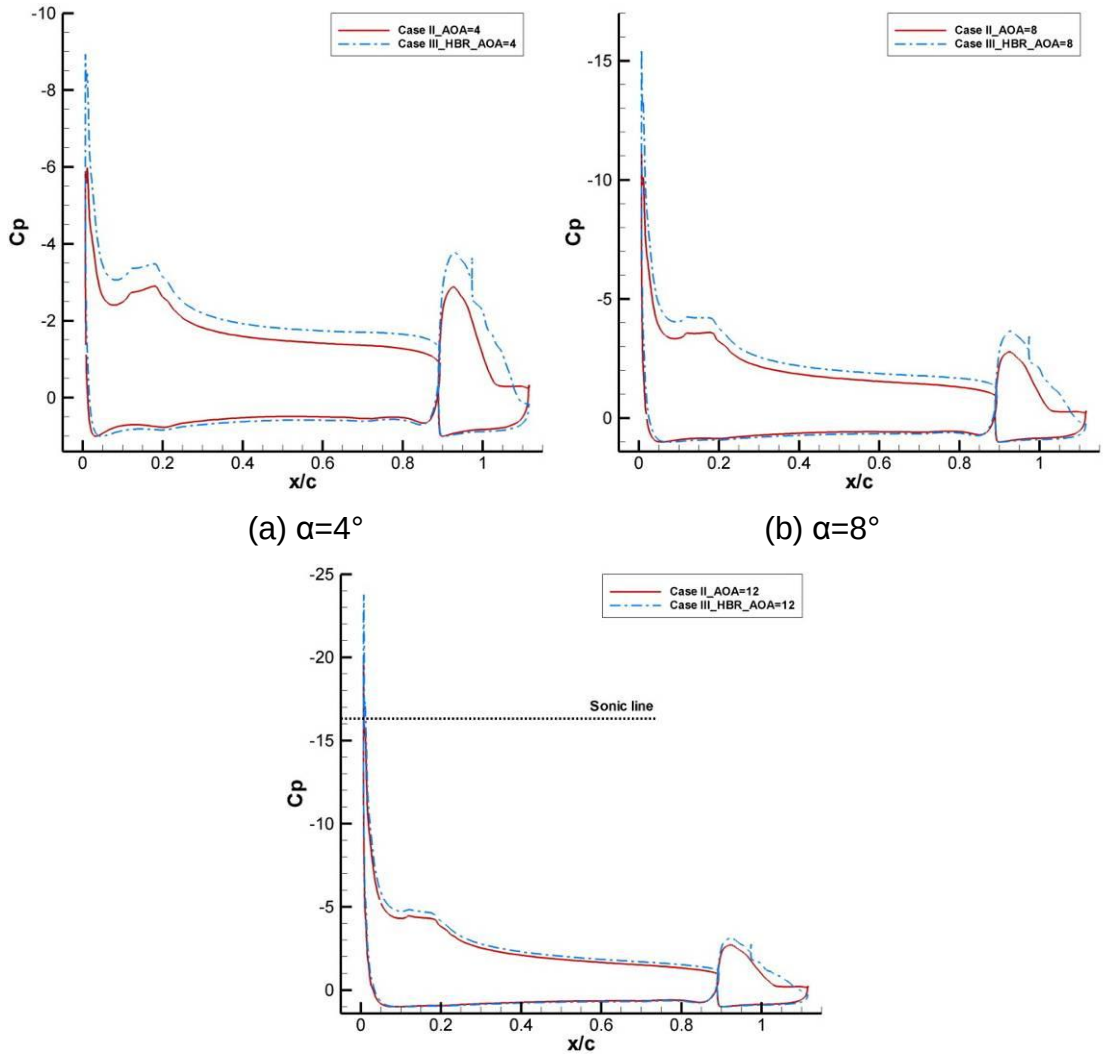

(a) α=4° (b) α=8°

(c) α=12°

Figure 6-9 Comparison of C_p distribution (Case II & III, HBR)

Medium-blowing rate (MBR) - Quantitative results are listed in table 6-3. Unlike the high-blowing case, the lift curve of the airfoil was still in its linear region when the medium rate blowing was applied. C_L rose steadily as the incidence increased. Approximately 10% improvement in C_L was achieved at both α=4° and α=8°. At α=12°, this figure dropped to 7.5%. The drag curve was found to be in a similar pattern as for the high-blowing case. Starting with a 21% reduction at α=4°, the C_D also jumped when the airfoil's incidence reached 12°. Though the C_D did not increase as much as it did under the high-blowing rate condition, only 4% drag reduction was achieved. A decrease of *L/D* was observed, too.

Table 6-3 Results of simulation (Case III, MBR)

α	C_μ	C_L	C_D	L/D	C_M
4°	0.0077	2.8979	0.0385	75.27	-0.7021
8°	0.0075	3.3283	0.0457	72.83	-0.6873
12°	0.0071	3.7136	0.0621	59.80	-0.6603

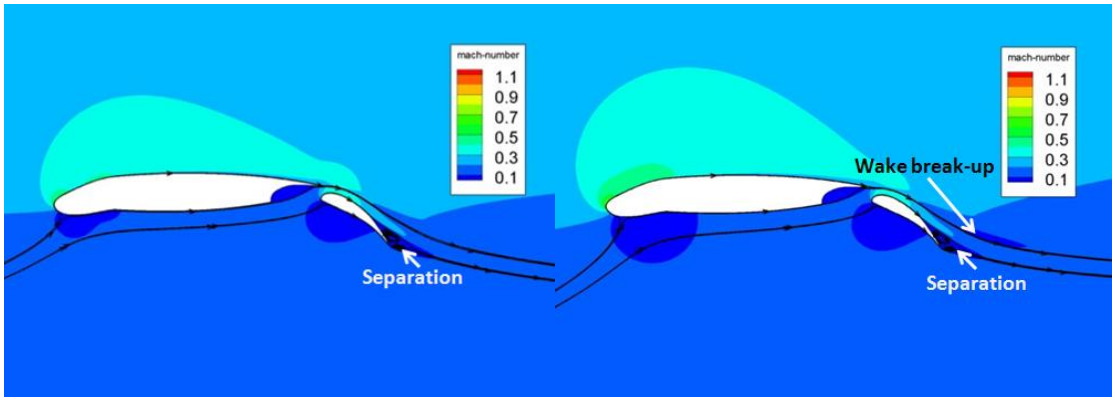

(a) α=4° (b) α=8°

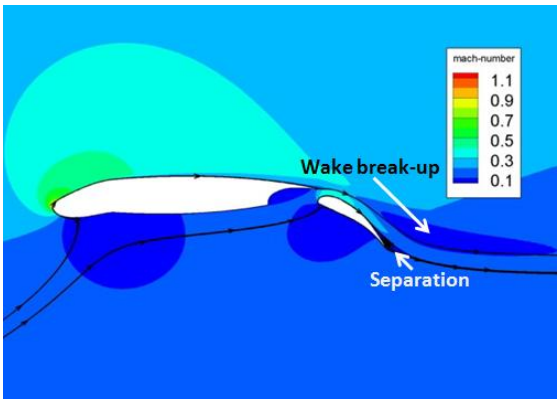

(c) α=12°

Figure 6-10 Streamline and contour of Mach number (Case III, MBR)

From analysis of the velocity profile of different incidences, the medium blowing could delay the separation on the flap upper-surface. Flow separated at near 70%c_{flap} for both α=4° and α=8° conditions. The area of the separation became smaller along with the increase of incidence (see Fig. 6-11). And the separation was observed at 80% c_{flap} at α=12°.

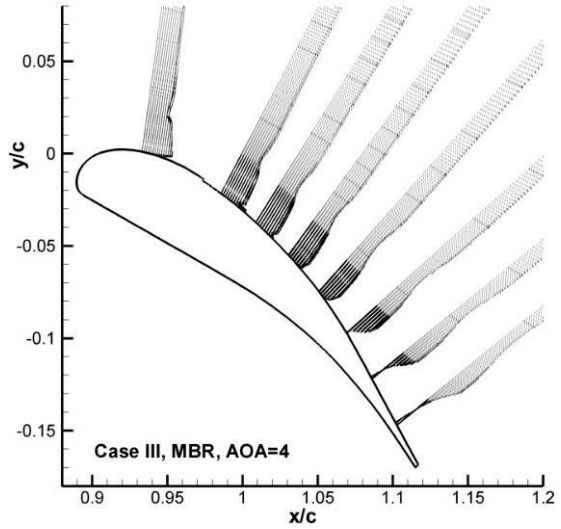

(a) α=4°

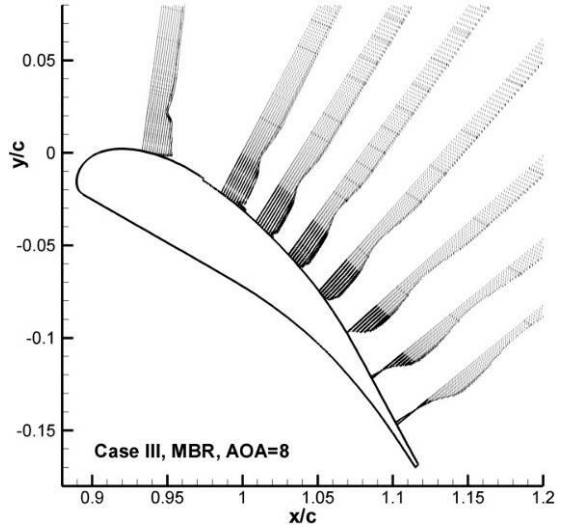

(b) α=8°

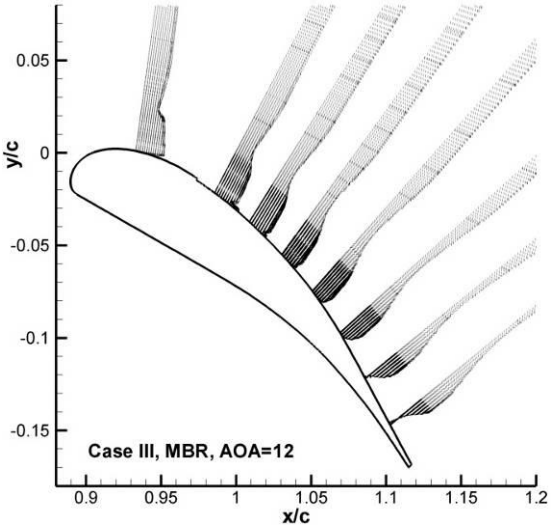

(c) α=12°

Figure 6-11 Velocity profile on the flap upper-surface (Case III, MBR)

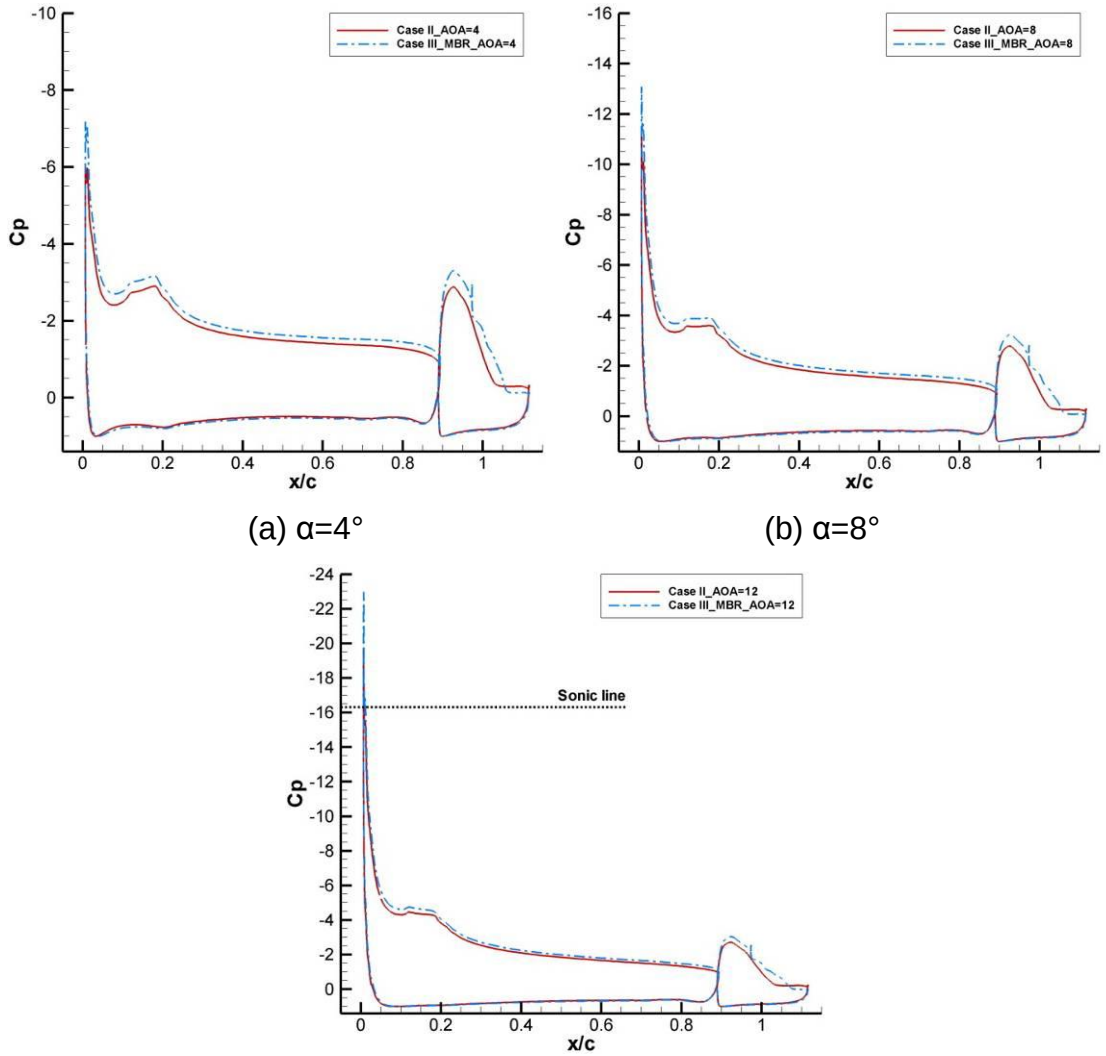

(a) α=4° (b) α=8°

(c) α=12°

Figure 6-12 Comparison of C_p distribution (Case II & III, MBR)

Increased flow velocity was also observed on the upper-surface of the main element. But the C_p curve experienced a downward shift along with the decreased sucking peak at the leading edge. However, the flow still became supersonic at the leading edge when the airfoil's incidence reached 12°. The wake of the main wing did not break at α=4°. Though its breakdown was found at both α=8° and α=12° (see also Fig. 6-10), the area of the wake was smaller than it was when the high-blowing-rate blowing was applied. Both the breakdown of the main wing wake and the separation on the flap contributed to the increase of drag for these conditions.

The injected flow and the boundary layer fully merged before 50%c_{flap} position. This indicated that it was the mixing between the injected and incident flow that prevented the blowing from maintaining the capability of separation control. Placing the slot further downstream (closer to the separation point) would minimize such an effect.

Low-blowing rate (LBR) – Quantitative results are listed in table 6-4. Though jets of both high-blowing and medium-blowing rate were quite effective in enhancing the lift and decreasing the drag, the low-blowing rate did not improve the airfoil's performance much at all three tested incidences. Lift of the airfoil was increased by less than 2% at each angle of attack. For drag reduction, the best result was obtained at α=8° where C_D was decreased by 5% and led to 7% increase in lift-to-drag ratio. Similar to the 8° incidence condition, the blowing induced 4% of drag reduction at α=4°. But for α=12° condition, this figure dropped to less than 2%.

The injected flow fully merged with the boundary layer before reaching 50% flap chord. Without enough momentum, the blowing had limited effect on separation. As shown in Fig. 6-13, the separation on the flap was found at 60%c_{flap}. Though the separation had been slightly delayed, C_p distribution on both the flap and the main element were almost the same (see Fig. 6-14).

Table 6-4 Results of simulation (Case III, LBR)

α	C_μ	C_L	C_D	L/D	C_M
4°	0.0050	2.6521	0.0467	56.79	-0.6335
8°	0.0048	3.0776	0.0529	58.18	-0.6197
12°	0.0045	3.4841	0.0638	54.61	-0.5996

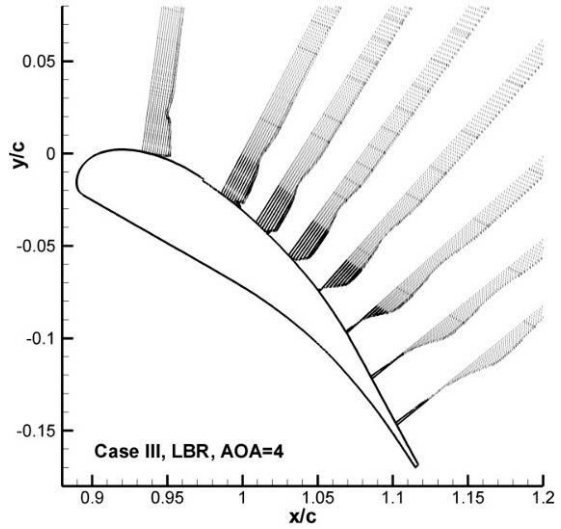

(a) α=4°

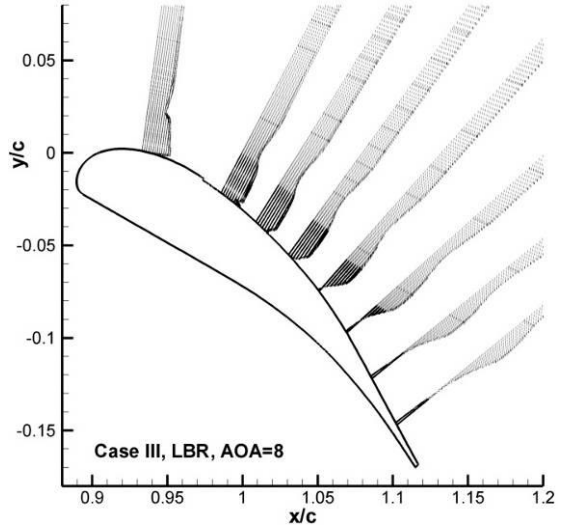

(b) α=8°

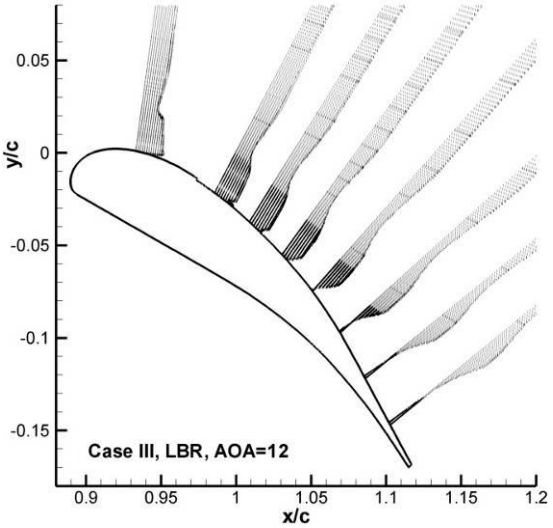

(c) α=12°

Figure 6-13 Velocity profile on the flap upper-surface (Case III, LBR)

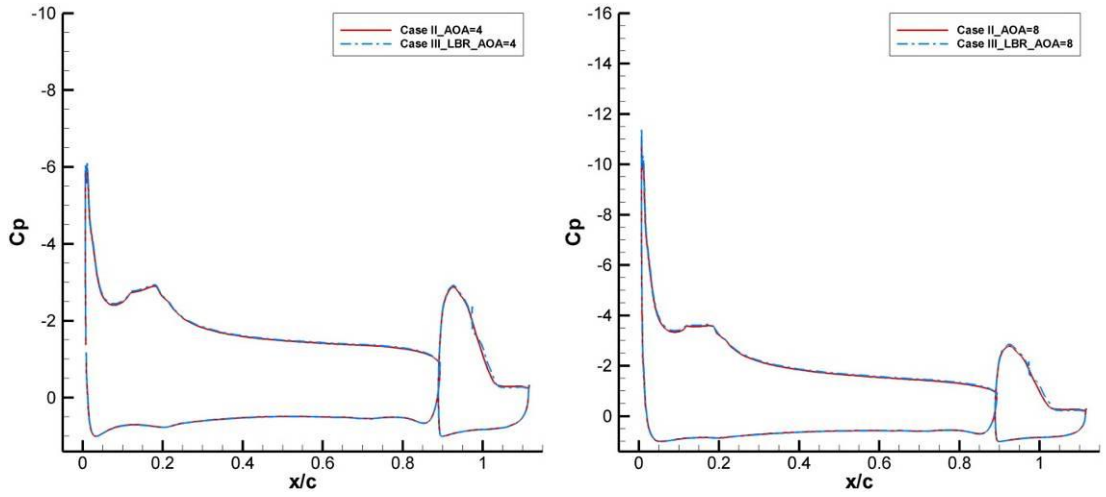

(a) α=4°

(b) α=8°

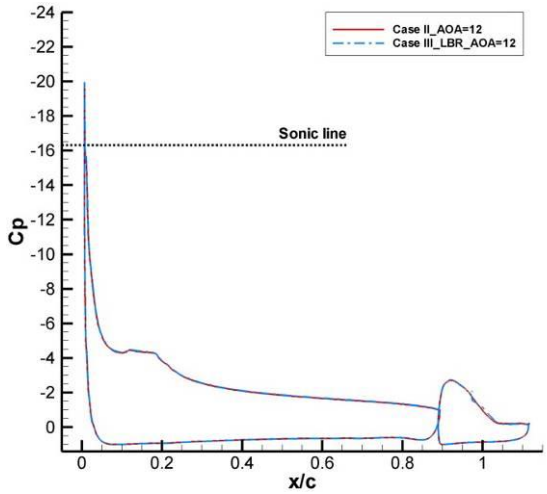

(c) α=12°

Figure 6-14 Comparison of C_p distribution (Case II & III, LBR)

Zero blowing (ZB) - Quantitative results are listed in table 6-5. Despite the huge improvement found, the predicted results of zero-blowing showed that the existence of the blowing slot and the partly modified airfoil profile introduced approximately 8% of lift loss and more than 10% drag penalty once the blowing system was off. As illustrated in Fig. 6-15, the blowing slot and the flap upper surface formed a backward facing step-like profile. The boundary layer separated at the sharp corner of the slot and then reattached on the upper-surface. As the airfoil profile became steeper downstream, separation occurred on the flap at near 40%c_{flap} position (see Fig. 6-16) where no sign of separation was found at the same position for Case II.

The blowing slot did not only affect the separation on the flap, but also induced larger pressure recovery loss of the main element wake, as this wake flow had been forced to bend upward and decelerate over the flap. Downward shifting of the *Cp* curve was seen on the upper-surface of both the flap and the main element (see Fig. 6-17).

So, it is clear that this kind of slot design will trigger the separation and cause performance deterioration of the airfoil. For Case III, the low-blowing rate is needed to remove these negative effects.

Table 6-5 Results of simulation (Case III, ZB)

α	C_μ	C_L	C_D	L/D	C_M
4°	0.0000	2.4236	0.0584	41.50	-0.5725
8°	0.0000	2.8351	0.0644	44.02	-0.5573
12°	0.0000	3.2100	0.0739	43.44	-0.5318

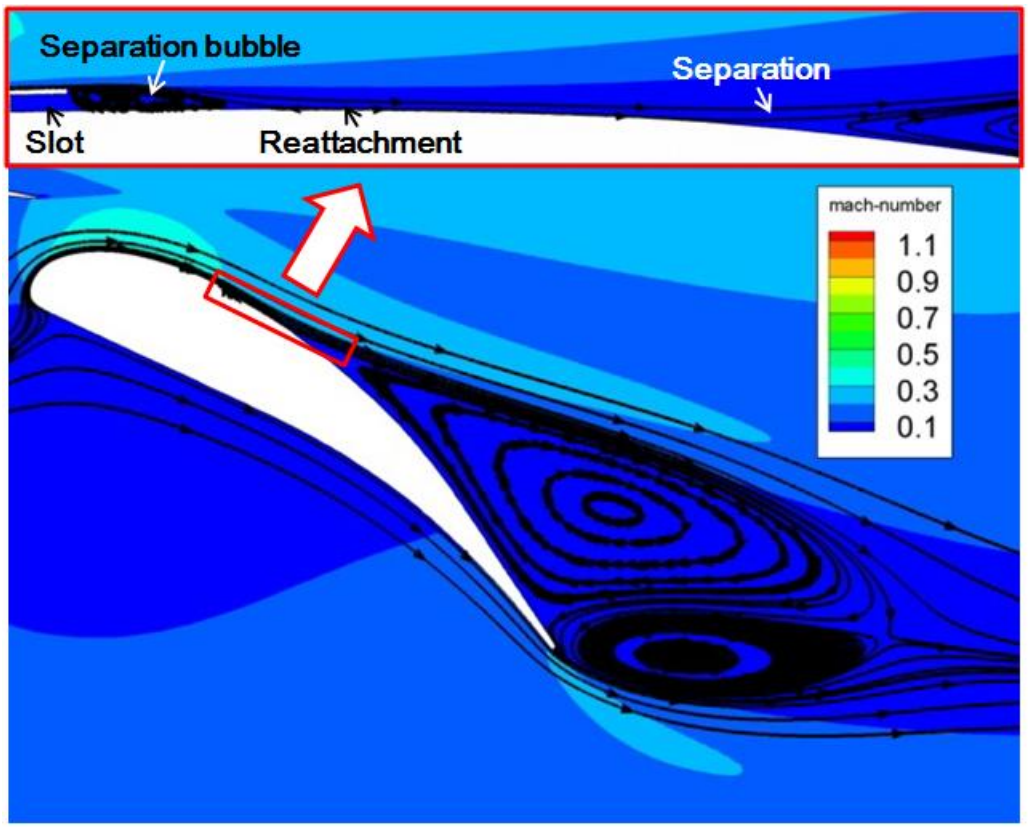

Figure 6-15 Flow behaviour near the blowing slot (Case III, *ZB*, α=12°)

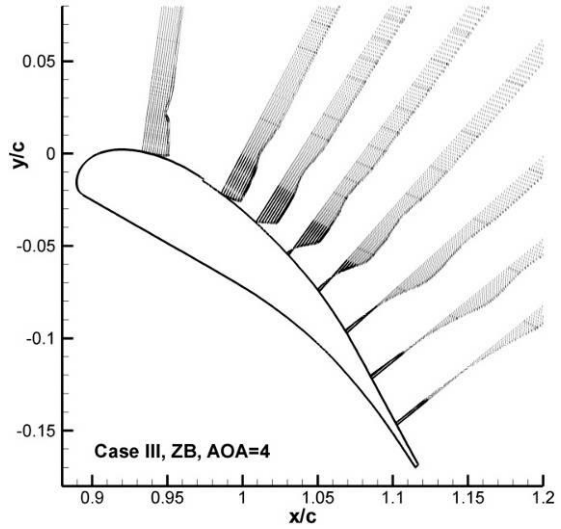

(a) α=4°

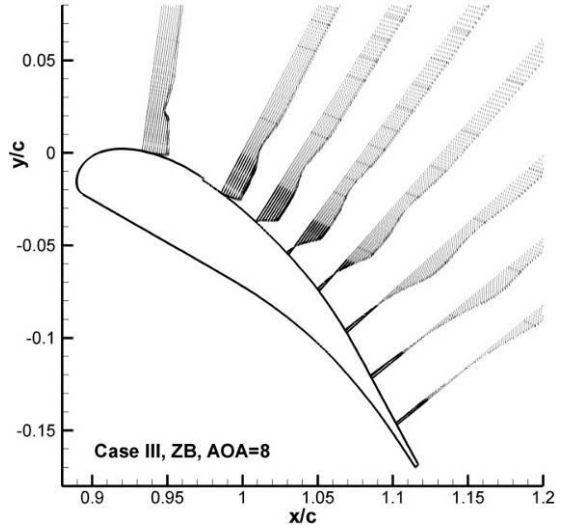

(b) α=8°

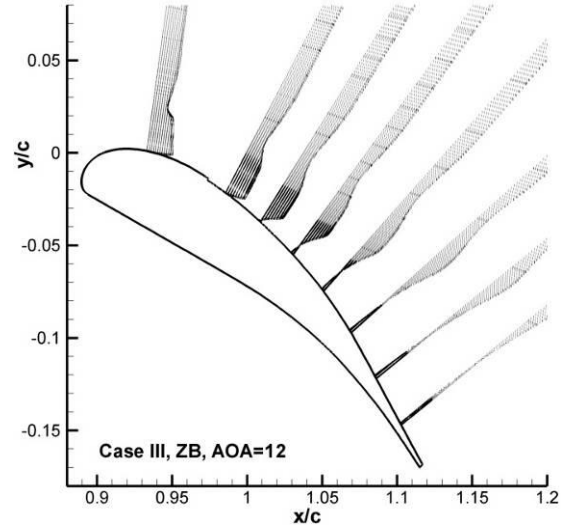

(c) α=12°

Figure 6-16 Velocity profile on the flap upper-surface (Case III, ZB)

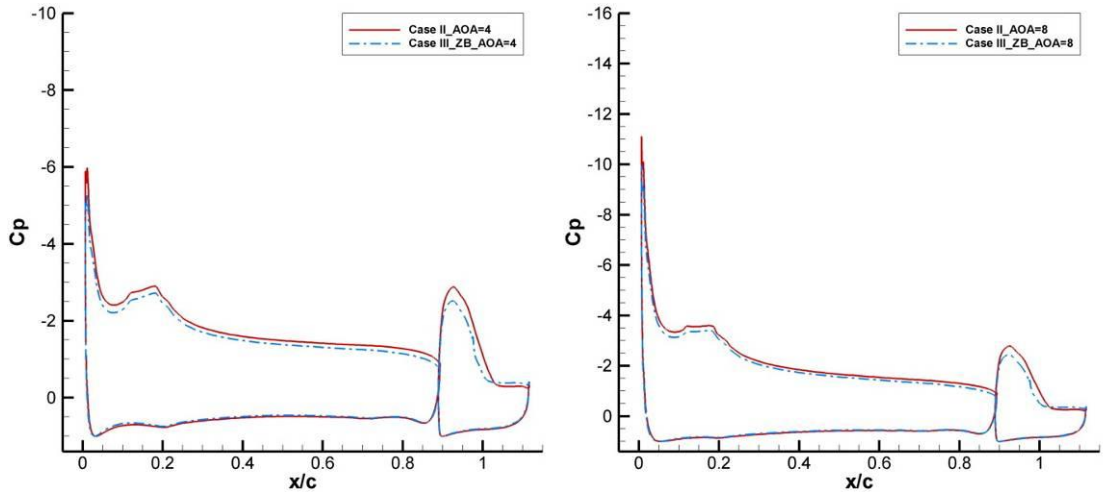

(a) α=4°

(b) α=8°

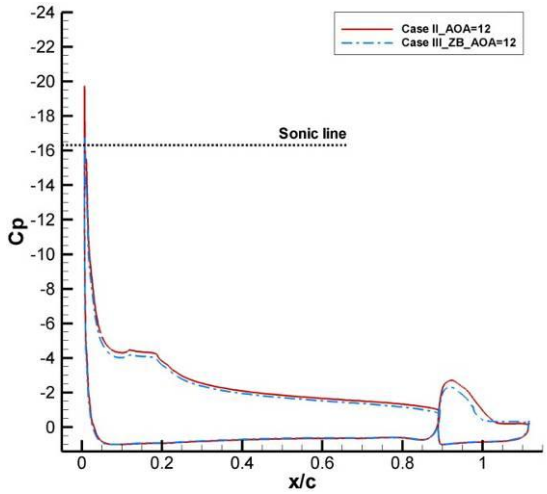

(c) α=12°

Figure 6-17 Comparison of C_p distribution (Case II & III, ZB)

6.2.2 Non-tangential blowing (Case IV)

As previously discussed, the upper-surface blowing had been shown to be effective against the separation on the flap, if sufficient blowing rate was provided. But the existence of the slot had a huge impact on drag once the system was off, and the modified airfoil profile was believed to be the major contributor to drag penalty. In the hope of solving this, non-tangential blowing had been developed and tested.

Similar to the results of Case III, the lift curve of Case IV experienced upward shifts with the injected momentum from the upper-surface blowing (see Fig. 6-18). Drag decreased simultaneously except at 12° angle-of-attack. For low incidence conditions, the larger the blowing momentum applied, the better the enhancement while could be obtained.

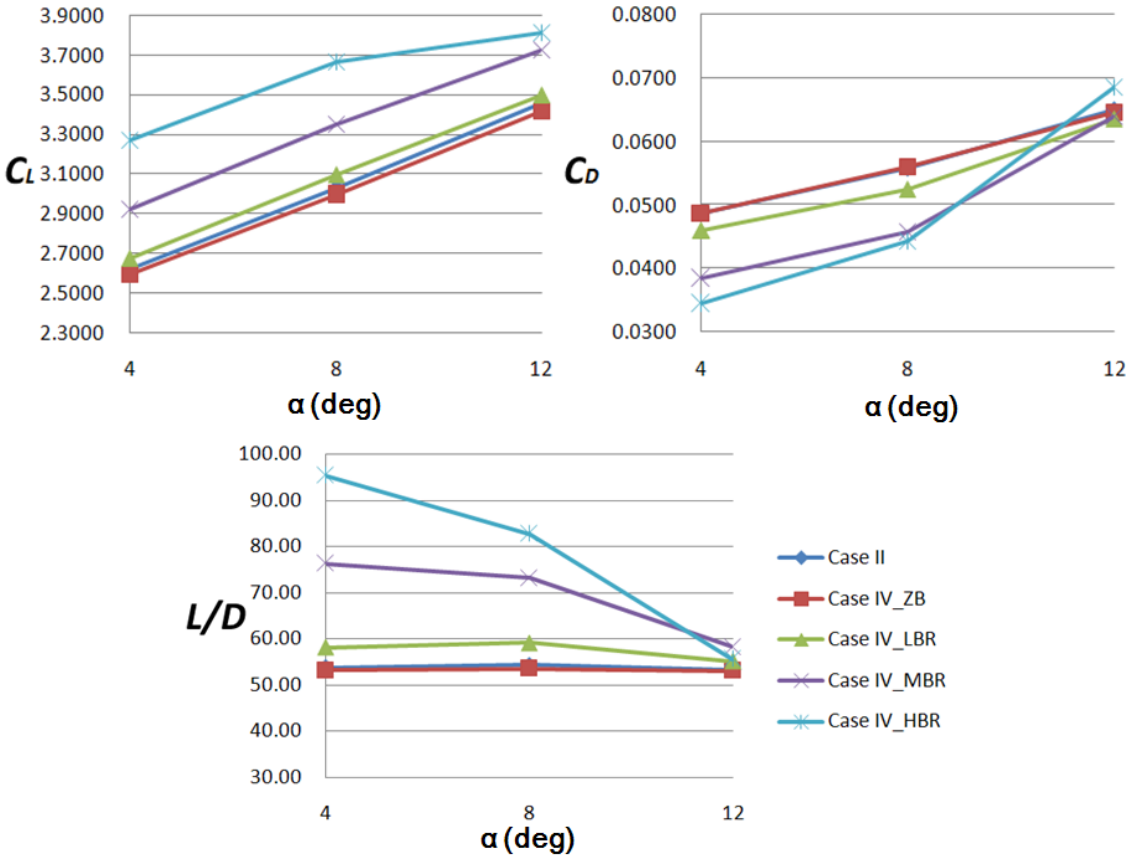

Figure 6-18 Effects of steady blowing (Case IV)

Zero blowing (ZB) – Quantitative results are listed in table 6-6. There was no significant difference between Case II and Case IV in computed force coefficients. The C_D was almost the same while the lift of Case IV decreased by 1%.

As the airfoil profile had barely been changed, the boundary-layer passed the blowing slot smoothly and stayed attached downstream (see Fig. 6-19). Velocity profiles (see Fig. 6-20) also showed good agreement between Case II and Case IV. Additionally, separation was found at the 50%c_{flap} position which was exactly the same as Case II at all three tested incidences. C_p distribution of the

main wing and flap was compared in Fig. 6-21. The downward shifting of C_p curve was not observed in this case. This showed that the drag penalty found in Case III was avoided.

Table 6-6 Results of simulation (Case IV, ZB)

α	C_μ	C_L	C_D	L/D	C_M
4°	0.0000	2.5902	0.0487	53.19	-0.6169
8°	0.0000	2.9909	0.0559	53.50	-0.5972
12°	0.0000	3.4187	0.0645	53.00	-0.5828

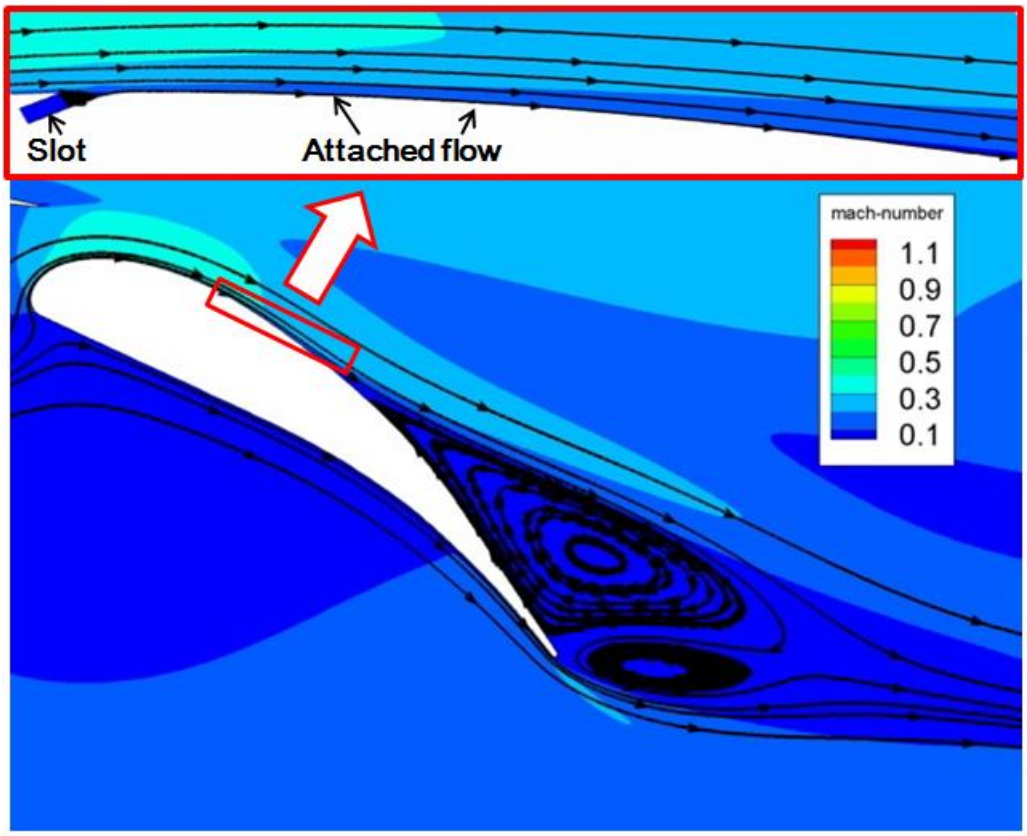

Figure 6-19 Flow behaviour near the blowing slot (Case IV, *ZB*)

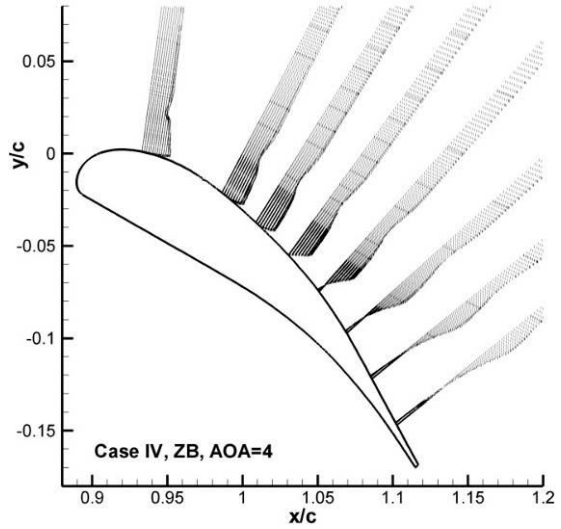

(a) α=4°

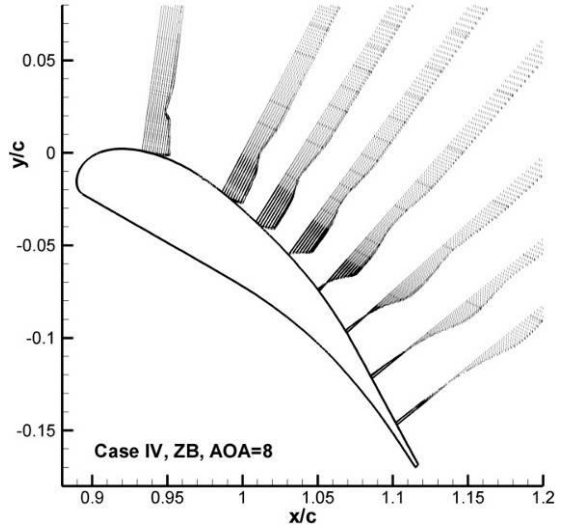

(b) α=8°

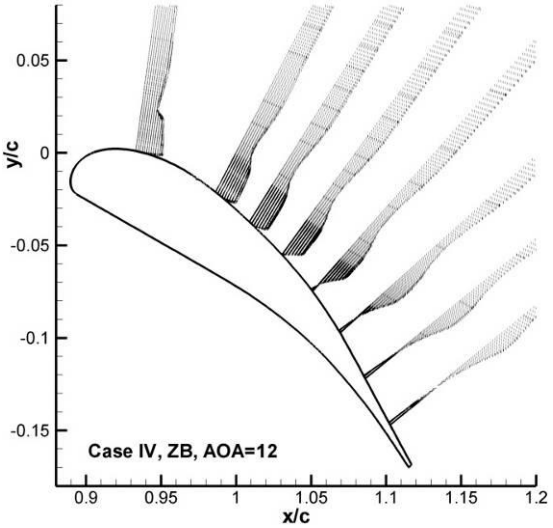

(c) α=12°

Figure 6-20 Velocity profile on the flap upper-surface (Case IV, ZB)

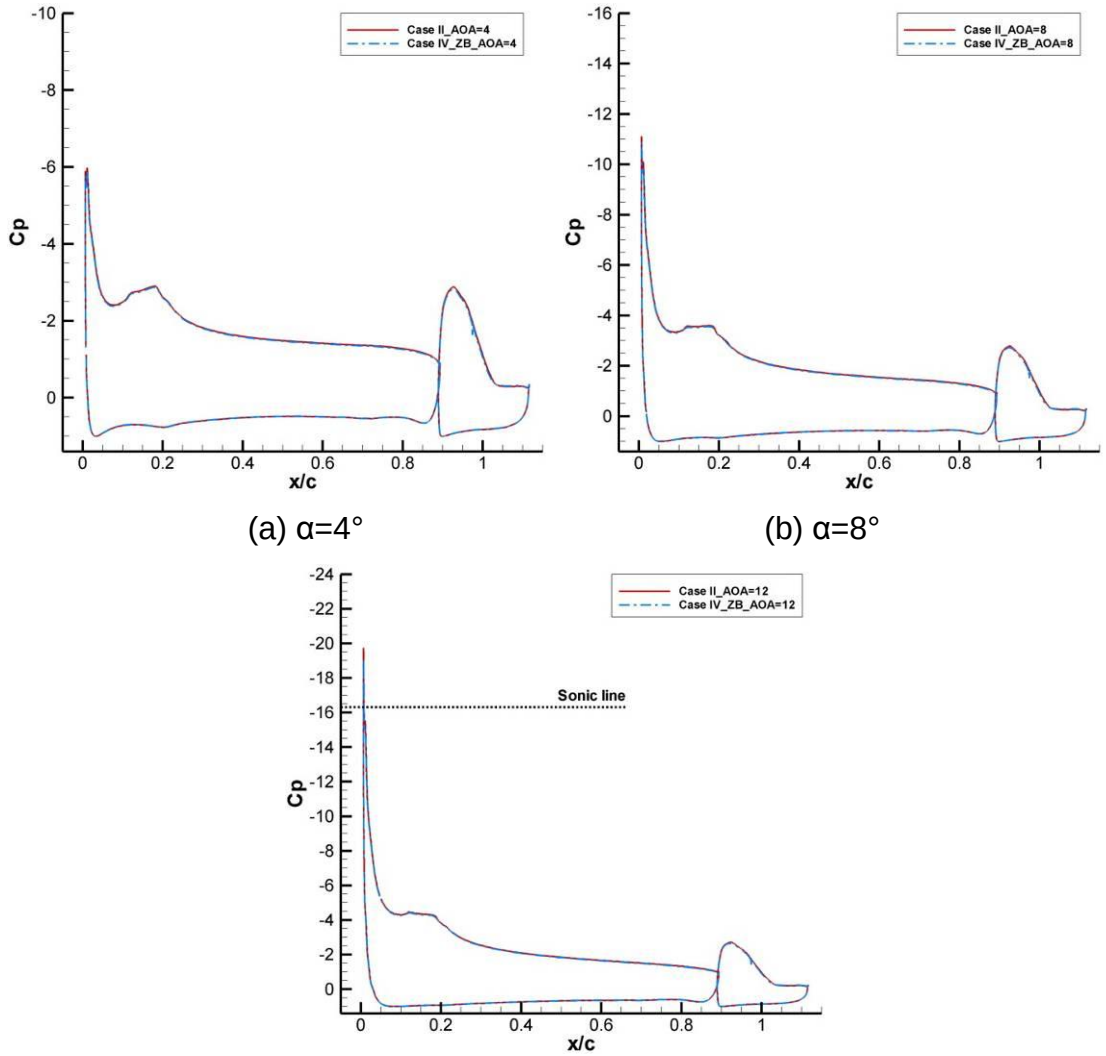

Figure 6-21 Comparison of C_p distribution (Case II & IV, ZB)

Low-blowing rate (LBR) – Quantitative results are listed in table 6-7. Approximately 2% lift enhancement was achieved with a jet of low-blowing rate. 6% drag reduction was found at both α=4° and α=8°, but C_D only decreased by 2% at α=12°. Despite these, 17% less C_μ was also observed at all the tested incidences which indicated the non-tangential blowing might be less demanding than the tangential one.

As in Case III, no flow acceleration was found on the main element. But the non-tangential blowing slightly bent the local flow upward and induced flow accelerations in the near-wall region where the C_p curve experienced a sudden rise (see Fig. 6-24). Due to the low C_μ and previously discussed flow mixing, the

injected flow fully merged with the incident flow at around 40%c_{flap}. Compared to Case III, It seems that the non-tangential blowing would enhance the mixing between the incident and injected flow. Though the extra momentum was clearly not enough to prevent the separation from happening, it did decrease the size of the separation region. Separation occurred at 60% flap chord for all tested incidences. At 12° angle of attack, the occurrence of the supersonic region at the leading edge and the breakdown of main element wake flow was observed (see Fig. 6-22.c) as in Case III.

Table 6-7 Results of simulation (Case IV, LBR)

α	C_μ	C_L	C_D	L/D	C_M
4°	0.0041	2.6720	0.046	58.09	-0.6395
8°	0.0039	3.0963	0.0524	59.09	-0.6252
12°	0.0038	3.4977	0.0635	55.08	-0.6035

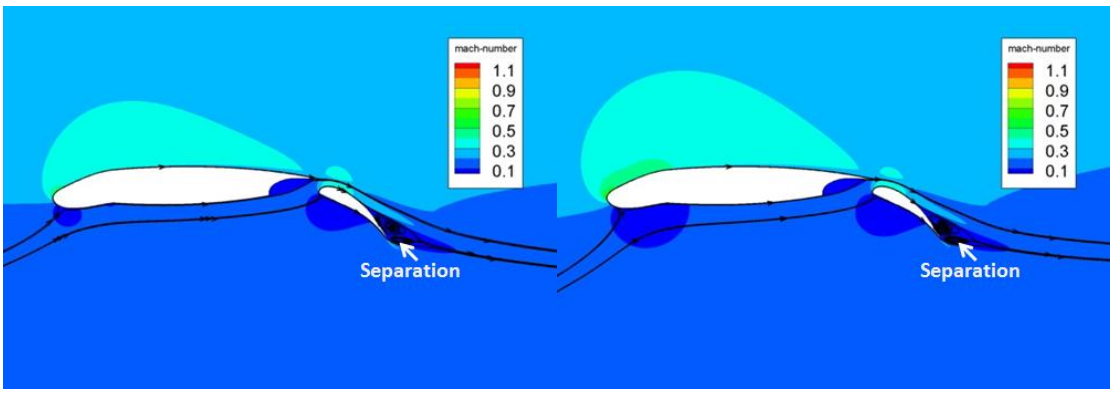

(a) α=4° (b) α=8°

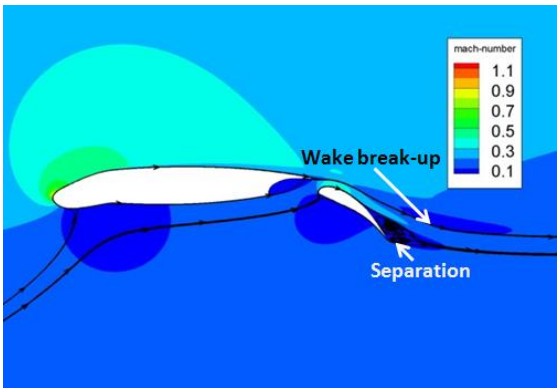

(c) α=12°

Figure 6-22 Streamline and contour of Mach number (Case IV, LBR)

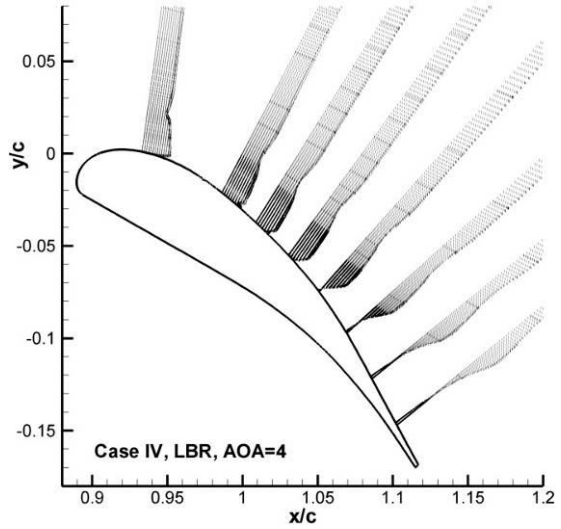

(a) α=4°

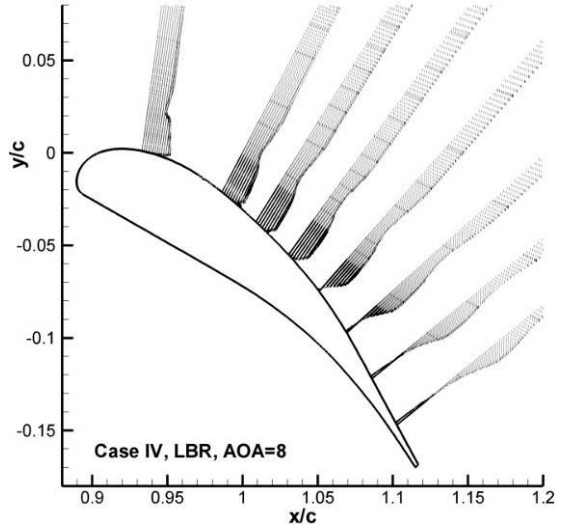

(b) α=8°

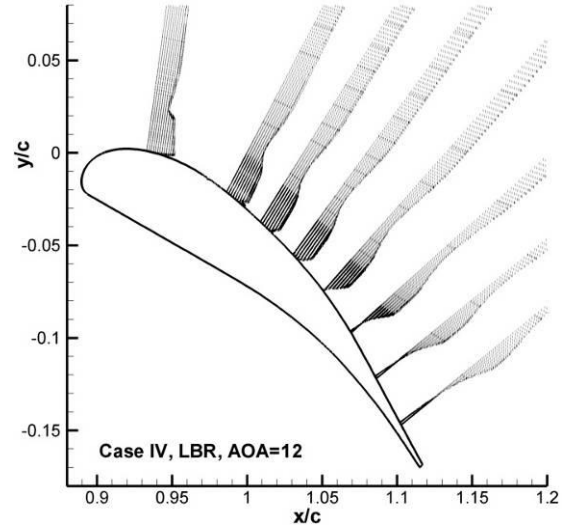

(c) α=12°

Figure 6-23 Velocity profile on the flap upper-surface (Case IV, LBR)

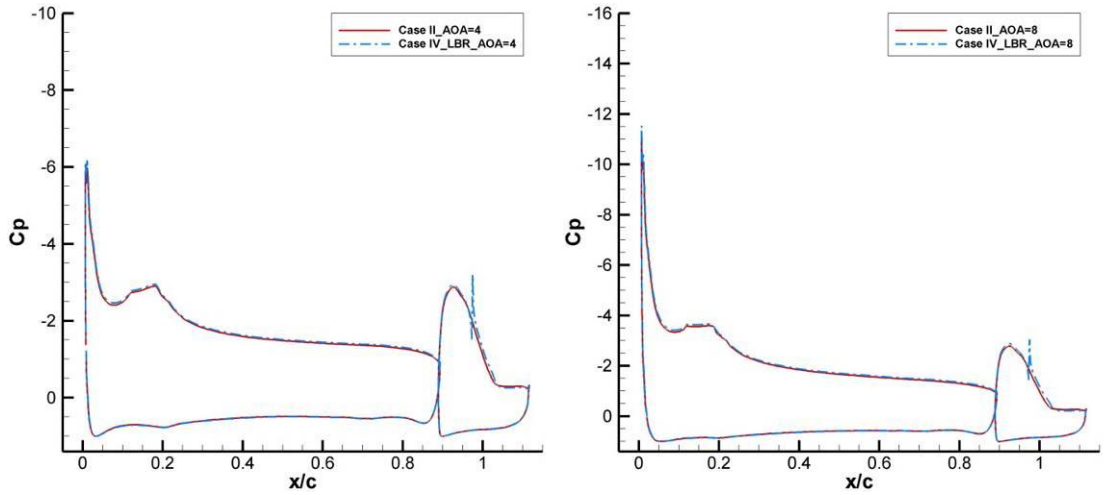

(a) α=4°

(b) α=8°

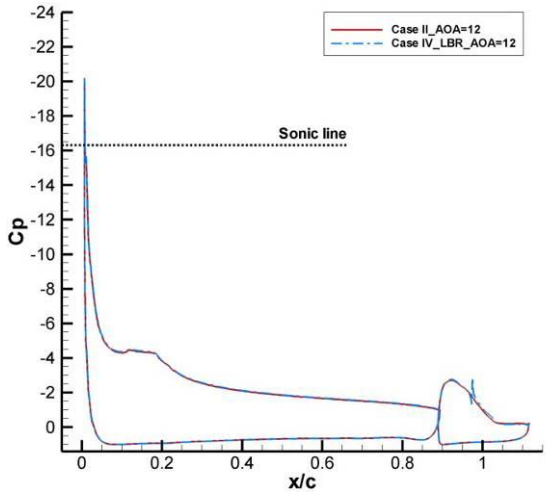

(c) α=12°

Figure 6-24 Comparison of C_p distribution (Case II & IV, LBR)

Medium-blowing rate (MBR) – Quantitative results for Case IV are listed in table 6-8. As in Case III, approximate linear rise of the lift curve was found. 10% of lift enhancements were found at α=4° and α=8°, while 8% was observed at α=12°. The drag curve, which was similar to the Case III, also jumped when the incidence reached 12° where only 1% drag reduction was achieved. For α=4°, the blowing reduced the drag by 21% and 18% reduction was obtained at α=8°.

Flow-visualization results were shown in Fig. 6-25. The wake of the main element was found to be broken at both α=8° and α=12°, but not at α=4°. Separation on the flap was observed at all three incidences. At α=4° and α=8°, separation was found at 70%c_{flap} (see Fig. 6-26). The blowing seemed to have

better efficiency at higher angle of attack, as less C_μ applied and the separation was observed at 80% flap chord for the 12° angle of attack. However, a larger supersonic region was found at the leading edge when the blowing was applied, and thus induced larger drag. This explained why less C_D reduction was obtained for this incidence condition.

Table 6-8 Results of simulation (Case IV, MBR)

α	C_μ	C_L	C_D	L/D	C_M
4°	0.0065	2.9202	0.0383	76.25	-0.7092
8°	0.0064	3.3494	0.0458	73.13	-0.6939
12°	0.0060	3.7246	0.0640	58.20	-0.6646

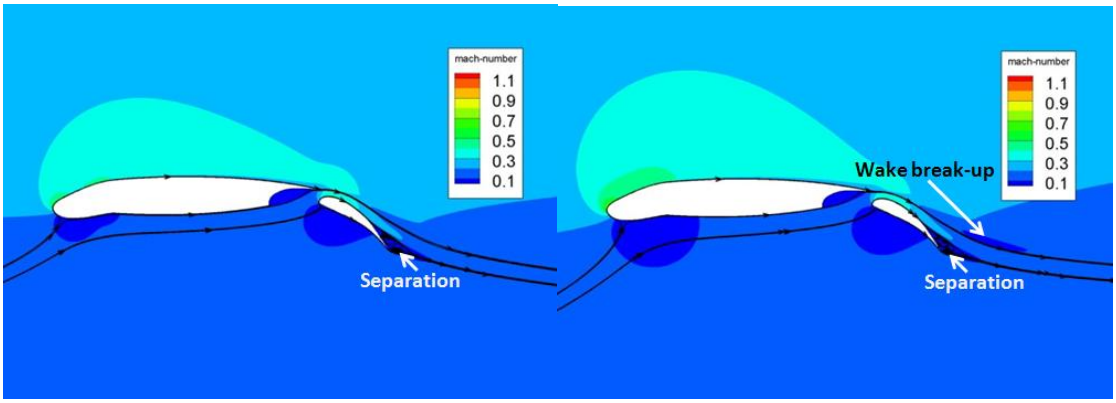

(a) α=4° (b) α=8°

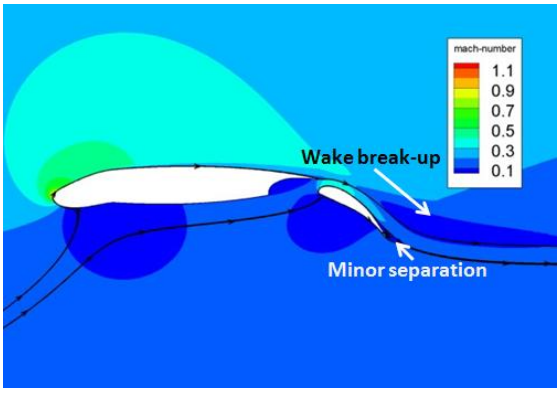

(c) α=12°

Figure 6-25 Streamline and contour of Mach number (Case IV, MBR)

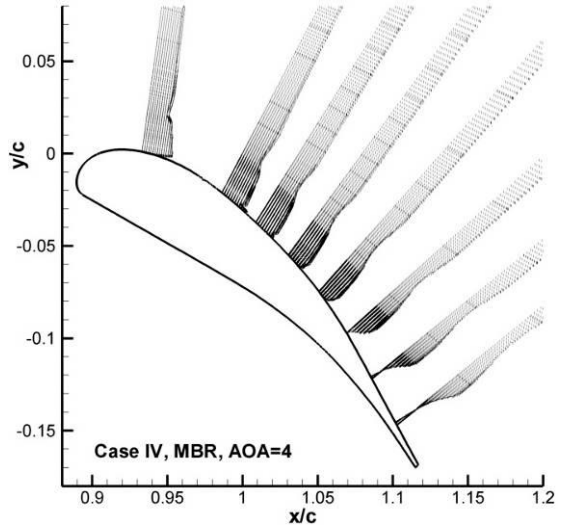

(a) α=4°

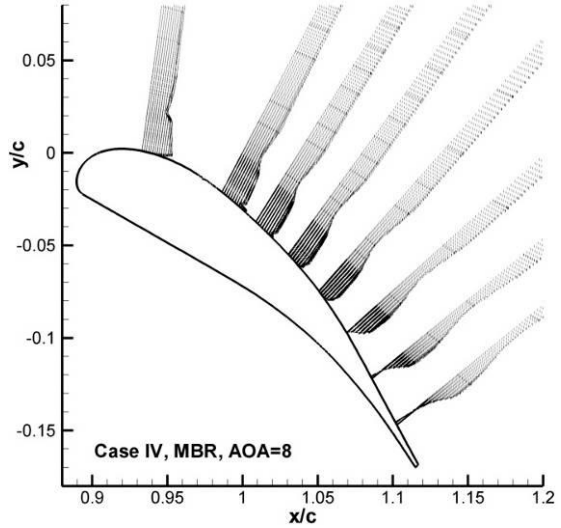

(b) α=8°

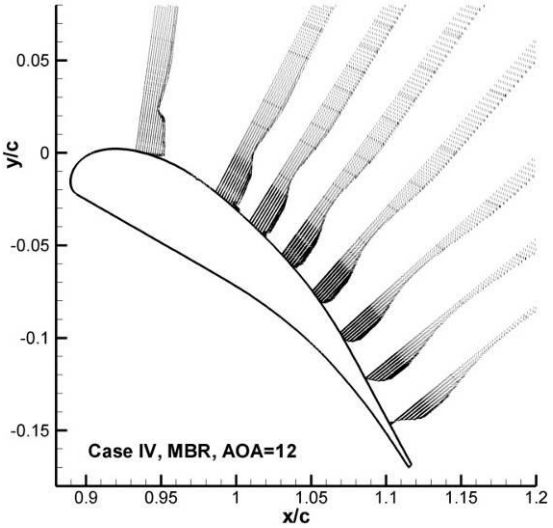

(c) α=12°

Figure 6-26 Velocity profile on the flap upper-surface (Case IV, MBR)

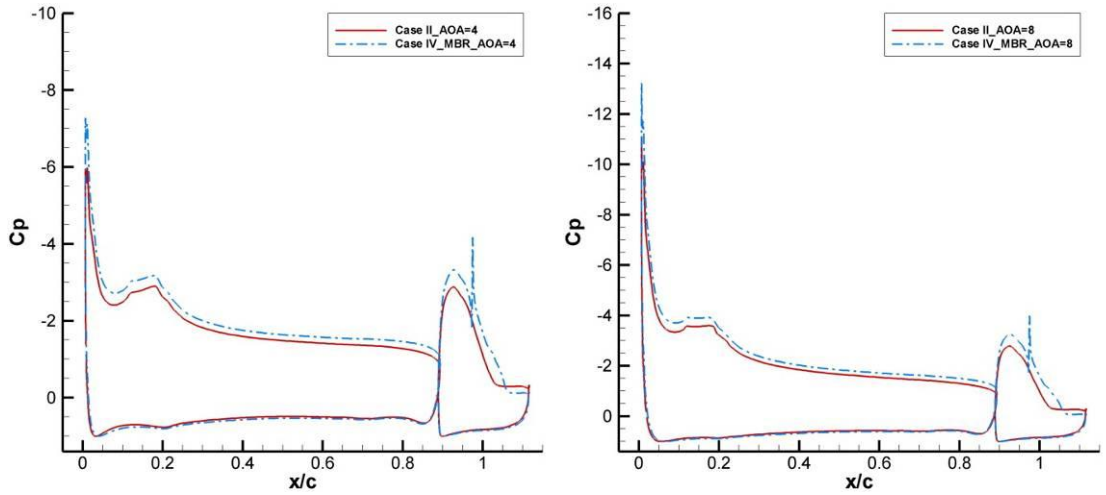

(a) α=4°

(b) α=8°

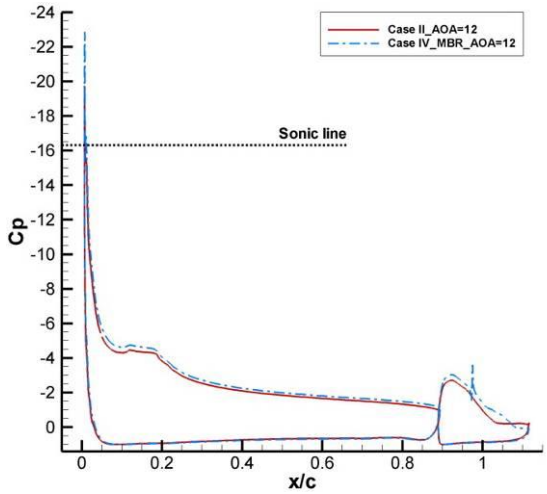

(c) α=12°

Figure 6-27 Comparison of C_p distribution (Case II & IV, MBR)

The velocity profile (see Fig. 6-26) showed that the jet and incident flow had fully mixed near 40% flap chord at α=4° and α=8° and near 50% flap chord at α=12°.

High-blowing rate (HBR) - Quantitative results are shown in table 6-9. The computed force coefficients of Case IV were quite similar to that of Case III. The lift increased by almost 25% at α=4°, and rose by 21% at α=8°. But the slope of the lift curve then decreased with the further increased incidence of attack (see Fig.6-18). At α=12°, 10% lift enhancement was achieved. The drag curve also swung downward as the angle of attack increased, which was the same for the tangential blowing case. At α=4°, almost 30% of the total drag had been

decreased by the upper-surface blowing. When the airfoil's incidence reached 8°, this figure dropped to 20%. Dramatic drag increase was found at 12° again, where the total-drag of the airfoil was increased by 6%.

Table 6-9 Results of simulation (Case IV, HBR)

α	C_μ	C_L	C_D	L/D	C_M
4°	0.0097	3.2666	0.0343	95.24	-0.8100
8°	0.0094	3.6619	0.0443	82.66	-0.7822
12°	0.0087	3.8113	0.0686	55.56	-0.6900

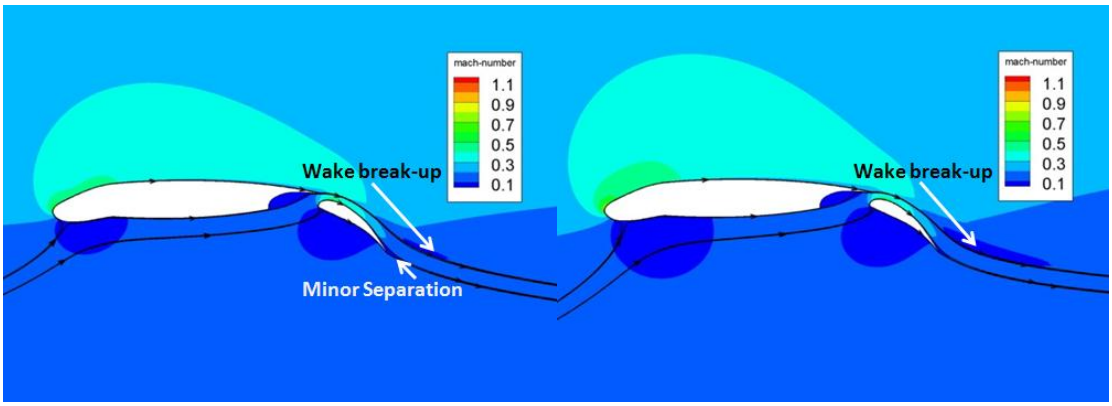

(a) α=4° (b) α=8°

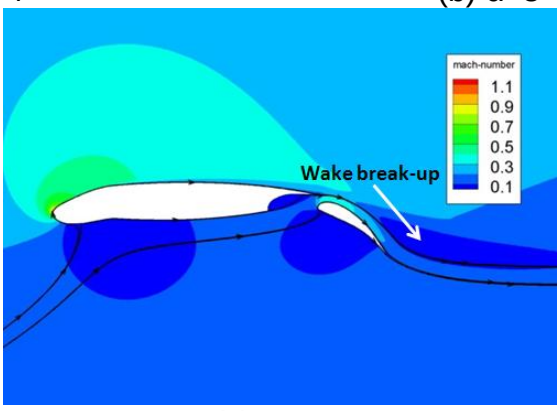

(c) α=12°

Figure 6-28 Streamline and contour of Mach number (Case IV, HBR)

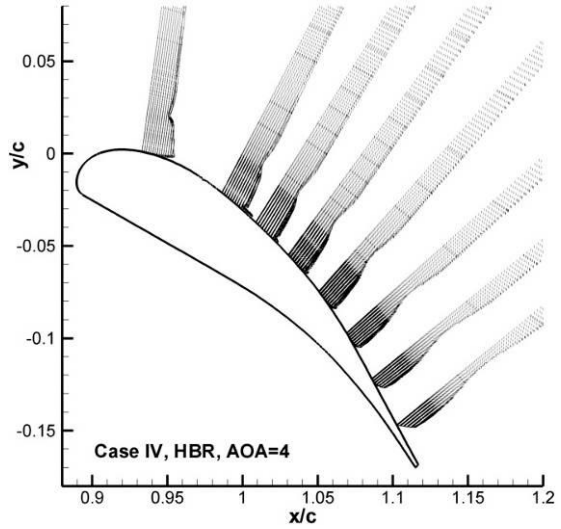

(a) α=4°

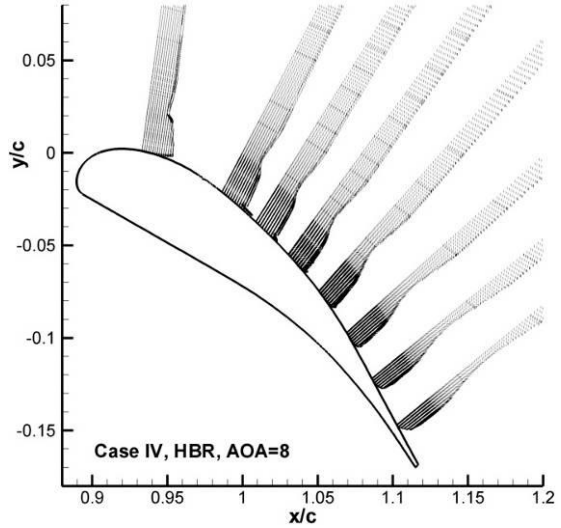

(b) α=8°

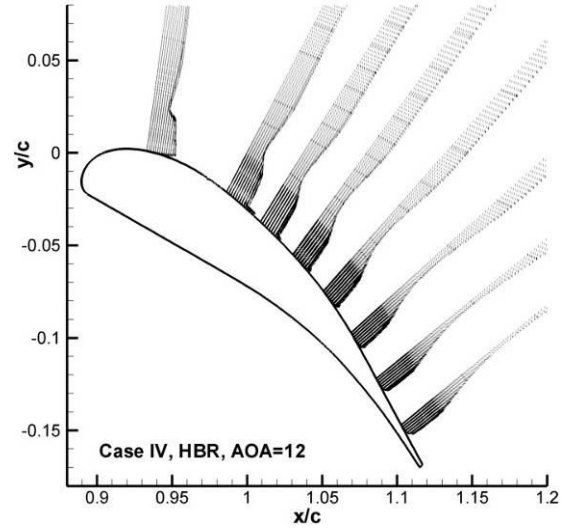

(c) α=12°

Figure 6-29 Velocity profile on the flap upper-surface (Case IV, HBR)

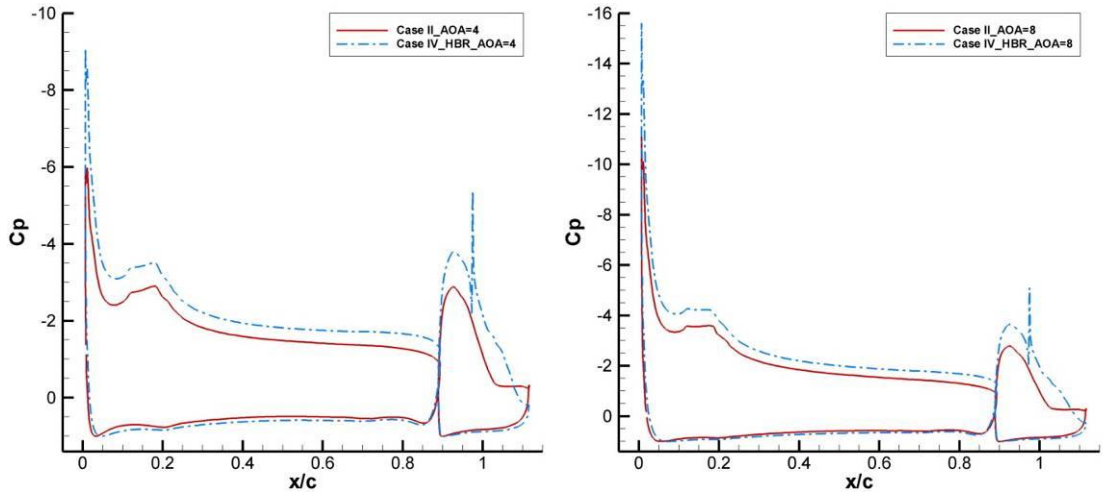

(a) α=4°

(b) α=8°

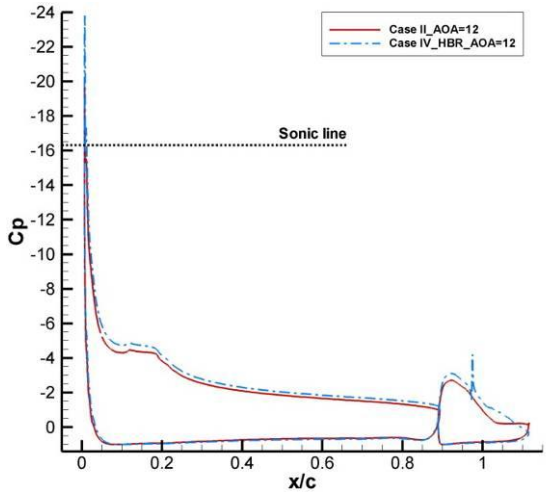

(c) α=12°

Figure 6-30 Comparison of C_p distribution (Case II & IV, MBR)

With the high-blowing rate, the injected momentum prevented any significant separation from happening, especially at α=12° where the separation was totally eliminated from the flap upper-surface. For the other two incidence conditions, Minor separation was found at the trailing edge (see Fig. 6-29). But on the other hand, the elimination of separation also induced the downward bending of flow above the flap and resulted in the breakdown of main element wake. Even at α=4°, minor wake break-up was found over the flap. Normally, this phenomenon would not be observed at such a low angle of attack.

The velocity profile (see Fig. 6-29) showed that the jet and incident flow had fully mixed near around 70%c_{flap} at α=4° and α=8°. As in Case III, the

separation occurred at 80%c_{flap} for 4° incidence condition and 90%c_{flap} for 8° incidence condition. The separation on the flap was not observed at α=12°

6.3 Summary

According to the prediction results, a further increase in the camber of the flap will not benefit the aerodynamic performance of the baseline airfoil, if the separation on the flap is not properly controlled.

Once the upper-surface blowing is employed with sufficient blowing momentum, huge improvement in lift, drag and efficiency of the baseline airfoil could be achieved. At low angles-of-attack, higher blowing momentum will lead to better lift enhancement and drag reduction, and hence greatly increase the airfoil's efficiency. For higher incidence, e.g. 12°, the performance enhancing capability of the blowing jet is limited by the breakdown of the wake of the main element. And the flow reaches sonic speed at the leading edge which becomes a major factor of soaring drag, too. Taking this into consideration, a jet of medium blowing rate will lead to better efficiency at higher angle of attack. The decrease of the slope of C_L curve also indicates that the $\alpha_{CL\,max}$ might have been changed due to the maximum blowing momentum. As only three different incidences have been studied, further studies should be carried out.

For the blowing slot, better designs should be based on the principle of not modifying the airfoil profile too much as it will trigger separation and introduce a drag penalty. Bearing this in mind, the non-tangential blowing configuration was developed and tested. Predictions showed the new design was competent. Besides, from the computed results, the non-tangential blowing has the possibility of enhancing the mixing between the incident and injected flow which, as previously discussed, has negative effect on the blowing. Though separation has been changed due to different blowing configuration, the force coefficients have barely been affected.

7 Conclusion and Future work

Four different cases including two flap configurations and two blowing designs have been studied. The key features of each studied cases are summarised in this chapter. Suggestions for future work are also presented.

7.1 Summary of the results

Two baseline cases including normal flap (Case I) and high-camber flap (Case II) were tested and compared at the beginning of this study. It was found that the aerodynamic performance of the airfoil was not enhanced by the further increase in flap camber, due to a larger separation region on the flap. When the airfoil's incidence reached 12°, flow velocity exceeded Mach 1 at the airfoil's leading edge and the breakdown of main element wake flow was observed over the flap.

Then, upper-surface blowing has been applied on the high-camber flap configuration. Two blowing methods have been studied: tangential blowing (Case III) and non-tangential blowing (Case IV). In addition, the effects of two parameters, including the blowing momentum coefficient (C_μ) and the airfoil's incidence, have been analysed. Generally speaking, computed results showed that both blowing methods were quite effective against separation once sufficient blowing momentum was applied. For the tested blowing slot designs, the non-tangential blowing showed its advantage in avoiding the drag penalty when the blowing system was off.

For both blowing configurations, there was no significant difference in airfoil's performance between Case III and Case IV when a jet of high-blowing rate was applied. At α=4°, the separation on the flap was delayed by the blowing and occurred at 80%c_{flap} for both blowing cases. Increased flow velocity was not only found on the flap, but also on the upper surface of the main element. Consequently, approximately 25% lift enhancement and 30% drag reduction were found at this condition for each blowing configuration, according to the numerical prediction. At α=8°, the separation on the flap was observed at

90%c_{flap}, and 20% lift enhancement and 22% drag reduction of the airfoil was obtained. For 12° incidence condition, the elimination of separation on the flap led to a significant curvature of the main element wake flow, and thus caused its breakdown. 10% lift enhancement was found for each case, whilst the drag of the baseline airfoil was increased by 4% for Case III and 6% for Case IV.

For medium-blowing rate condition, both blowing cases were able to delay the separation, but failed to eliminate it. At α=4°, the separation on the flap was observed near 70%c_{flap} for both blowing cases. Approximately 11% lift enhancement and 21% drag reduction were found at this condition. For 8° incidence condition, the separation was found at the same position on the flap, whilst 10% lift increase and 18% drag reduction were observed. When the airfoil's incidence reached 12°, the separation was further delayed by the blowing to near 80%c_{flap}. Though the separation was delayed further downstream, only 8% lift enhancement was found due to the significant effect of the break-up of the main element wake flow. The drag was found 5% less for Case III and 1% less for Case IV in comparison with the computed result from Case II.

For low-blowing rate condition, the injected flow did not have enough momentum to penetrate the adverse pressure gradient, and thus the position where the separation occurred was barely changed. The separation on flap occurred at 60%c_{flap} for all tested cases and incidence conditions. Approximately 2% lift enhancement was achieved with a jet of low-blowing rate under each tested condition. For tangential blowing, 4% of drag reduction at α=4° and 5% at α=8° was obtained, whilst less than 2% drag reduction was found. For non-tangential blowing, 6% drag reduction was achieved at both α=4° and α=8°. At α=12°, only 2% decrease of C_D was found.

The effects of the blowing slots were tested when the blowing systems were shut down. For the tangential blowing, the blowing slot and the modified flap upper surface formed a backward facing step-like profile which triggered the separation and led to deterioration of airfoil's performance. Approximately 8% lift loss and more than 10% drag penalty was introduced. But for the non-

tangential blowing, no drag penalty was observed as only a small gap was added to the flap upper surface.

7.2 Future work

The upper surface blowing has been proved to be quite effective against separation on flap. But the mixing between the injected and incident flow limits the performance enhancing capability of blowing. How to preserve the injected momentum should be analysed. Also, the location and the shape of the slot should be optimized for better performance. In addition, certain flow control device can be applied to the main element for wake flow control. This will help to further enhance the aerodynamic performance of the baseline airfoil, especially at higher angle of attack.

As only CFD has been involved in this study, experimental testing definitely needs to be undertaken in the future. In addition, using more advanced computational approaches will also benefit this study.

REFERENCES

[1]. Akansu, Y.E., Firat, E., Control of Flow around a Square Prism by Slot Jet Injection from the Rear Surface, Experimental Thermal and Fluid Science, Vol. 34, pp. 906-914, 2010.

[2]. Anders, S.G., Sellers III, W.L., and Washburn, A.E., Active Flow Control Activities at NASA Langley, AIAA paper 2004-2623, 2004.

[3]. Anderson, W.K., Bonhaus, D.L., McGhee, R.J., Walker, B.S., Navier-Stokes Computations and Experimental Comparisons for Multi-Element Airfoil Configurations, AIAA Paper 93-0645, January 1993.

[4]. Bertelrud, A., Transition on a Three-Element High Lift Configuration at High Reynolds Numbers, AIAA Paper 98-0703, January 1998.

[5]. Butter, D.J., Recent Progress on Development and Understanding of High-Lift-Systems, AGARD-CP 365, 1984.

[6]. Carrannanto, P.G., Storms, B.L., Ross, J.C., Cummings, R.M., Navier-Stokes analysis of lift-enhancing tabs on multi-element airfoils, Aircraft Design, Vol. 1, pp. 145-158, 1998.

[7]. Chin, V.D., Peters, D.W., Spaid, F.W., McGhee, R.J., Flowfield Measurements about A Multi-Element Airfoil at High Reynolds Numbers, AIAA Paper 93-3137, July 1993.

[8]. Collis, S.S., Joslin, R.D., Seifert, A., Theofilis, V., Issues in Active Flow Control: Theory, Control, Simulation, and Experiment, Progress in Aerospace Sciences, Vol. 40, pp. 237-289, 2004.

[9]. Donovan, J.F., Kral, L.D., and Cary, A.W., Active Flow Control Applied to an Airfoil, AIAA Paper 98-0210, January 1998.

[10]. Dominik, C.J., Application of the Incompressible Navier-Stokes Equations to High-Lift Flows, AIAA Paper 94-1872, June 1994.

[11]. Ekaterinaris, J.A., Preditction of Active Flow Control Performance on Airfoils and Wings, Aerospace Science and Technology, Vol. 8, pp. 401-404, 2004.

[12]. Eldredge, R., Bons, J., 2004. Active Control of a Separating Boundary Layer with Steady Vortex Generating Jets. Detailed Flow Measurements. AIAA paper 2004-751.

[13]. Erm, L.P., 2001. Parametric study of jet/vortex interactions in AMRL water tunnel Technical report, DSTO-TR-1209, Defense Science and Technology.

[14]. Ferziger, J.H., Introduction to the Physics and Simulation of Turbulence, Introduction to the Modeling of Turbulence. Vol. VKI Lecture Series 1997-03, Von Karman Institute, 1997.

[15]. Gad-el-Hak, M., Flow Control – Passive, Active, and Reactive Flow Management, Cambridge University Press, 2000.

[16]. Garner, P.L., Meredith, P.T., and Stoner, R.C., Areas for Future CFD Development as Illustrated by Transport Aircraft Applications, AIAA Paper 91-1527, 1991.

[17]. Godard, G., and Stanislas, M., Control of a Deceleration Boundary Layer. Part 1: Optimization of Passive Vortex Generators, Aerospace Science and Technology, Vol. 10, pp. 181-191, 2006.

[18]. Godard, G., Foucaut, J.M., and Stanislas, M., Control of a Deceleration Boundary Layer. Part 2: Optimization of Slotted Jets Vortex Generators, Aerospace Science and Technology, Vol. 10, pp. 394-400, 2006.

[19]. Godard, G., and Stanislas, M., Control of a Deceleration Boundary Layer. Part 2: Optimization of Round Jets Vortex Generators, Aerospace Science and Technology, Vol. 10, pp. 455-464, 2006.

[20]. Hirsch, C., Numerical Computation of Internal and External Flows, the Fundamentals of Computational Fluid Dynamics, 2nd. Edition, ELSEVIER, 2007.

[21]. Hoffmann, K.A., and Chiang, S.T., Computational Fluid Dynamics, EES, Whichita, 2000.

[22]. Jones, K.M., Biedron, R.T., Whitlock, M., Application of a Navier-Stokes Solver to the Analysis of Multi-Element Airfoils and Wings Using Multi-Zonal Grid Techniques, AIAA Paper 95-1855, June 1995.

[23]. Klausmeyer, S.M., Lin, J.C., An Experimental Investigation of Skin Friction on a Multi-Element Airfoil, AIAA Paper 94-1870, June 1994.

[24]. Klausmeyer, S.M., Lin, J.C., Comparative Results from a CFD Challenge over a 2d Three-element high-lift airfoil. NASA TM 112858, May 1997.

[25]. Lee-Rausch, E.M., Vatsa, V.N., Rumsey, C.L., Computational Analysis of Dual Radius Circulation Control Airfoils, 36th AIAA Fluid Dynamics Conference, San Francisco, California, June 2006.

[26]. Lamballais, E., Silvestrini, J., and Laizet, S., Direct Numerical Simulation of a Separation Bubble on a Rounded Finite-Width Leading Edge, International Journal of Heat and Fluid Flow, Vol. 29, pp. 612-625, 2008.

[27]. Lynch, F.T., Potter, R.C., Spaid, F.W., Requirements for Effective High Lift CFD, International Council of the Aeronautical Sciences Proceedings, 20th Congress, Vol. 2. Reston, VA: AIAA, 1996.

[28]. Marques, M., Gamboa, P., and Andrade, E., Design of a Variable Camber Flap for Minimum Drag and Improved Energy Efficiency, AIAA Paper 2009-2196, 2009.

[29]. McGinley, C.B., Anders, J.B., Spaid, F.W., Measurements of Reynolds Stress Profiles on a High-Lift Airfoil, AIAA Paper 98-2620, June 1998.

[30]. Morrison, J.H., Numerical Study of Turbulence Model Predictions for the MD 30P/30N and NHLP-2D Three-Element Highlift Configurations, NASA/CR-1998-208967, 1998.

[31]. Pfingsten, K. C., Jensch, C., Körber, K.W., and Radespiel, R., Numerical Simulation of the Flow Around Circulation Control Airfoils, First CEAS European Air and Space Conference, Berlin, Germany, September 2007.

[32]. Reckzeh, D., Aerodynamic Design of the High-lift-wing for Megaliner Aircraft, Aerospace Science and Technology, Vol. 7, pp. 107-119, 2003.

[33]. Rogers, S.E., Menter, F.R., Durbin, P.A., Mansour, N.N., A Comparison of Turbulence Models in Computing Multi-Element Airfoil Flows, AIAA Paper 94-0291, January 1994.

[34]. Ross, J.C., Storms, B.L., Carrannanto, P.G., Life-enhancing Tabs on Multi-element Airfoils, AIAA Journal of Aircraft, Vol. 32, pp. 649-655, 1995.

[35]. Rudolph PKC. High-Lift Systems on Commercial Subsonic Airliners. NASA CR 4746, September 1996.

[36]. Rumsey, C.L., Lee-Rausch, E.M., Watson, R.D., Three-Dimensional Effects on Multi-Element High-Lift Computations, AIAA Paper 2002-0845, January 2002.

[37]. Rumsey, C.L., and Ying, S.X., Prediction of High Lift: Review of Present CFD Capability, Progress in Aerospace Sciences, Vol. 38, pp. 145-180, 2002.

[38]. Rumsey, C.L., Spalart, P.R., Turbulence Model Behavior in Low Reynolds Number Regions of Aerodynamic Flowfields, 38th AIAA Fluid Dynamics Conference and Exhibit, Seattle, WA, June 23-26, 2008.

[39]. Saguat, P., Large Eddy Simulation for Incompressible Flows: An Introduction, Springer, 2006.

[40]. Shan, H., Jiang, L., and Liu, C., Direct Numerical Simulation of Flow Separation around a NACA 0012 Airfoil, Journal of Computers & Fluids, Vol. 34, pp. 1096-1114, 2005.

[41]. Siauw, W.L., et al, “Transient dynamics of the flow around a NACA 0015 airfoil using fluidic vortex generators”, International Journal of Heat and Fluid Flow, Vol. 31, pp. 450-459, 2010

[42]. Sondergaard, R., Rivir, R.B., Bons, J.P., Control of low-pressure turbine separation using vortex generators. J. Propulsion Power, Vol. 18, pp. 889–895, 2002.

[43]. Spalart, P.R., and Allmaras, S.R., A One-Equation Turbulence Model for Aerodynamic Flows, AIAA 92-0439, January 1992.

[44]. Stanewsky, E., Adaptive Wing and Flow Control Technology, Progress in Aerospace Sciences, Vol. 37, pp. 583-667, 2001.

[45]. Stanewsky, E. and Rosemann, H., Active Flow Control Applied to Military and Civil Aircraft, RTO MP-051, May 2000.

[46]. Storms, B.L., Ross, J.C., Experimental Study of Lift-enhancing Tabs on a Two-element Airfoil, AIAA Journal of Aircraft, Vol. 32, pp. 1072-1078, 1995.

[47]. Valarezo, W.O., Mavriplis, D.J., Navier–Stokes Applications to High-Lift

Airfoil Analysis, AIAA Paper 93-3534, August 1993.

[48]. van Dam, C.P., The Aerodynamic Design of Multi-Element High-Lift Systems for Transport Airplanes, Progress in Aerospace Science, Vol. 38, pp. 101-144, 2002.

[49]. van der Burg, J. W. et al., Low Speed Maximum Lift and Flow Control, Aerospace Science and Technology, Vol. 8, pp. 389-400, 2004.

[50]. Weaver, D., McAlister, K.W., and Tso, J., Suppression of Dynamic Stall by Steady and Pulsed Upper-Surface Blowing, NASA TP-3600, 1995.

[51]. Williams, J., and Alexander, A.J., Pressure-plotting Measurements on an 8% Thick Aerofoil with Trailing-edge Flap Blowing, ARC-18487, June 1956.

[52]. You, D., and Moin, P., Active Control of Flow Separation over an Airfoil Using Synthetic Jets, Journal of Fluids and Structures, Vol. 24, pp. 1349-1357, 2008.

APPENDICES

Summary of GDP Report

A.1 Group Design Project Overview

In the detail design phase of the Flying Crane, three major tasks have been undertaken by the author: the scarf intake design, intake aerodynamic performance study and mass & CG control.

A.2 Scarf Intake Design and Performance Analysis

Scarf intake design is mainly the tradeoff between acoustic benefit and intake aerodynamic performance. The major motivation of this research is to minimize the intake pressure loss and nacelle drag. CFD approach has been involved after intake design parameters were chosen, and two different designs have been compared.

A.2.1 Background

Scarf Intake, or Negatively Scarfed Intake (NSI), is not a new concept in intake design. The reason why it has recently been revisited so many times is its acoustic benefit. Several studies have been conducted in the last decades. Some conclusions can be drawn from these studies:

1. The acoustic benefit of a scarf intake mainly depends on the scarf angle. The larger the scarf angle is the better acoustic shielding a scarf intake will have.

2. Because of the lower lip extension, a scarf intake may experience flow separation from the upper lip at static condition and increased cruise drag due to the spillage of flow over the upper external lip

A.2.2 Design Process

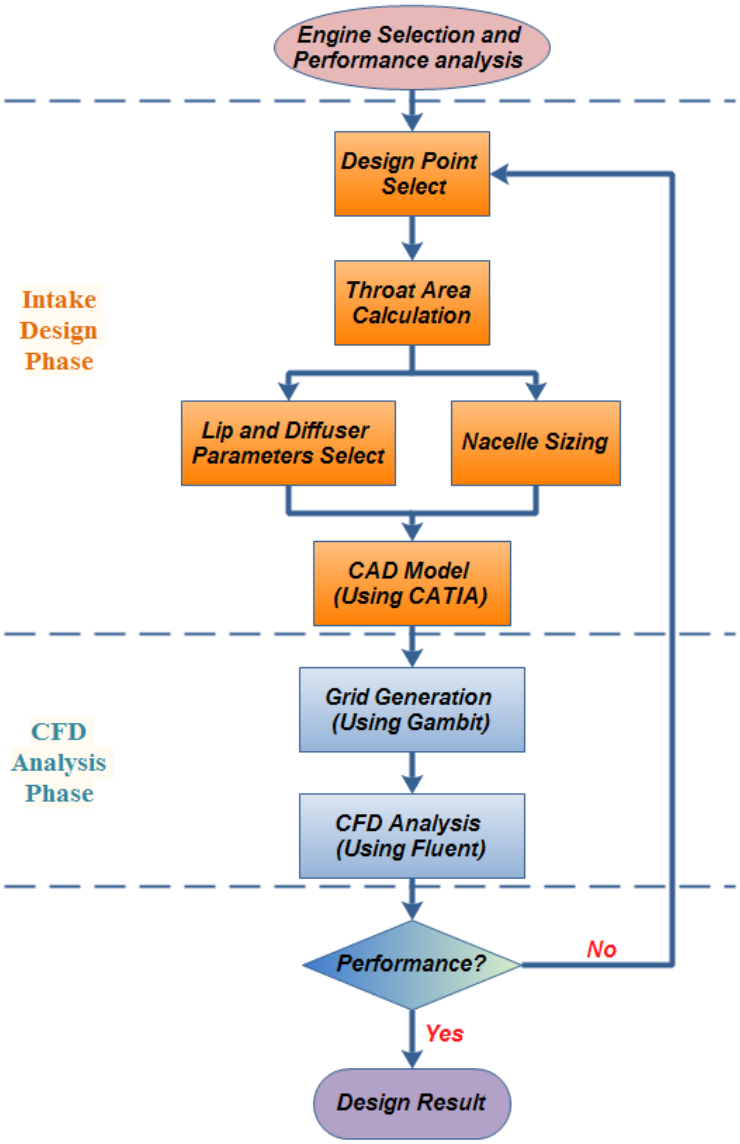

Figure A-1 Process of intake design

There were three major phases involved: firstly, the engine of the Flying Crane has been revised. This was followed by the selection of the design point and

major parameters of the intake. In this phase, two different design principles of nacelle sizing are revisited and compared. Two scarf intake designs were developed. Then, the performance of each intake design was tested and compared through computational approaches. The design flow is shown in Fig. A-1.

A.2.3 Engine Selection

According to the preliminary design, the selected engine (named the ACIMTP-I) of the Flying Crane was developed by team 1 of the 1st AVIC engine group due to its low specific fuel consumption and the high cruise net thrust. This character can fulfil the need of building the cost effective and eco-friendly Flying Crane. Major parameters of the ACIMTP-I is given as follow.

Table A-1 Engine Parameters of the ACIMTP-I

Parameters	Value
D_{FAN} (mm)	1754
FPR	1.7
BPR	6
OPR	36
COT (K)	1400

A.2.4 Scarf Intake Design

To design a scarf intake, two steps have been taken: firstly, a symmetrical intake is designed. Then, the scarf angle, or lower lip extension, is applied to the symmetrical intake to create the negatively scarfed intake.

The typical cruise condition of the Flying Crane had set to be the design point of the intake (see table A-2). The throat Mach number was chosen to be 0.66, and the throat area was 2.2115 m^2. The ellipse curve was applied to shape the lip, which had the contraction ratio of 1.25. With NACA 1-series cowling forming its forebody, the lower lip extended forward for 250mm and created the 7.6° negative scarf angle.

Table A-2 Intake Design Point

Parameters	Value
ALT (m)	11000
M_∞	0.8
W_{INTAKE} (kg/s)	175
P_0 (Pa)	34498.9
T_0 (K)	244.38

In order to define the 3D extension of the lip, two parameters are introduced: *LEC* and *θ*. The *Lip Extension Coefficient* (*LEC*) equals to the *length of* the *lip extension* (L_{LE}) divided by the *fan radius* (R_{FAN}), which is L_{LE}/R_{FAN}. And the θ is the criterion which defines the circumferential position of the lip, as shown in Fig. A-2.

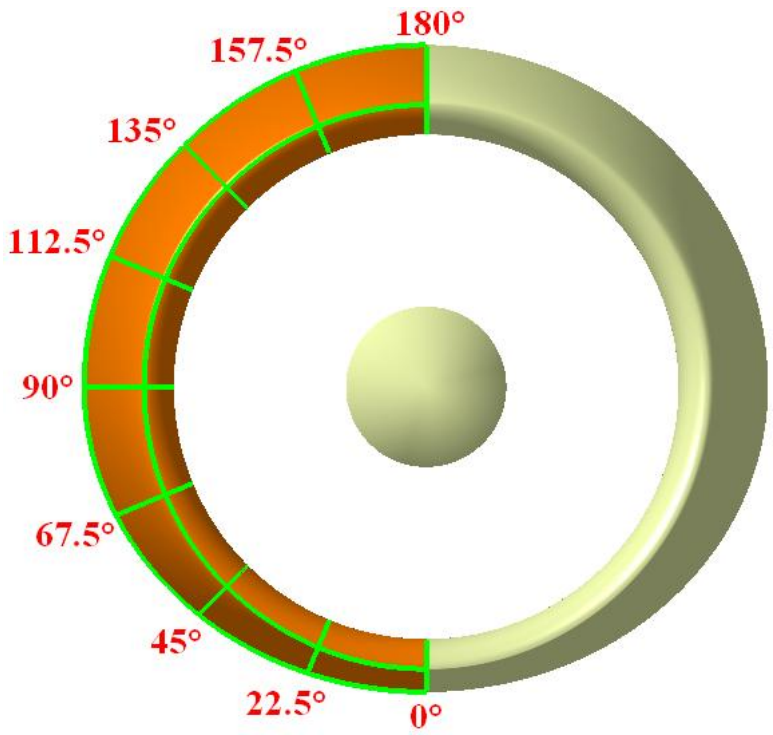

Figure A-2 Circumferential Position of the Intake Lip

For the scarf intake, the *LEC* is crucial. The larger the *LEC* is the better acoustic benefit will be obtained. But on the other hand, the large *LEC* will cause great increase in nacelle weight, and also, the aerodynamic performance of the intake will deteriorate.

For obtaining the acoustic benefit while keeping the weight increase and deterioration of the aerodynamic performance low, many works have been involved. According to Abbott and Slater (2001), added volume and weight, due to the lip extension, can be minimized through quick transition of the extended lip length from its maximum to its minimum over the 180 degrees of circumference. This approach, based on the performance results from Abbott and Slater's work, actually increase the lip extension rate with the same

extended lip length. And finishing the transition within 135 degrees rather than 180 degrees seems to be a promising solution.

Then, the intake extended lip length can be described by the following cubic equation:

$$LEC_\theta = LEC_{0^\circ}\left[2\left(\frac{\theta}{135}\right)^3 - 3\left(\frac{\theta}{135}\right)^2 + 1\right]$$

Where $0^\circ \leq \theta \leq 135^\circ$.

If $135^\circ < \theta \leq 180^\circ$, then $LEC_\theta = 0$.

In this design case, LEC_{0° is set to 0.25. *LEC* at different circumferential position are shown in table A-3.

Table A-3 *LEC* of Scarf Intake at Different Circumferential Position

θ	LEC_θ
0.0	0.250
22.5	0.232
45.0	0.185
67.5	0.125
90.0	0.065
112.5	0.019
135.0	0.000

Two different intakes, which were named as the “Slim” and the “Big”, were developed and compared using CFD approach. The only difference between these two designs was the maximum height of the nacelle, which affected the

spillage critical Massflow ratio and the drag divergence Mach number. The profiles of these intakes are shown in Fig. A-3, and design parameters are compared in table A-4.

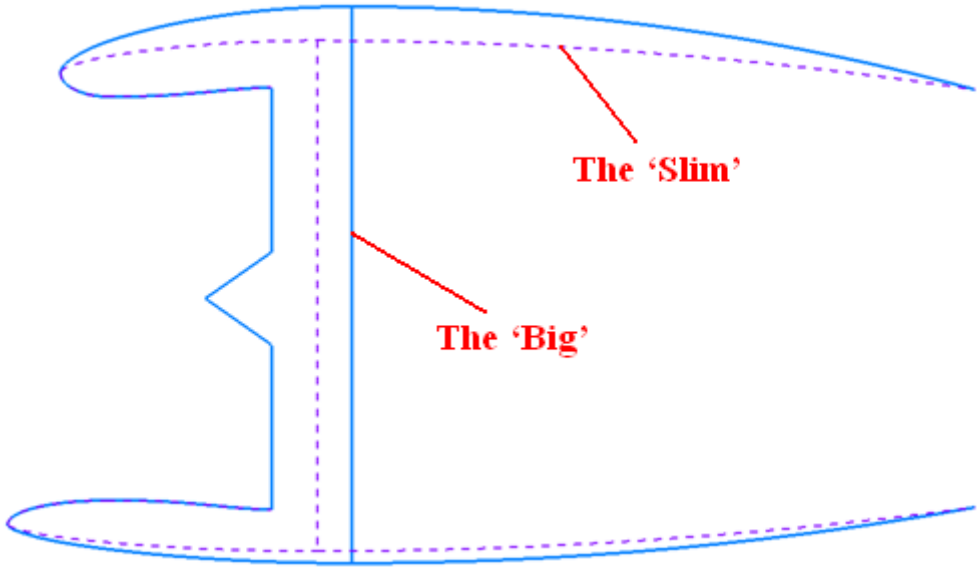

Figure A-3 Compare of Scarf Intake Profiles

Table A-4 Compare of Scarf Intake Geometry Parameters

Parameters	The 'Slim'	The 'Big'
A_{TH} (m^2)	2.21	2.21
D_{TH} (m)	1.68	1.68
A_{HI} (m^2)	2.76	2.76
D_{HI} (m)	1.88	1.88
L_{LIP} (m)	0.20	0.20
L_{IN} (m)	0.88	0.88
L_F (m)	1.07	1.21
H_{MAX} (m)	2.12	2.31
D_9 (m)	1.74	1.74
L_A (m)	2.59	2.45

A.2.5 Nacelle Performance Analysis

Two typical operation conditions of the intake had been analyzed: static condition and cruise condition (see Fig A-4 and A-5). CFD results showed that two different intakes shared the same static performance, whilst the “Big” had larger drag divergence Mach number. Due to the forward extended lower lip, the incoming stream tube of the intake had been shifted upward. This would result in a blunt upper lip design and increased the weight of the whole nacelle. So the weight issue should be taken into consideration in the future optimization. Quantitative results are shown in table A-5 and A-6.

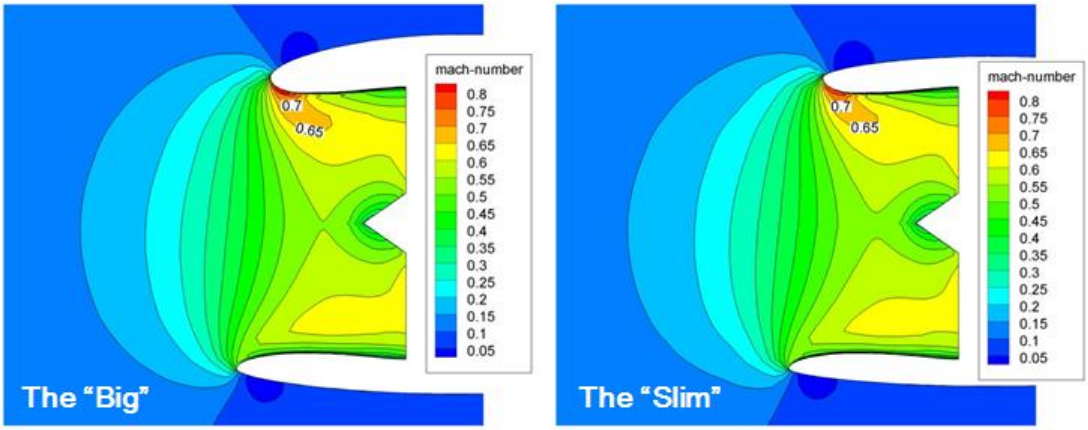

Figure A-4 Compare of Intake Flow at Static Condition

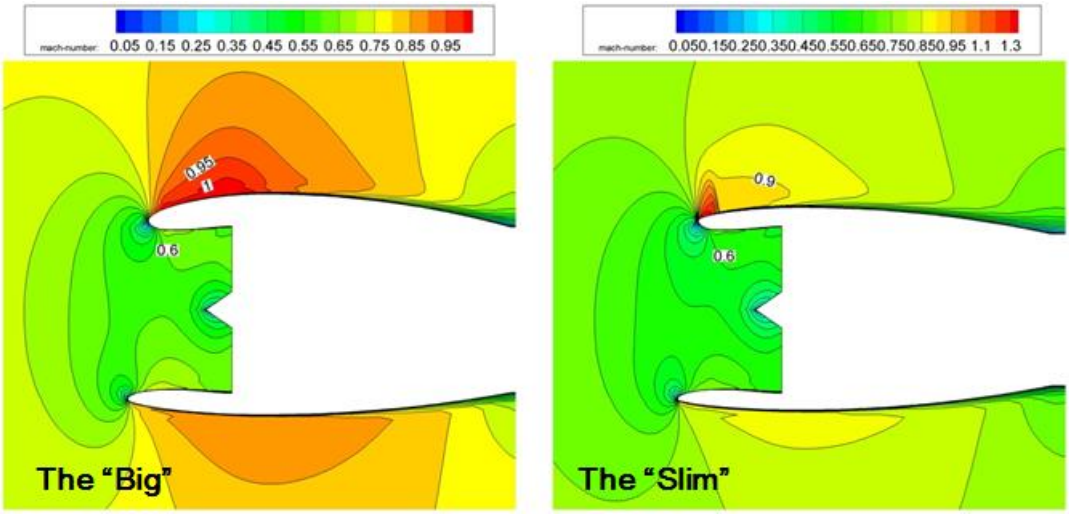

Figure A-5 Compare of Intake Flow at Cruise Condition

Table A-5 Compare of Static Performance

	M_∞	W_{INTAKE} (kg/s)	σ	M_{TH}	M_{IN}
The 'Big'	0.1	425.44	0.97	0.60	0.57
The 'Slim'	0.1	425.44	0.97	0.60	0.57

Table A-6 Compare of Cruise Performance

	M_∞	W_{INTAKE} (kg/s)	σ	M_{TH}	M_{IN}
The 'Big'	0.78	175	0.985	0.64	0.61
The 'Slim'	0.78	175	0.985	0.64	0.61

Nacelle/wing interference has been analysis through CFD approach, too. In this phase, the nacelle was simplified as a free flow nacelle and only the "Big" configuration was tested. The existence of nacelle slightly increases the lift of the wing, but affects the drag of the wing much greater, which results in a significant decrease, about 5, in lift-to-drag ratio (see Fig. A-8).

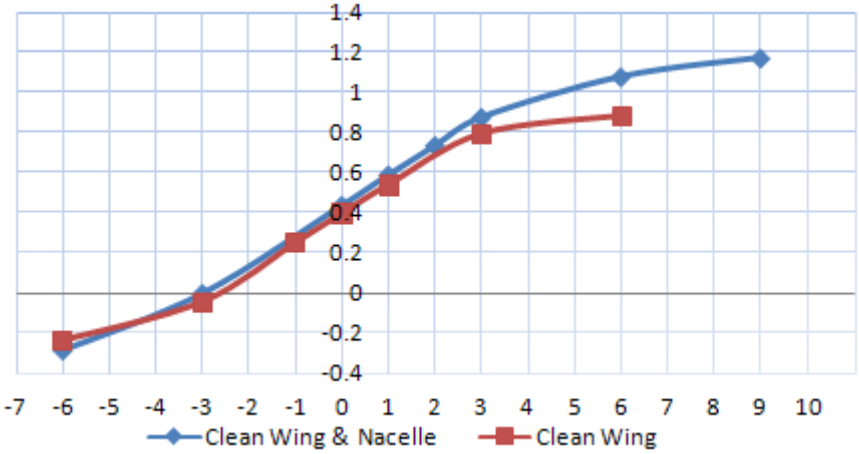

Figure A-6 Compare of C_L at Different Angle of Attack

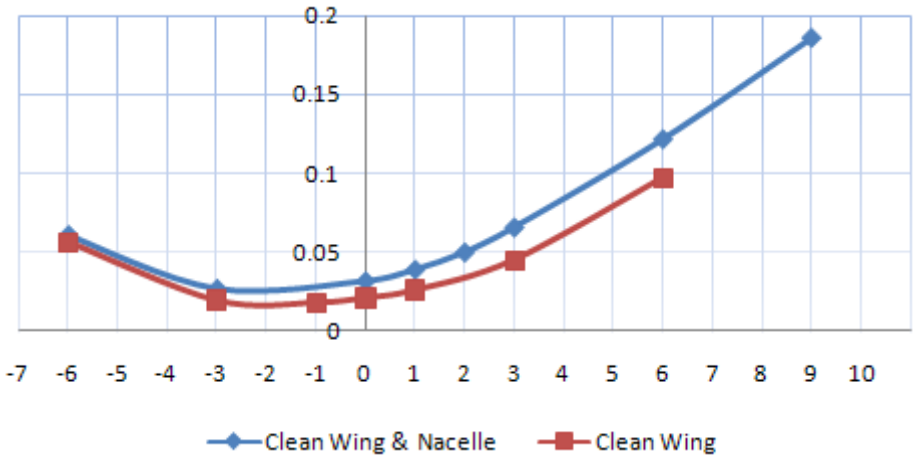

Figure A-7 Compare of C_D at Different Angle of Attack

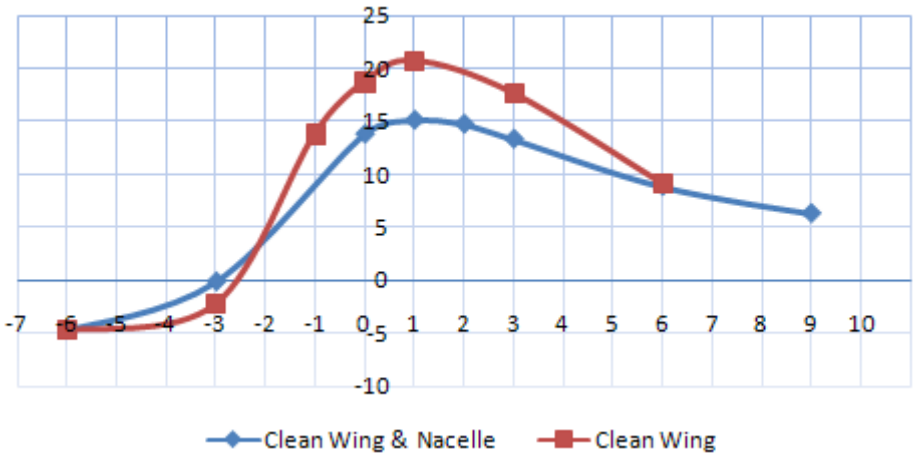

Figure A-8 Compare of C_L/C_D at Different Angle of Attack

A.3 Mass and CG

For the Flying Crane, the maximum take-off mass (*MTOM*) had been set to 64,582kg with the CG_X of 28%*MAC* (16.63m from the nose) in conceptual design phase. The *CG* limit was also obtained, which is 12%*MAC* to 35%*MAC*, based on two different extreme payload distribution conditions (half payload forward and half payload afterward).

In the preliminary design stage, mass and *CG* had been updated along with the latest and more detailed designs, whilst the *MTOM* and *CG* limit remained the

same. A huge structural mass reduction (4,035kg) of the Flying Crane was found in preliminary design phase due to the change of material of the structure. In detail design phase, this was also carefully checked and updated along with design updates.

During the detail design phase, the main target of mass and *CG* control was to maintain the *MTOM* (64,582kg) while increasing the structure efficiency and maximizing the payload capacity. The *CG* position should also be controlled in an agreeable range. In addition, the designer predicted the payload assuming that the average weight of an individual passenger was 70kg in preliminary design phase. Unfortunately, the latest survey showed that the average weight of the passengers was increased dramatically during recent years, and the "70kg" assumption was out of date. So the payload of the Flying Crane must be recalculated.

According to the latest results, the structural mass reduction was 1,965kg, less than the result from preliminary design phase. The structure mass to *MTOM* ratio was 27.5% while this ratio usually lay in the range from 30% to 35% for the conventional layouts. It provided clear evidences of how the structure efficiency could be improved by the proper application of composite material. The changing history of each structural component was shown in Fig. A-9.

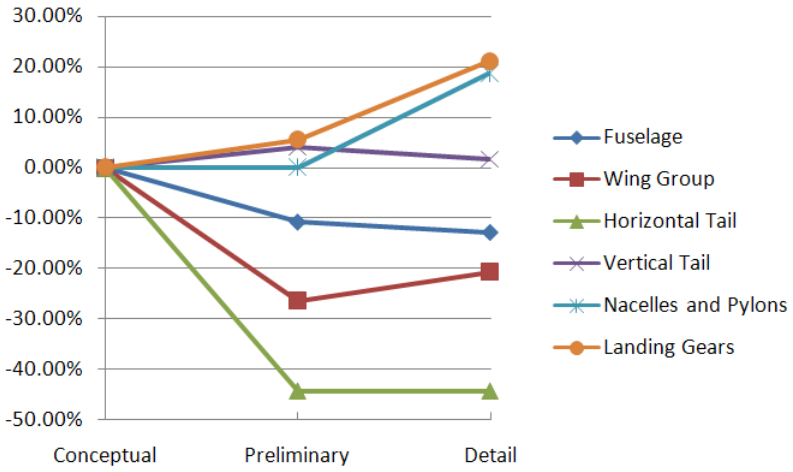

Figure A-9 Mass Change of Different Structural Components

The design payload has been increased from 12,160kg to 14,260kg as a result of the "bigger" passenger model (85kg plus 30kg extra baggage). The maximum design payload of 17,000kg has been obtained as the maximum payload capacity of the Flying Crane is 18,126kg.

While flying at design range of 2,000nm, the Flying Crane can carry maximum payload ranging from 15,545kg to 15,795kg depending on the cabin layout. The typical mass breakdown of MTOM is shown in Fig. A-10.

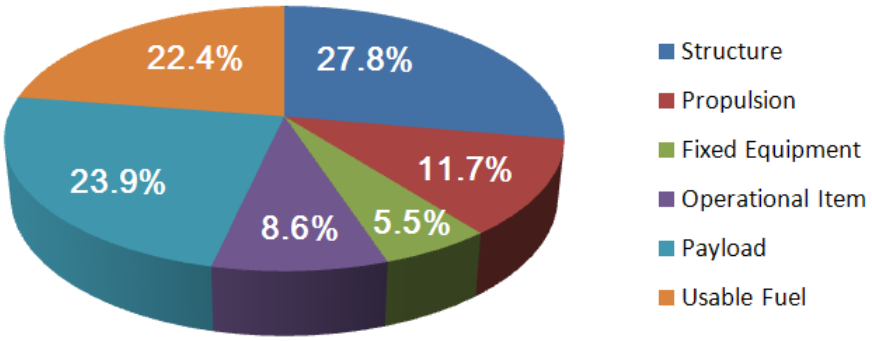

Figure A-10 Maximum Take-off Mass Breakdown (Single-aisle double class)

Except for two double class configurations, cargo loading restriction should be applied in order to meet the forward CG limit, and the principle of the loading restriction is filling the rear cargo compartment first.

A.4 Further Work

For the intake design, though the “Big” intake had a larger drag divergence Mach number, the increased maximum height of nacelle put more weight on the nacelle. And furthermore, bigger nacelle also meant larger wetted area and increased friction drag. More optimization should be involved. The nacelle/wing and nacelle/wing/pylon interference should also be further analyzed.

For the Mass and CG control, further updating and weight check should follow along with the freeze of design and manufacture of each component.